

**REPORT DOCUMENTATION PAGE**Form Approved  
OMB NO. 0704-0188

i

Public Reporting burden for this collection of information is estimated to average 1 hour per response, including the time for reviewing instructions, searching existing data sources, gathering and maintaining the data needed, and completing and reviewing the collection of information. Send comment regarding this burden estimates or any other aspect of this collection of information, including suggestions for reducing this burden, to Washington Headquarters Services, Directorate for Information Operations and Reports, 1215 Jefferson Davis Highway, Suite 1204, Arlington, VA 22202-4302, and to the Office of Management and Budget, Paperwork Reduction Project (0704-0188,) Washington, DC 20503.

|   |   |  |  |  |  |
|---|---|--|--|--|--|
| 1. AGENCY USE ONLY (Leave Blank)  |   | 2. REPORT DATE<br>01 FEB 1999                              |  | 3. REPORT TYPE AND DATES COVERED<br>SBIR Final Report<br>01 MAY 1998 through 31 JAN 1999 |  |
| 4. TITLE AND SUBTITLE<br>In-Situ Rolling Element Bearing Temperature and/or Pressure Measurement<br>U.S. Air Force Phase I SBIR Final Report  |   |  |  | 5. FUNDING NUMBERS<br><br>F29601-98-C-0119   |  |
| 6. AUTHOR(S)<br>David A. Nickel, Farshid Sadeghi  |   |  |  |  |  |
| 7. PERFORMING ORGANIZATION NAME(S) AND ADDRESS(ES)<br><br>Innovative Design & Technology, Ltd.<br>1220 Potter Drive, Suite 130D<br>West Lafayette, IN 47906   |   |  |  | 8. PERFORMING ORGANIZATION<br>REPORT NUMBER<br><br>IDT-F-03                              |  |
| 9. SPONSORING / MONITORING AGENCY NAME(S) AND ADDRESS(ES)<br><br>Air Force Research Laboratory / VSOE<br>SBIR Program Office<br>3650 Aberdeen Avenue, SE<br>Kirtland AFB, NM 87117-5776   |   |  |  | 10. SPONSORING / MONITORING<br>AGENCY REPORT NUMBER                                      |  |
| 11. SUPPLEMENTARY NOTES   |   |  |  |  |  |
| 12 a. DISTRIBUTION / AVAILABILITY STATEMENT<br>Approved for public release; distribution unlimited.   |   |  |  | 12 b. DISTRIBUTION CODE  |  |
| 13. ABSTRACT (Maximum 200 words)<br><br>Report developed under SBIR contract.<br><br>Two programs have been undertaken to evaluate technologies for noninvasive diagnostic and condition-monitoring sensors to be used in land- and space-based applications, with an emphasis on spacecraft attitude-control wheels.<br><br>Thin-film deposition and patterning processes have been formulated for the production of thin-film resistive sensors for in-situ measurement of pressure and temperature transients in lubricated contacts. These sensors have been tested in a laboratory-scale rig using both oils and greases with both hydrocarbon and fluorocarbon base oils. A small, low power signal conditioner has been developed to facilitate use of the sensors in non-laboratory environments.<br><br>The open literature concerning three technologies for remote measurement of lubricant migration and degradation has been reviewed. Direct vapor pressure measurement, quartz crystal microbalances, and process residual gas analyzers have been assessed. Of the three, process residual gas analyzers are deemed the most promising for both tasks considered. |   |  |  |  |  |
| 14. SUBJECT TERMS<br>tribology, elastohydrodynamic contact, in-situ sensor, lubricated contact  |   |  |  | 15. NUMBER OF PAGES<br>105   |  |
|   |   |  |  | 16. PRICE CODE   |  |
| 17. SECURITY CLASSIFICATION<br>OR REPORT<br>UNCLASSIFIED  | 18. SECURITY CLASSIFICATION<br>ON THIS PAGE<br>UNCLASSIFIED | 19. SECURITY CLASSIFICATION<br>OF ABSTRACT<br>UNCLASSIFIED |  | 20. LIMITATION OF ABSTRACT<br><br>UL   |  |

NSN 7540-01-280-5500

Standard Form 298 (Rev.2-89)  
Prescribed by ANSI Std. Z39-18

19990127 000

## TABLE OF CONTENTS

|  |    |
|--|----|
| INTRODUCTION .....   | 1  |
| THIN-FILM SENSORS FOR ELASTOHYDRODYNAMIC CONTACT PRESSURE<br>AND TEMPERATURE SENSING. .... | 3  |
| Goals to be Achieved. ....   | 3  |
| Literature Review. ....  | 3  |
| Theory of Sensor Operation. ....   | 11 |
| System Design Issues. ....   | 15 |
| Influences on the dynamic behavior of thin-film contact sensors. ....                      | 15 |
| Two contact examples to indicate the contact passby time scale. ....                       | 16 |
| Finite sensor width effect on sensor temporal response. ....                               | 18 |
| Sensor frequency response limitation due to capacitive coupling to substrate. ...          | 19 |
| System-imposed limits on contact sensor frequency response. ....                           | 23 |
| Summary and discussion ....  | 23 |
| Deposition of Thin Films: Precleaning and Sputtering. ....                                 | 24 |
| Pre-deposition cleaning. ....  | 24 |
| Sputtering. ....   | 26 |
| Introduction. ....   | 26 |
| Gas and plasma properties in an RF (radio frequency) plasma. ....                          | 27 |
| Process parameters. ....   | 31 |
| Deposition of durable films. ....  | 32 |
| Control of electrical properties. ....   | 35 |
| Layers deposited for EHD sensor fabrication. ....  | 35 |
| Sensor Pattern Production. ....  | 36 |
| Through-mask deposition ....   | 37 |
| Laser etching. ....  | 37 |
| Photolithography. ....   | 41 |
| Introduction. ....   | 41 |
| Photomask generation. ....   | 42 |
| Chemical etching. ....   | 42 |
| Development of a zirconium thin-film etchant compatible with oxide insulators. ....        | 44 |
| Photoresist strip. ....  | 47 |
| Implementation of photolithography on glass disk substrates ....                           | 48 |
| Thin-Film Interconnects. ....  | 49 |
| Thermal Aging Bake ....  | 52 |

## TABLE OF CONTENTS (CONTINUED)

|   |    |
|---|----|
| Signal Conditioning. ....   | 52 |
| Calibration. ....   | 54 |
| Thermal calibration procedure. ....   | 55 |
| Pressure calibration procedure. ....  | 55 |
| Testing. ....   | 56 |
| Description of Test Rig. ....   | 56 |
| Signal Conditioning, Data Acquisition and Post-Processing. ....                 | 57 |
| Results. ....   | 59 |
| RADIO TELEMETER for component temperature assessment. ....                      | 68 |
| Goals to be Achieved. ....  | 68 |
| Literature Review. ....   | 68 |
| Theory of Device Operation. ....  | 69 |
| System Design Issues. ....  | 71 |
| Circuit Design. ....  | 71 |
| Overall feedback circuit. ....  | 71 |
| Amplifier components. ....  | 72 |
| Tank circuit. Broadcast antenna. Temperature-sensing capacitors. ....           | 73 |
| Power source. ....  | 75 |
| Telemeter Manufacture. ....   | 75 |
| Circuit board manufacture. ....   | 76 |
| Surface mount technology component attachment. Telemeter holder. Final testing. | 77 |
| Calibration and Test Procedure. ....  | 78 |
| Signal monitoring. ....   | 78 |
| Calibration. ....   | 79 |
| Use in axial bearing test rig. ....   | 80 |
| Test Results, Discussion of Results. ....                                       | 81 |
| VAPOR PRESSURE LITERATURE SEARCH. ....  | 85 |
| PHASE I CONCLUSIONS. ....   | 89 |
| PHASE II THRUSTS. ....  | 90 |
| REFERENCES. ....  | 91 |

## LIST OF FIGURES

| Figure   | Page |
|--|------|
| 2.1 Relative disk orientation in a twin-disk machine. ....   | 4    |
| 2.2 EHD pressure or temperature sensor, views (a) normal to substrate surface. ....<br>(b) of a crosssection of the substrate surface. | 12   |
| 2.3 Exemplary temperature and pressure profiles. ....  | 17   |
| 2.4 Finite-size effect of thin film sensor in EHD contact. ....  | 18   |
| 2.5 Response rolloff due to finite sensor width, shown in the frequency domain. ...  | 20   |
| 2.6 Wheatstone bridge schematic showing thin-film sensor and interconnect pads. .  | 21   |
| 2.7 Lumped parameter sensor/bridge dynamic model. ....   | 22   |
| 2.8 Simulated frequency response of $120\Omega$ thin-film resistive sensor ....  | 22   |
| 2.9 Example program for computer-controlled table. ....  | 38   |
| 2.10 Schematic of laser patterning apparatus. ....   | 39   |
| 2.11 Interferograms of laser-patterned lines (40X). ....   | 40   |
| 2.12 Schematic of a Wheatstone bridge. ....  | 53   |
| 2.13 Typical thermal calibration curve of pressure and temperature sensors. ....   | 55   |
| 2.14 Schematic of optical EHD rig core. ....   | 57   |
| 2.15 Comparison of analytical and experimental pressure estimates. ....  | 60   |
| 2.16 Comparison of analytical and experimental temperature estimates. ....   | 60   |
| 2.17 Comparison of analytical and experimental temperature transients (1 of 3). ....   | 61   |

## LIST OF FIGURES (CONTINUED)

| Figure  | Page |
|---|------|
| 2.18 Comparison of analytical and experimental temperature transients (2 of 3). . . .   | 62   |
| 2.19 Comparison of analytical and experimental temperature transients (3 of 3). . . .   | 63   |
| 2.20 Pressure sensor output, NLGI-00 grease with mineral oil. . . . .   | 65   |
| 2.21 Pressure sensor output, NLGI-1 grease with mineral oil. . . . .  | 66   |
| 2.22 Pressure sensor output, NLGI-2 grease with PFPAE oil. . . . .  | 67   |
| 3.1 Analog modulation methods. . . . .  | 70   |
| 3.2 Block Diagram of a Radio Transmitter. . . . .   | 70   |
| 3.3 Radio Telemeter Circuit Schematic. . . . .  | 71   |
| 3.4 Qualitative thermal capacitance response of an EIA Type III dielectric. . . . .   | 74   |
| 3.5 Eveready 337 battery life at room and elevated temperatures. . . . .  | 76   |
| 3.6 Artwork used to construct photomask for six circuit boards (5X). . . . .  | 77   |
| 3.7 Photograph of telemeter in holder (approximately 4X). . . . .   | 78   |
| 3.8 Two telemeter temperature calibration curves. . . . .   | 80   |
| 3.9 Measured roller (via telemeter) and housing (via attached thermocouple) . . . . .<br>temperatures of a tapered roller bearing with a nominal Hertzian stress level<br>of 175 ksi and shaft speeds of (a) 400, (b) 800, and (c) 1600 rpm.  | 82   |
| 3.10 Measured roller (via telemeter) and housing (via attached thermocouple) . . . . .<br>temperatures of a tapered roller bearing with a nominal Hertzian stress level<br>of 250 ksi and shaft speeds of (a) 400, (b) 800, and (c) 1600 rpm. | 83   |
| 3.11 Bearing roller and housing temperatures before and after oil flow interruption . .<br>(operating conditions: 175 ksi nominal, 800 rpm).  | 84   |
| 4.12 Photograph of process RGA head (~ 2X scale). . . . .   | 88   |

## LIST OF TABLES

| Table   | Page |
|---|------|
| 2.1 Quantitative comparison of different energy expressions. ....     | 31   |
| 2.2 Silicon dioxide dissolution rates in mixed fluoride species. .... | 45   |

## 1. INTRODUCTION

Satellite reaction and momentum wheels provide mission critical management of satellite orientation. Lubrication-induced failures in attitude control wheels (ACWs, a term including both reaction and momentum wheels) have limited satellite life in the past [6], with this sometimes due to design flaws, sometimes to early expenditure of the onboard lubricant store. Auer [2] confirms this with the statement that "ball bearing lubrication remains the principal life-limiting problem on momentum and reaction wheels."

From the point of view of a spacecraft dynamist, reaction and momentum wheels appear quite similar. This similarity extends to the major components of the wheel: an enclosure, motor, drive electronics, and a spindle. To a tribologist, the two are very different. Momentum wheels rotate in one direction and at a relatively large, consistent speed. A benefit of this is the formation of a relatively thick film of lubricant which separates rotating components and damps vibration (in a regime known as EHL, or elastohydrodynamic lubrication). A detriment is the centrifugal pumping of lubricant out of the spindle bearings, a process that necessitates a lubricant recirculation system. Reaction wheels, on the other hand, rotate slowly and often reverse direction. The slow speed makes sealed bearings a design-simplifying possibility. Unfortunately it also results in frequent collapse of the separating lubricant film (this regime is known as boundary lubrication). Loss of a continuous, protective oil film results in metal-to-metal contact, dramatically accelerated wear, and localized flash temperatures sufficient to chemically degrade the base oil and additives constituting the lubricant.

The choice of lubricant and lubrication system is influenced by these and other factors, including lubricant outgassing potential, the tendency of breakdown products to interfere with satellite functions, and the temperature range the spindle will act in. An incorrect decision can affect satellite operation [3]. To insure reliable operation, the 1988 military standard MIL-A-83577B [1] imposed the requirement that "momentum wheels

bearings shall operate in the elastohydrodynamic film regime confirmed by analysis or test."

The standard listed contact resistance measurement as an experimental method of verifying EHL operation. Contact resistance provides a crude indication of the degree of metal-to-metal contact. It does not provide detailed information about lubricant pressure, temperature, or film thickness, parameters useful in ascertaining the effect of changes in bearing environment (ambient temperature, for example) or for verifying the accuracy of numerical models. A more detailed perspective of contact and lubricant status can be provided using a family of sensors introduced in the 1960's and 1970's and improved upon in the 1980's and 1990's. These sensors, which are applied to one of the surfaces in the contacting element pair, provide the ability to measure pressure, temperature, and lubricant film thickness fluctuations in real time. Installed in ground-based test equipment, bearings instrumented with these sensors can provide definitive answers to ACW designers. Models can be verified, and limiting conditions tested.

Friction, heat, and motion disperse and degrade a lubricant. Migration depletes the limited reservoir provided for an ACW bearing spindle. Degradation converts it to a form that is at best less useful, at worst deleterious to bearing function. Each of these can be measured using sensors external to the spindle. The two sensors described have their genesis in the vacuum deposition and processing industry. The first measures condensing mass flux, the second the partial pressure of the gases characteristic of a degrading oil.

Phase I consisted of two major tasks: technical advancement of thin-film sensors for the in-situ measurement of pressure and temperature transients in rolling contacts, and a literature search for technologies to be used in remote lubricated contact condition monitoring. The primary emphasis was to be placed on the first of these. The remainder of the report consists of one chapter on each thin film sensors, one providing background information for a slated Phase II effort in radio telemetry for remote component diagnosis or condition monitoring, and the results of the literature review concerning physical & chemical sensors for remote diagnosis of lubricated contact condition, followed by a list of references cited throughout the report.



## 2. THIN-FILM SENSORS FOR ELASTOHYDRODYNAMIC CONTACT PRESSURE AND TEMPERATURE SENSING.

### 2.1 Goals to be Achieved.

The determination of pressure and temperature in heavily-loaded lubricated contacts is of significant interest to product designers. Contact pressure and temperature influence the specification of lubricants, the size and tolerancing of tribological components, and the materials employed in the contact pair.

Contact sensors for pressure, temperature, and lubricant film thickness determination have been produced by laboratories in the United States, Germany, England, the Netherlands, Egypt, Poland, and, most recently, Japan. Only one of these laboratories is currently active in the production of these sensors, in spite of the demand. There is a gap between laboratory capabilities and industrial needs.

The development of durable, accurate sensing systems is as much a question of process as of concept. For incorporation in the industrial research and development cycle, this process must be as simple as possible and must require minimal capitalization. The process is a combination of a set of equipment and a base of factual and conceptual knowledge. The goal of this phase is the development of and improvement on durable, accurate sensing systems for the measurement of lubricant pressure and surface temperature in elastohydrodynamic contacts.

### 2.2 Literature Review.

In-situ sensors have been employed for the assessment of lubricated contact parameters for over 35 years. The technology has moved from continent to continent and laboratory to laboratory, with concurrent development at multiple centers rare. Improvements in sensor size, precision, and durability have followed corresponding

improvements in microelectronic fabrication and wear-resistant coatings. Historical points of significance include improvements in technology and applications considered by other researchers.

One explanation may be useful to readers not familiar with tribological test equipment. A device known as a “twin disk machine” is often used to test tribocomponent materials, lubricants, and, probably because it is already available, thin-film sensors. It consists of two spindles capable of holding disks, motor/drive systems for one or both spindles, a sliding or rotational mechanism that allows one spindle to be moved toward and away from the other with a known force applied, and sensors to monitor speed, load, and/or torque. Figure 2.1 depicts the typical relative orientation of the two driven disks.

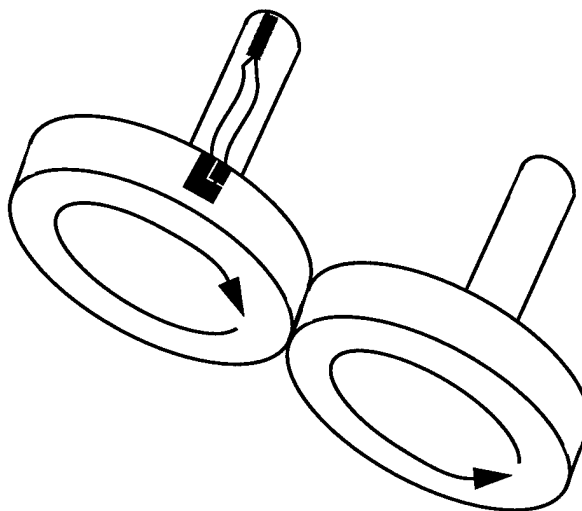


Figure 2.1: Relative disk orientation in a twin-disk machine.

Load or pressure and two speed-related parameters are monitored: the absolute tangential surface speeds of the two disks, and “slip”, or the ratio of the difference between surface speeds to the mean surface speed. In the desirable case of “pure rolling,” the two surface speeds are equal in sign and magnitude and the slip is zero-valued.

The first documented thin-film sensor was fabricated by A.W. Crook in 1961 [8]. This sensor consisted of a thin chromium film deposited onto a 3 inch diameter glass disk and was used in a twin-disk apparatus. Signal conditioning consisted of a DC potential placed across the metal film with a resistor of unspecified value used as a current-to-voltage converter, a configuration that permitted a form of film thickness

measurement via capacitive discharge. Few other details were included, and a promised "fuller account" of the experiment was not found.

Resistive pressure and temperature measurement was documented by Orcutt in 1965 [22]. Again, an instrumented glass disk was run against a steel disk. The temperature sensor was fabricated by painting "liquid bright platinum" onto a 25 micron wire, then pressing the wire onto the disk and firing at 680°C in air. The pressure sensor was fabricated by evaporation of manganin. The thicknesses and widths of the platinum and manganin sensors were estimated to be 0.1 to 0.15 and 25 to 38 microns. Signal conditioning consisted of a Wheatstone bridge formed on the rotating disk to avoid excessive resistance noise in the mercury contactor used. Orcutt reports an anomalously high TCR (thermal coefficient of resistance) of 110 ppm/°C, attributing it to deposition technique. Measured temperature results are used to compensate for thermal sensitivity in the manganin device, with no reported pressure cross-sensitivity discussed in the 0.17 to 0.28 GPa applied pressure range.

Kannel of the Battelle Memorial Institute has introduced several innovations in thin-film pressure and temperature measurement. Two publications in 1965 [23], [24] introduced pressure and temperature sensors on quartz and steel substrates, with a twin-disk machine forming the test geometry. A manganin strip 50 microns wide was evaporatively deposited (using a wire-fed source to maintain stoichiometry) to fabricate a pressure sensor. A strip thickness of 0.025 to 0.050 microns was estimated based on the 4400Ω typical sensor resistance and resistivity values quoted from the literature. Manganin is stated to have a PCR (pressure coefficient of resistance) of approximately -2Ω/Ω-GPa, with the exact value determined in [23] by equating a time-integral of pressure to the known applied load. Kannel used a silver-bearing paint to form external contacts, although he needed to embed a wire in the paint due to cracking during relatively large temperature excursions.

Kannel's process for a sensor on steel [24] began with an unspecified polish of the steel substrate, with the final agent alumina. Subsequent to chemical cleaning, an ion cleaning operation was performed at 10 mTorr. A silicon oxide insulation layer approximately 0.75 microns thick was deposited by reactive evaporation of silicon monoxide in a 1 mTorr atmosphere of unspecified feed gas. The coating thus obtained was transparent, leading to the interpretation that the material deposited was nearly SiO<sub>2</sub>.

Thinner layers were said not to be insulating, thicker ones to crack. The layer thus deposited was observed to be piezoelectric, resulting in the impression of a bias voltage onto sensor. To extract resistive from piezoelectric effects, tests were run with positive and negative excitation voltages and the result formed from their average. Sensors were subjected to pressures from 0.72 to 0.88 GPa.

Kannel published three more papers on the subject, one in 1974 [25] a second in 1978 [26], and a third in 1980 [27]. These involved more challenging environments (metal rolling in the first, 20% slip in the third). Two technological changes were made in sensor manufacture and described in [26]. A one micron layer of sputtered aluminum oxide formed a more durable insulation layer (Kannel states an initial substrate roughness of 25 nm center line average (CLA)). The "bisignal" transducer is introduced. This consists of two features: a stacked structure that places pressure and temperature sensor lines atop one another to insure rotational phase alignment, and a Wheatstone bridge capable of adding weighted combinations of the pressure and temperature sensor signals, permitting in-bridge compensation for cross-sensitivity effects.

More recently, Kannel and Merriman have measured the low-pressure elastohydrodynamic contact involved in the printing process [28]. Most of this work employs techniques not appropriated for concentrated tribocomponent contacts. One interesting excursion involves the use of Ytterbium.

Hamilton and Moore (1971) report results from a four-disk machine using an instrumented glass disk. The novel aspects of this paper lie not in the contact sensors, but in the auxiliary sensors used: an optical sensor used to trigger the oscilloscope and floating thermocouples run against the disk and used to measure bulk lubricant temperature [29]. The authors describe sensor self-heating as a problem for currents in excess of 20 mA (4V half-bridge voltage in the case of their approximately 100  $\Omega$  sensor), and state a manganin sensor TCR and PCR (pressure coefficient of resistance) of approximately 100 ppm/ $^{\circ}$ C and 0.01 to 0.02  $\Omega/\Omega$ -GPa. Nickel films were used in temperature measurement - these again exhibited an unexpectedly low TCR of 1300 ppm/ $^{\circ}$ C. Observable pressure crosssensitivity was noted. Some sensor width effects were observed (typical gauge width was 45 microns), for which deconvolution of the output signal was suggested. The authors measure pressure, temperature, and film thickness, notably listing a model for lubricant dielectric constant.

After the work of Hamilton and Moore, research in the United Kingdom moved from Reading to Imperial College, with J.C. Anderson supervising M.M.A. Safa. Safa's papers discuss fabrication details more completely than most authors, making them a valuable asset.

The first, 1979 paper [33] concerns manufacture of manganin resistive pressure sensors and chromel/alumel thin-film thermocouples for testing in a twin-disk machine. Aqueous and solvent degreasing was followed by low pressure sputtering. Sputtered silica, chromia, and alumina were tried as isolation materials, with 1 micron alumina ultimately chosen. Best results were obtained with the substrate water-cooled. Sputtered manganin was tried and found to be mechanically durable, but electrically inconsistent, with the cause determined as stoichiometric inaccuracy. Patterning of the manganin sensor was done by flash evaporation through a laser-cut mask. The nominal manganin thickness was 0.1 microns. The mask, which featured a 2.5 micron slit, was developed at Imperial College using an apparatus described in De Silva et al. [34]. The mask was positioned on the disk without breaking vacuum. Flash evaporation through masks also was used in the fabrication of the 25 by 125 micron junction thin-film thermocouples. Again, the films used in construction of thermocouples were said to be approximately 0.1 microns thick. The authors calibrated in a hydraulic press, but observed a different apparent pressure sensitivity in their machine, something they attributed to a different stress state. No evidence of a pressure spike was found in this research. Sensor durability was an issue, with 50% failure and no sensors surviving more than 30 minutes testing at pressures up to 1.08 GPa (slip not specified).

De Silva [34] describes the method used to laser-cut masks for through-mask deposition. A 2 KW Nd-YAG laser was used with a pulse rate and duration of 1000/second and 200 nanoseconds. Metal films with thicknesses to 100 microns (0.004 inches) were cut using a 2.5 to 10 micron spot, with a 25 micron molybdenum foil used to manufacture the mask used in [33].

Safa's second paper, published in 1982 [35], describes improvements to the process made during the interim period. One key change in process was replacement of the thin-film thermocouple used in temperature measurement with a thermistor, differing thermoelectric variation with pressure cited as the reason. The sensors were employed both on the twin-disk apparatus and in a cylindrical roller bearing. Rather than through-mask deposition, the sensor on the bearing inner ring was patterned directly using the laser

beam. This publication shows pressure-spike results on the twin-disk machine, but not in the case of the roller bearing. The titanium thermistor shows pressure effects which are dealt with using a separate pressure calibration, assuming the manganin sensor to be unaffected by temperature variations.

In 1985, Safa and Gohar presented a study of EHD impact of a steel ball onto a glass plate at the 12th Leeds-Lyon Symposium on Tribology [36]. Pressure is measured using a manganin sensor, and pressure-time plots much like those observed in rolling contact were noted. Other than this, the 1985 study introduces nothing new to those involved in traditional tribocomponent measurements.

A similar research effort by Mokhtar and Abdel Ghany took place at the University of Cairo. Three papers [30]-[32] describe the authors' fabrication and test results, although many important details like sensor length are not included.

The longest, most consistent effort to develop thin-film sensors has been in Germany. This program, along with offshoots in Poland and the Netherlands, overlapped the period of greatest technological development in microelectronics.

The first publication describing German thin-film sensor development appeared in 1976 [37]. Authors Bartz and Ehlert used an instrumented steel disk in a twin-disk apparatus to characterize lubricant viscosity variation with pressure and temperature. Manganin and titanium pressure sensors 0.030 and 0.10 microns thick, and 10 microns wide were employed.

In 1980, Peeken and Köhler [38] described development of an instrumented shaft used to measure the pressure and temperature fluctuations during rolling of a cylindrical roller bearing over the stationary shaft. Electron-beam evaporation was used to concurrently deposit nickel and chromium in an unspecified ratio designed to minimize TCR. A 20 to 50 micron stripe was formed by through-mask deposition. A titanium thermistor was used for temperature measurement. Measurements appear rough, with output nearly symmetric across the contact sensor and no evidence of an EHD pressure spike. This paper was followed by another in 1981 [39] reporting results on a twin-disk machine. Here a pressure sensor 1.5 mm by 20 microns by 0.05 microns thick is used to measure pressures up to 1.5 GPa under stationary and oscillating loads. Some evidence of a pressure spike is observable in these data.

Another 1980 article, this time by Peecken and Spilker, describes the design of a test chamber in which pressures to 2 GPa can be generated [40].

Königer and colleagues explored ion beam sputtering as a possible means of producing durable aluminum oxide isolation layers [41]. Ion beam sputtering differs from typical cathode sputtering in that an external source is used to generate the beam striking the sputtering target and/or substrate -- no process gas is introduced to the deposition system. Films ranging in thickness from 0.6 to 4 microns were tested at a peak pressure of 1.9 GPa with slip from 2 to 40 percent. Coatings were deemed durable if they survived 5 minutes of continuous operation. The authors found all coatings to survive lubricated low-slip testing, coatings thinner than 1.5 microns durable enough under lubricated, high-slip testing, and no coatings lasted without lubrication. This technique was later used to produce manganin and platinum thin-film pressure and temperature sensors [42]. Two methods of patterning were used: through-mask deposition and photolithography. The authors tried two nonstandard methods of photolithography: lift-off, which uses a photoresist layer applied before deposition and removed afterwards to produce a photographic negative of the patterned resist, and ion-beam etching, which uses the same ion gun employed in sputter-etching to remove the regions of a thin film not protected by photoresist. Lift-off by its nature often introduces deposition process contamination and reduces adherence, something found by the authors. Ion-beam etching, on the other hand, permitted them to successfully pattern even platinum, for which few chemical etchants exist. They found this method to be easy to use for different materials, and that there were no serious consequences of overetching. Their twin-disk results showed no evidence of the enhanced cross-sensitivity associated with film contamination. There seems to be one additional advantage to either their sputtering system or sputtering method. In contrast to Safa's experience in [35], they were able to sputter the manganin alloy without a noticeable change in crosssensitivity.

Janczak and Hofman published two papers describing the work at Radom in Poland [43], [44]. Testing was done on a twin-disk rig with fluid hydraulic drives. Measured pressure and temperature results were predictably low in noise. Notable among both papers is a theoretical and experimental analysis and ranking of sources of measurement error.

The other major European center for thin-film EHD contact sensor development is Eindhoven in the Netherlands. Authors Schouten, van Leeuwen, and

Meijer presented two reports on a program to measure contact parameters in a cam/flat follower contact [45], [46] to the Leeds-Lyon Symposium. Nichrome and titanium sensors were photolithographically patterned onto the flat follower plate. The reported sensor dimensions (200 long by 20 wide by 0.030 microns thick) are typical, but the reported results appear noisy, with the shapes of the curves not characteristic of typical EHD sliding contacts.

Roth et al. studied process parameters associated with reactively sputtered aluminum oxide [47], [48]. In their first paper, process parameters were compared with the resultant coating microstructure as observed using electron microscopy. In the second, the best process was evaluated using a Timken sliding block test.

In 1987, Baumann [49] introduced a new method for dealing with pressure sensitivity in the titanium thin-film temperature sensors used. Noting the positive PCR of the manganin pressure sensor and the negative PCR of titanium, he assembled a layered coating of both with thickness ratio determined for zero PCR. In practice, the PCR was reduced by a factor of twenty.

Haller and Kirschner continued to improve the quality of their measurements, releasing in 1989 a set of cam/flat follower measurements that conformed most closely to theoretical predictions [50].

Finally, in 1991, Holland and Tychsen published a comprehensive, detailed description of the application of photolithographic methods to EHD contact sensors [51]

The most recent publications (compared to Merriman and Kannel's somewhat-related 1997 work [28]) come from the Musashi Institute of Technology in Japan [52], [53]. Both involve the measurements on hydrodynamic crankshaft bearings in an engine simulator. Pressure and temperature measurements were made, with temperature measurements needed to compensate for crosssensitivity in the pressure sensors fabricated (this due to a small, 0.15 GPa, anticipated pressure change). Thin-film thermocouples were used in a manner analogous to Tian et al. [54]. Three sputtered SiO<sub>2</sub> layers were deposited to a total insulator depth of 2.1 microns, a factor that the authors said improved the durability of the overall layer. It is interesting to note that the same technique is sometimes used to overcome point defect formation in insulating films.



### 2.3 Theory of Sensor Operation.

Three EHD film properties, pressure, temperature, and film thickness, have been measured by researchers to characterize the state of a lubricated contact. The first two, which are discussed in this document, are monitored by the same type of transducer. Both pressure and temperature affect both the shape and material resistivity of the sensor employed. This change in resistivity translates to a change in the resistance of the sensor. Note this mechanism is different than that observed in strain gauges, where the resistivity is near-constant and the sensor resistance change is due only to minute changes in sensor dimensions.

EHD in-situ pressure or temperature sensors are formed by depositing and patterning thin conductive films on an insulating substrate or an insulating layer over a conductive substrate. Figure 2.2 shows two diagrams of a sensor, one looking along the surface normal, the other a crosssection cut into the surface. The patterned sensor has two parts: a sensitive region, which, because of its relative thinness dominates the overall resistance of the sensor and two relatively thick connector regions.

Two characteristics of the deposited sensor affect its performance. The capacitance of the sensor connective structures affects its temporal response. This is explored, along with other system design issues, in the next section. Deposition technique and substrate/sensor elastic interaction determine the temperature and pressure response of the sensor. This is considered next.

The resistance of a long, thin filament of length  $L$ , width  $w$ , and thickness  $t_M$  is well approximated by the one-dimensional conduction model

$$R = \rho \frac{L}{wt_M} \quad . \quad (2.1)$$

Here  $\rho$  is the resistivity, a constant typically though of as characteristic of a material.

The thin film sensors employed in this project rely on a small change in resistance to indirectly indicate changes in pressure and temperature. In differential form, Equation (2.1) becomes

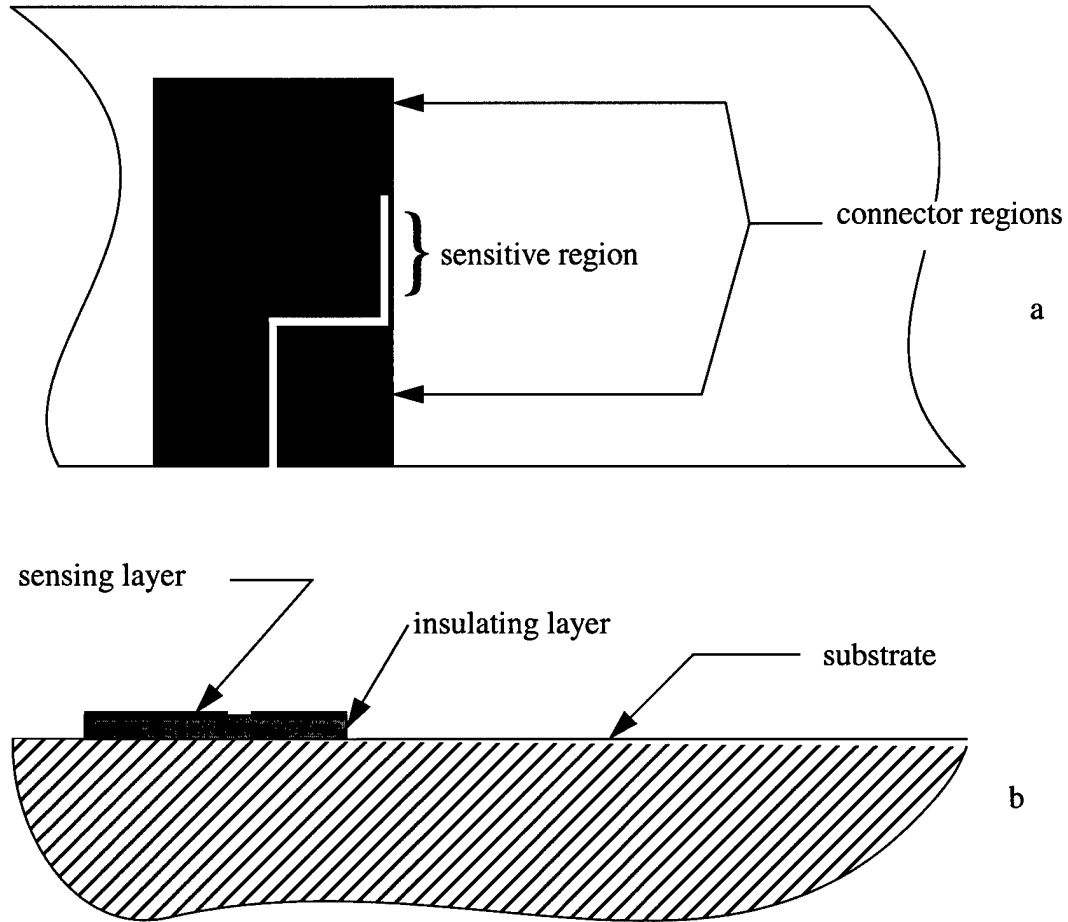


Figure 2.2: EHD pressure or temperature sensor, views (a) normal to substrate surface. (b) of a crosssection of the substrate surface.

$$dR = d\rho + (dl - dw - dt_M). \quad (2.2)$$

The change in resistance under any influence (temperature change, mechanical loading, etc.) comes from two sources: change in dimensions, and change in resistivity. The films used to manufacture thin-films sensors are very compliant because of the small in-plane dimensions. The geometric effect is dictated by the elastic response of the substrate and the effect of in-plane strain on strain in the through-thickness direction (for a Hookean body, Poisson's ratio). The validity of the Hookean model and the geometric effect on resistance of a Hookean film under Hertzian load will be considered in the dissertation.

The other term in Equation (2.2), the change in resistivity, plays a role in the determination of sensor materials and processes, and is considered here.

The electrical conduction of a continuous body is described by a quantum-mechanical crystal model [55]. In the simplest version of the model, the body consists of regularly distributed nuclei through which electrons propagate as waves. In this ideal crystal, wavelengths correspond exactly to the lattice spacing, and electron-waves propagate without loss. Any disturbance in the lattice results in wave scattering manifested as a loss, electrical resistance, and the transfer of energy from the electron to the lattice.

A number of phenomena break the periodicity of the crystal lattice in real materials. Thermal energy randomly moves nuclei from their nominal positions, resulting in scattering. As temperature increases, RMS nuclear displacement does, resulting in an almost invariably positive thermal coefficient of resistivity (thermally-induced phase change not considered). Impurity atoms, holes in the lattice, and extra atoms geometrically disturb the lattice. Grain boundaries and the surface of a finite body are extreme examples of this. The macroscopic cumulative effect of resultant scattering is modeled statistically, using the kinetic theory of gases (this will be revisited in the introduction to sputtering). The average degree of scattering associated with each cause is described by a mean time duration between scattering events  $\tau$ , with the cumulative time found by parallel addition [56]

$$\frac{1}{\tau_{\text{total}}} = \frac{1}{\tau_{\text{thermal}}} + \frac{1}{\tau_{\text{g.b.}}} + \frac{1}{\tau_{\text{surface}}} + \frac{1}{\tau_{\text{defect}}} + \frac{1}{\tau_{\text{impurity}}} + \dots \quad (2.3)$$

An increase in the density of any scattering phenomenon reduces its scattering time and causes it to have a larger impact on the total scattering time, and thus on the total resistivity. An alloy, for example, is an extreme case of impurity scattering, and the resistivity of alloys is higher than that of either constituent metal.

Each of the resistance-causing mechanisms described in Equation (2.3) has a pressure and temperature sensitivity associated with it. In pure metals, the dominant mechanism is thermal scattering. Alloy resistance is dominated by impurity and thermal effects -- the resistance contribution associated with impurities is not very temperature sensitive, so alloys tend to have a lower temperature coefficient of resistivity. For this reason, RTDs (resistance temperature devices) are made of pure metals like platinum and thin-film resistors are made of alloys like manganin, nichrome, or constantan. Grain

boundary and defect scattering is similar in the sense that, for temperatures low enough to keep thermal diffusion small, the phenomena are not very thermally sensitive, so, as resistance due to these effects increases, thermal coefficient of resistance decreases.

Surface effects become large in films whose thickness is on the order of the mean free path (MFP) of conduction electrons, a value on the order of 0.1 microns. Films thinner than the MFP exhibit resistivity that rapidly and dramatically increases [57]. Note this increase has nothing to do with film purity or continuity. The "size effect" as it is called, contributes to resistance in a way is principally sensitive to film thickness. This is affected by temperature only through substrate elastic restraint, by pressure through film elasticity and elastic restraint. The indirect strain effect is considered in Section 2.2 of Reference 57.

One factor that influences thermal motion in the crystal lattice is residual stress. The residual stress state in a deposited film will be discussed in the subsequent section concerned with thin-film deposition technology. Belu-Marian et al. [91] give an idea of the impact on strain sensitivity (closely related to pressure coefficient of resistance). Two films, one produced using RF sputtering, the other DC sputtering, were found to have longitudinal gauge factor varying by about 10%, transverse gauge factor by 400%. Klokholm [92] describes an experiment in which control of substrate temperature was used to change the arithmetic sign of the longitudinal gauge factor of evaporated nickel films.

This theory is not comprehensive. In particular, it does not consider magnetic effects. For this reason, there are alloys (Klokholm's evaporated nickel in [92], for example, or high temperature superconductors) whose resistive properties are not well predicted. In addition, the theory requires a copious supply of free electrons, an assumption not valid in the case of semiconductors or insulative materials. A special case of this is discontinuous films (physically discontinuous films during the enucleation phase of deposition or films that are chemically discontinuous due, for example, to selective oxidation of the material at grain boundaries). Here conduction of the entire film is limited by that through the insulating discontinuities [58]. The availability of conduction electrons is increased by increasing temperature, and thermal coefficient of resistance becomes negative, instead of the positive value normally observed in continuous metal films.

To quickly summarize, resistivity is not a material constant, although material plays an influential role. The resistivity, temperature coefficient of resistance, and pressure coefficient of resistance depend on thickness, residual stress state, nano- (defect), micro- (grain size, grain boundary contamination), and macro-structure (film thickness) as well. Each of these must be characterized and controlled to achieve predictable sensor operation.

## 2.4 System Design Issues.

The dynamic response of the sensor, signal conditioning system, and data acquisition system work in concert to determine the accuracy of the short-duration signals associated with an elastohydrodynamic contact. Each, in turn, is analyzed in this section.

### 2.4.1 Influences on the dynamic behavior of thin-film contact sensors.

Small contacts, coupled with high component passby speeds, make the transient signals developed by in-situ contact sensors very short in duration. The sensor and signal conditioning system must be designed to allow accurate capture of important details.

There are three principal causes for smoothing of signals generated by contact sensors. One, the effect of finite sensor width, is spatial in nature. Two others, capacitive coupling between the sensor and conductive substrate and finite bandwidth of the signal conditioning system, are temporal. For a given passby speed, the temporo-spatial nature of contact sensor signal generation couples these three phenomena, allowing direct comparison of the three causes. This in turn permits prediction of the interaction of the three phenomena, determination of the dominant source of error, and adjustment of sensor design parameters to meet not only speed, but other considerations.

### 2.4.2 Two contact examples to indicate the contact passby time scale.

Two examples of contacts tested in the Tribology Laboratory are evaluated to determine typical durations of sensor/contact interactions. This provides an indication of the frequency response required for adequate contact sensor performance.

The first contact sensors were built on glass and steel disks and tested in the Tribology Laboratory's elastohydrodynamic (EHD) lubrication-testing optical rig. Typical test contact pressures are 0.87 GPa (glass disk) or 1.20 GPa (steel disk), with 2 m/sec a common operating speed. Circular contacts like the ball-on-flat associated with this apparatus are analyzed in Johnson [10]. For specified reduced modulus  $E^*$ , equivalent radius  $R$ , and maximum pressure  $p_o$ , the radius  $a$  of the circular contact is given by

$$a = \frac{\pi p_o R}{2E^*}, \quad R = (R_1^{-1} + R_2^{-1})^{-1}, \quad E^* = \left( \frac{1 - \nu_1^2}{E_1} + \frac{1 - \nu_2^2}{E_2} \right)^{-1} \quad (2.4)$$

(here  $R_1$  and  $R_2$  are the radii of the two solids of revolution, positive if locally convex,  $E_1, E_2$  and  $\nu_1, \nu_2$  are the Young's moduli and Poisson's ratios of the homogeneous, isotropic, linearly elastic materials comprising the two components). Substitution of geometric and material constants yields  $E^*=55$  GPa for the glass/steel contact,  $E^*=115$  GPa for steel/steel,  $R=12.7$  mm for both, and radii of 317  $\mu\text{m}$  and 208  $\mu\text{m}$  for the glass/steel and steel/steel contacts. For a surface speed of 2 m/sec, the duration a thin sensor will be in the contact is 317  $\mu\text{sec}$  for the glass/steel and 208  $\mu\text{sec}$  for the steel/steel contact.

One example of another component that could be instrumented is a Timken JM205110 tapered roller bearing cone (outer ring). The cone/roller contact most closely resembles a line, with roller profiling reducing the pressure towards the ends of the line. An axial bearing load of 700 pounds (3110 N) produces a peak contact stress of 1 GPa. Roller loads are determined using an algorithm described in Wren & Moyer [9], with contact width subsequently determined using a formula from Johnson. For the load described, the resulting contact width is 190  $\mu\text{m}$ . In the case of no slip (necessary for normal operation of a rolling element bearing), the approximate surface speed is given by

$$v_{train} = \omega \left( \frac{1}{R_o} + \frac{1}{R_i} \right)^{-1} \equiv \frac{\omega r_m}{2} \quad (2.5)$$

where  $\omega$  is the angular velocity of the shaft,  $R_o$  and  $R_i$  radii of the inner and outer rings at the point of interest, and  $r_m$  the mean of the inner and outer ring radii. For the bearing of interest,  $r_m$  is approximately 30 mm. A typical operating speed of 1800 rpm (188.5 rad/sec) results in a train velocity of 5.75 m/second and a sensor passby time of 33  $\mu$ sec.

Figure 2.3 shows pressure and temperature contact sensor data taken in the EHD optical rig described in Section 2.11.1. These results were taken using an instrumented glass disk rolling and sliding against a steel ball. These show typical profiles for fluid-lubricated contacts. A key feature of the pressure distribution is the “pressure spike” at the exit of the pressure distribution shown on the bottom of the figure. The frequency content of the short-duration spike is broader-band than that of the contact as a whole. Accurate measurement of the pressure spike is important in the subsequent use of the data, so sensor bandwidth must be several times larger than that predicted by the whole-contact calculations.

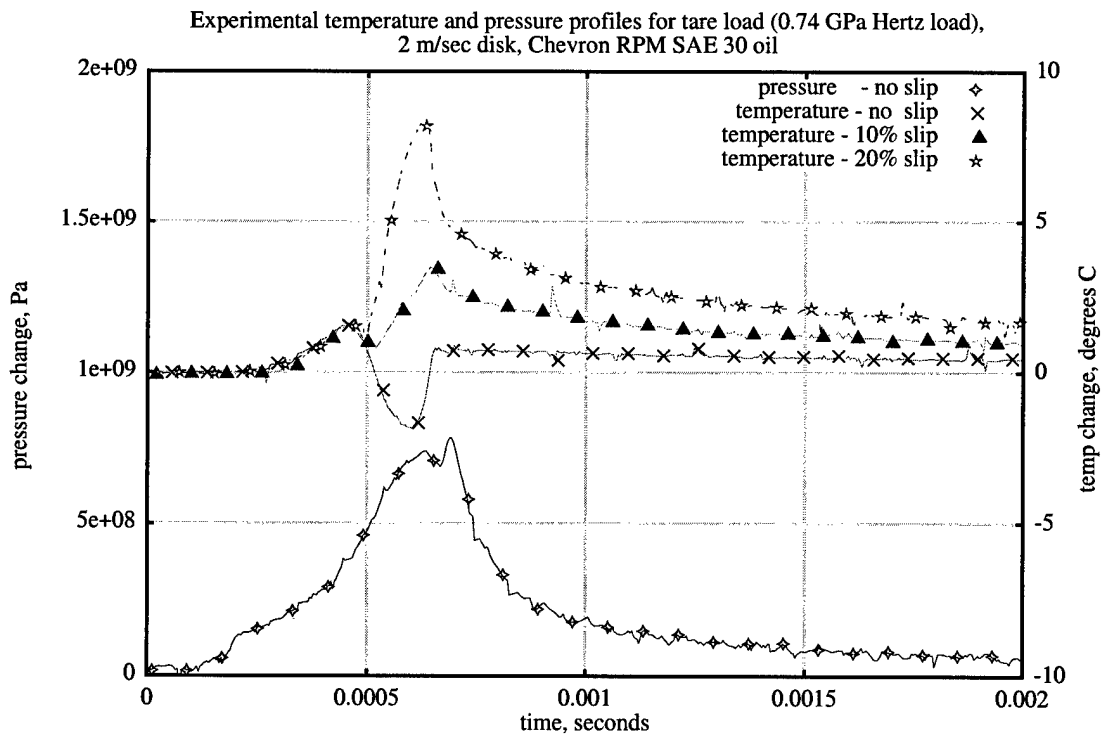


Figure 2.3: Exemplary temperature and pressure profiles.

Three factors, one geometric and two electronic, dictate the frequency response of the sensing system. Each in turn is analyzed next.

#### 2.4.3 Finite sensor width effect on sensor temporal response.

Figure 2.4 shows a rolling/sliding line contact with the pressure distribution superimposed. Vertical dimensions are magnified tremendously, horizontal dimensions

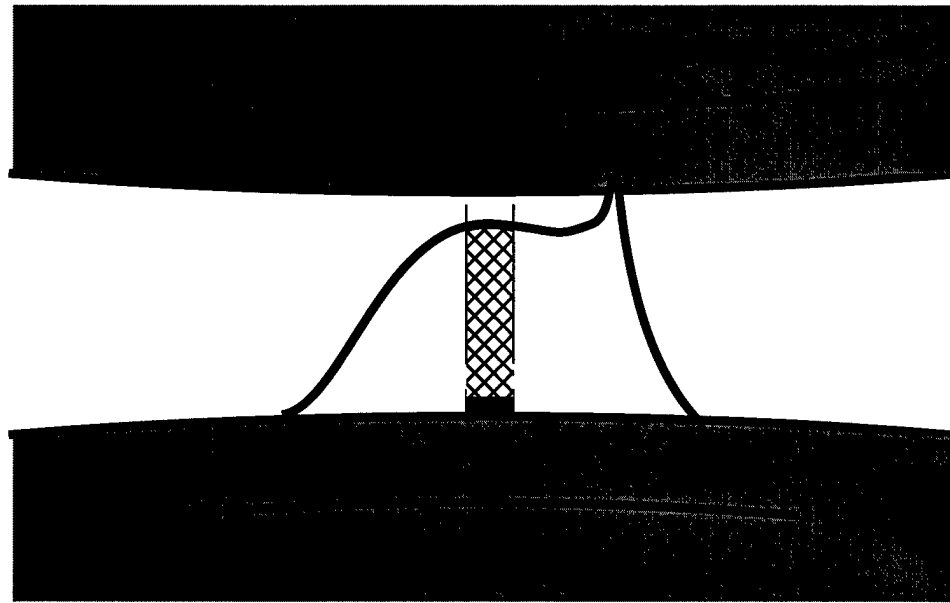


Figure 2.4: Finite-size effect of thin film sensor in EHD contact.

somewhat less so. As the sensor on the lower, instrumented roller passes over the contact, it is affected by a contact parameter: either pressure, as shown in the figure, or temperature. The sensor film is typically 100 times as wide as it is thick, justifying the assumption that edge effects are negligible. Assume further a uniformly thick sensor. The fluctuation in resistance is given by



$$s_o(t) = \int_{-\frac{a}{2}}^{\frac{a}{2}} s_i(t + \frac{x}{v}) w(x) dx \quad (2.6)$$

where  $s_o$  is the output signal,  $s_i$  the input,  $w$  the distribution of sensor sensitivity across its width,  $a$  the sensor width, and  $x$  the coordinate in the rolling direction. Transformation of the variable integrated to  $(x/v)$  and definition of  $w$  as taking the value zero for coordinates  $x$  outside of the sensor forms the convolution integral

$$s_o(t) = \int_{-\infty}^{\infty} s_i(t + \phi) w(\phi) d\phi = v(s_i * w) . \quad (2.7)$$

Transformation into the frequency domain shows the role of finite sensor width

$$s_o(f) = v S_i(f) W(f). \quad (2.8)$$

$vW$  plays the role of a low pass filter. Taking  $w$  as a rectangular pulse is both simple and appropriate. In this case, the filter function becomes the sinc function

$$vW(f) = \frac{\sin\left(\frac{\pi af}{2v}\right)}{\frac{\pi af}{2v}}. \quad (2.9)$$

Figure 2.5 shows the rolloff characteristic corresponding to a typical sensor width and passby speed.

#### 2.4.4 Sensor frequency response limitation due to capacitive coupling to substrate.

The second response-limiting mechanism is caused by capacitive coupling of the sensor to the conducting substrate. The tribological components monitored using contact sensors are typically made of steel, a conductor. To fabricate a sensor, first a thin

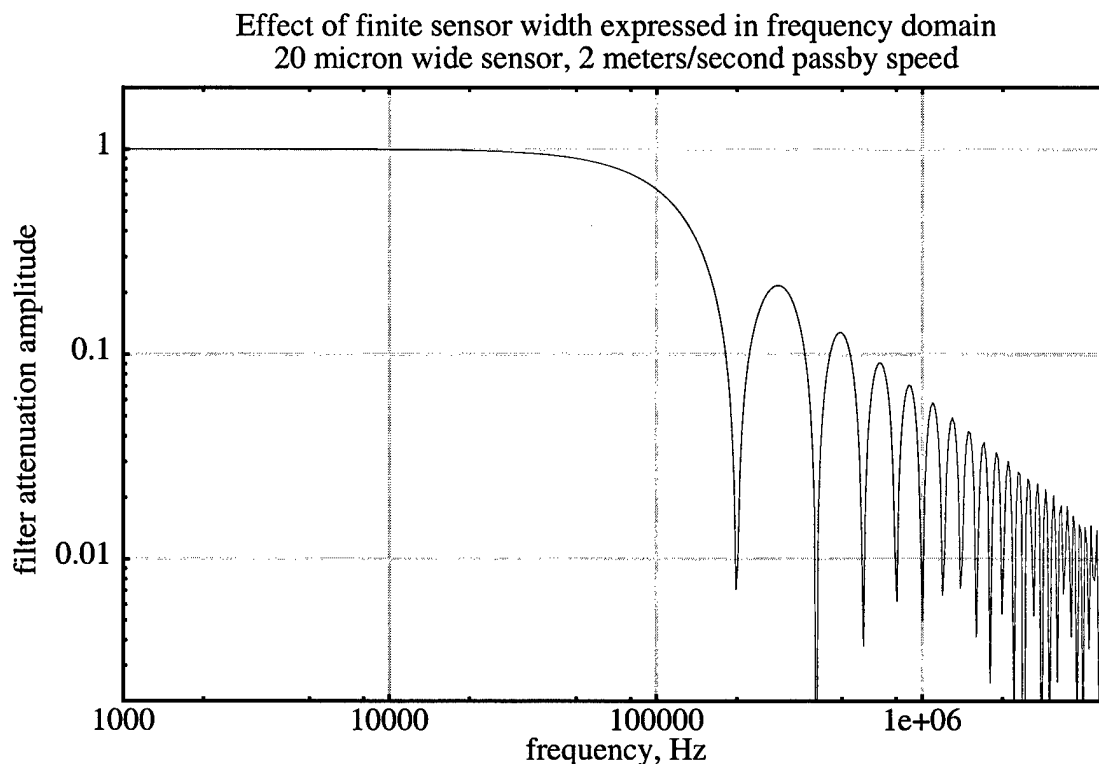


Figure 2.5: Response rolloff due to finite sensor width, shown in the frequency domain.

layer of a dielectric material, then another metallic layer are deposited. This sandwich structure closely resembles an ideal capacitor. The patterned metal film consists of three components: a slender sensor line whose resistance dominates that of the structure, and two stubby interconnect regions whose smaller aspect ratio reduces their resistances relative to the sensor line and whose large size means only a small fraction is in the EHD contact at any given time. Figure 2.6 is a schematic of the Wheatstone bridge used in signal conditioning. When the sensor passes through a contact, the sensor resistance changes slightly ( $O(0.1\%)$ ), but abruptly. Assuming negligible sensor inductance, the excitation pad remains at the excitation voltage. The slope of the potential/current path distance curve changes throughout the sensor line and ground-side pad.

The quick change in potential and the thin insulating layer combine to slow maximum sensor response. The electric field generated by the sensor voltage induces charge accumulation in the steel substrate near the sensor. The charge distribution is at a steady state until a component passes over the sensor. At this point, the sensor line and ground-side pad change potential, resulting in redistribution of the charge beneath them. This charge movement dissipates energy from the circuit. The simplest model for this

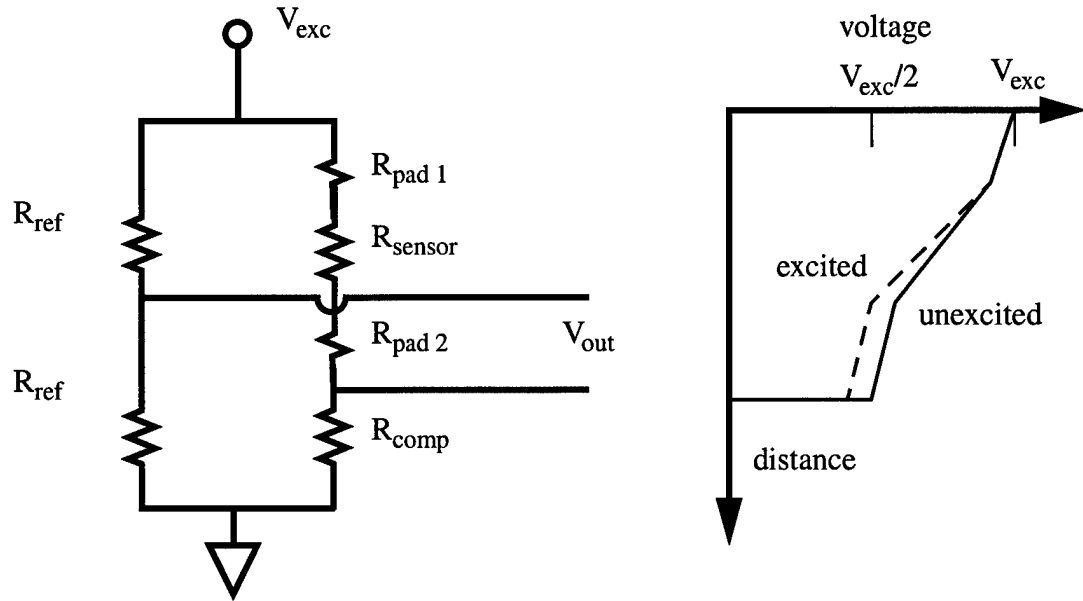


Figure 2.6: Wheatstone bridge schematic showing thin-film sensor and interconnect pads.

phenomenon is that of a distributed resistance/capacitance network. Solution of the indicated parametrically excited boundary value problem is challenging, but unnecessary. A much simpler lumped-parameter model is accurate if sensor and compensating resistors have much higher resistance than the sensor interconnect pads (typically a criterion for good design) and the sensor capacitance is negligible compared to that of the pad (true if the surface area of the pad is much larger than that of the sensor). Given these two assumptions, the model described in Figure 2.7 is accurate. The steady-state sinusoidal response amplitude of this system to a steady-state sinusoidal sensor relative-resistance fluctuation is given by

$$V_{out} = \frac{V_{exc} \left( \frac{\Delta R}{R} \right)}{\sqrt{\left( \frac{\omega RC}{2} \right)^2 + 1}}. \quad (2.10)$$

Figure 2.8 shows the frequency response indicated for the temperature sensor geometry and materials used in the most recent testing, with  $R=120 \, \Omega$ ,  $C=21.1 \, \text{nF}$  and  $6.4 \, \text{nF}$  for the current pad areas used over a 500 nm thick layer of PVD  $\text{SiO}_2$ .

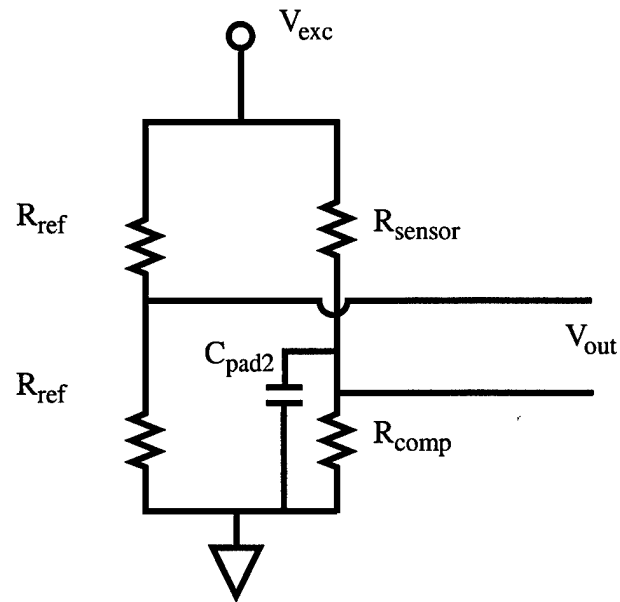


Figure 2.7: Lumped parameter sensor/bridge dynamic model.

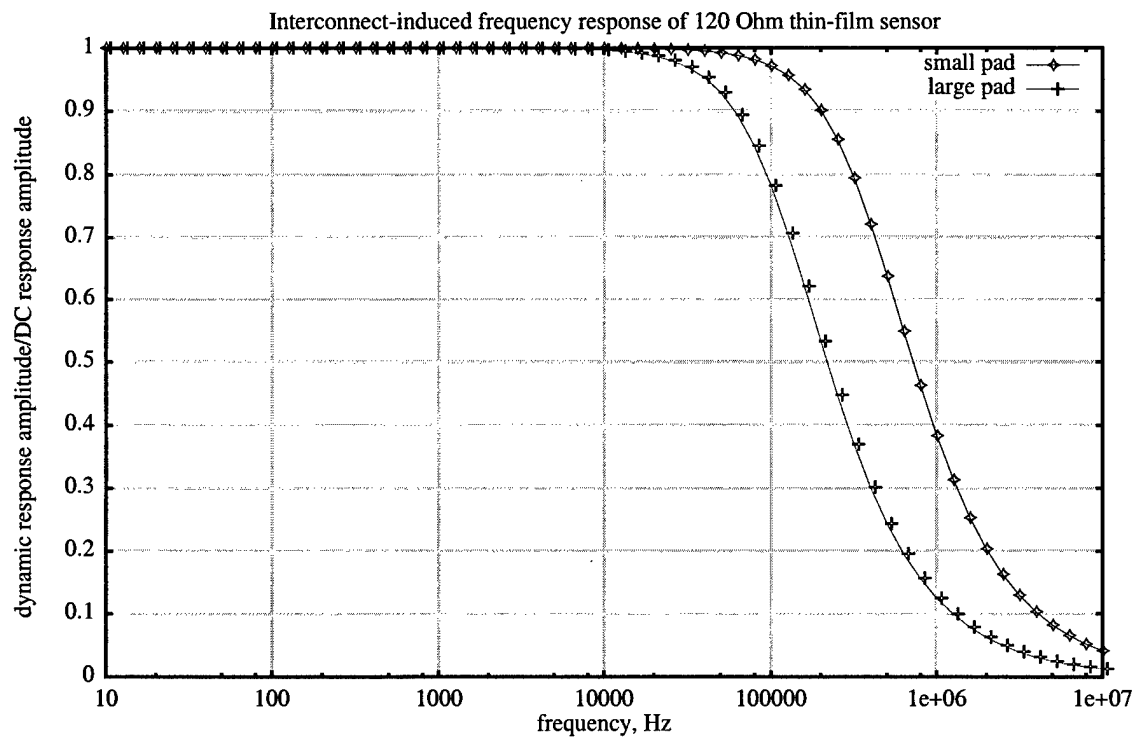


Figure 2.8: Simulated frequency response of 120 $\Omega$  thin-film resistive sensor

#### 2.4.5 System-imposed limits on contact sensor frequency response.

The final response-limiting design element concerns processing subsequent to the Wheatstone bridge. There are two principal areas of concern: amplification of the low-level (tens of microvolts) signal generated in the bridge, and digitization of the resulting high-level analog signal. Amplification is the more difficult of the two. An instrumentation amplifier is used to boost the differential signal generated within the sensor without applying significant gain to common-mode noise signals. The combination of  $100^+$  KHz bandwidth and thousandfold gain is not common, but was found in a device produced by Burr-Brown, the INA-103. A signal conditioner, consisting of an INA-103, switch-selectable resistors for gains of 100, 200, 500, and 1000, a variable bridge-completion resistor, and reference resistors was designed. Small signal bandwidth was found to be approximately 100 KHz, somewhat below the 800 KHz indicated in the manufacturer's literature. Digitization of the amplified signal is not a great challenge. According to Shannon's sampling theorem, a band-limited signal is fully temporally represented by a digital sequence sampled at twice the maximum frequency in the signal. This is easily done using the Purdue ME Tribology Laboratory (METL) Hewlett Packard 54501 digital sampling oscilloscope (DSO), which is capable of two-channel rates of 500 megasamples/second.

#### 2.4.6 Summary and discussion

There are three primary factors that influence the frequency response of thin-film EHD contact sensors: sensor linewidth, interconnect pad capacitance, and current instrumentation amplifier/data acquisition technology. In the design currently implemented, the limits associated with each of these areas are approximately equal, indicating a near-optimal design.

If the temporal performance of a sensor application is to be improved upon, each of the three areas will need to be addressed. Sensor linewidth can be reduced by a factor of two to three using higher-performance masks (technology already possessed by METL). Further improvement will require a reexamination of the photolithographic exposure procedure, with a limit at a five to tenfold reduction in linewidth. Interconnect pad capacitance can be reduced by a factor of ten by reducing the area of the pad. To do

this without making the pad resistance nonnegligibly large, another coating should be placed on or under the pad to increase its conductivity. Copper, with a conductivity 25 times that of titanium or zirconium and 70 times that of nichrome is a good choice with a target stocked by the Laboratory. If it is used, a separate deposition onto a region of the device will be performed. Prior deposition will protect the softer copper layer, subsequent deposition may facilitate soldering. A crude deposition mask can be used to avoid a second photolithographic operation. Development of a faster signal conditioner will require a jump from a monolithic instrumentation amplifier to one constructed from high speed operational amplifiers. A tenfold speed improvement will be achieved at the cost of a time-consuming design process and a possible increase in noise level.

## 2.5 Deposition of Thin Films: Precleaning and Sputtering.

### 2.5.1 Pre-deposition cleaning.

As delivered, most engineering surfaces are covered with a variety of contaminants. They are chemically diverse and attach to the surface by a number of different means. They are of concern because they modify the mechanical, chemical, and electrical characteristics of the deposited films. Cleaning, as defined here, is the removal or modification of kinds and amounts of contamination that prevent coatings from meeting desired performance parameters. It is typically a multiple stage process, with each step setting up a surface condition more amenable to the next.

The devices proposed for this study are wear-resistant resistors formed by chemical etching. Several common contaminant types can impair desired coating function. Particulate matter can induce pinhole defects that allow chemical etchants to attack the substrate [12,13,14]. Hydrocarbon films inhibit adhesion [15]. Adsorbed oxide films, if incorporated into the developing coating, can alter its resistive characteristics [59]. Ionic contaminants can change the surface mobility of the enucleating coating, thereby causing interruptions in the film [14].

Removal of surface contaminants is done by incorporating them into a medium for which they have greater affinity than the surface, by providing them with sufficient kinetic energy to desorb from the surface, or a combination of these.

Solvents are useful for the removal of ionic contaminants or hydrocarbons. Methods of application include spraying, immersion, and condensation from the vapor phase. Heating, mechanical scrubbing, spraying, or ultrasonic cleaning can be used to impart energy useful in desorption. Solvents low in undesirable contaminants (particles, nonvolatile dissolved substances) like deionized water should be used.

Soaps can be used in aqueous solutions to break up hydrophobic surface films. Soap molecules typically contain a hydrophobic group, which forms a low energy interface with the contaminant, and a hydrophilic group, which makes the two-layer surface film (soap over film) unstable and causes spheres with trapped contaminants inside of a soap outer layer to be released from the surface. Soaps are often incorporated into more complex detergent formulations that also contain agents that improve water rinsing characteristics and protect the clean surface from subsequent oxidation. Some of these compounds are useful in some contexts (preparing metals for painting, for example), but introduce surface films that are both difficult to remove and detrimental to the properties of subsequently physical vapor-deposited thin films.

Gas jets are used for the removal of particles and thick water or solvent films.

Three final cleaning steps can be performed with the substrate in the vacuum system. UV illumination is useful in decomposition of hydrocarbon contaminants. Heating of the specimen volatilizes adsorbed contaminants, increasing the efficiency of the vacuum as a cleaning agent. Plasma cleaning (also called sputter etching) uses bombardment of the substrate with an inert or reactive gas to increase volatility (through bond scission) and force desorption of thin hydrocarbon and oxide films.

Cleanliness can be assessed either in terms of the presence of defects in the deposited films or by use of surface analysis.

Based on the discussion above, the following cleaning procedure was developed. As-received parts have all visible traces of oil, dust, and other soils removed by wiping or mechanical scrubbing with a residue-free soap and water or a general

purpose solvent (unused Stoddard solvent, for example). Subsequent to this, parts are cleaned ultrasonically at 50°C (the temperature is described by Spring as high enough to melt medium weight hydrocarbons without crosslinking others) in an aqueous solution of a silicate-free alkaline detergent. Deionized (DI) water is used both for this and for an extensive rinse to be performed immediately after removal from the ultrasonic cleaning bath. These first two steps are to remove ionic elements and surface hydrocarbons. They are followed by a wipe of the surface to be coated with two trichloroethylene-wetted lint-free cloths to remove additional surface hydrophobic soils. After the part is placed in the vacuum system (using lint-free inspection gloves), it is blown off with clean, dry nitrogen or helium to remove as many of the fibers and particles clinging to the surface as possible. The vacuum system should be pumped down to its base pressure of 2 to 3  $10^{-7}$  torr to provide a clean chamber for plasma cleaning. Finally, the thin hydrocarbon/oxide surface layer is removed by an RF plasma clean with a bias of 50 Volts (chosen to be between the energy of chemisorbed and physisorbed contaminant bonds and the energy required for efficient transfer of materials in the RF workholder fixturing) for a period of 15 minutes or more.

## 2.5.2 Sputtering.

### 2.5.2.1 Introduction.

The theory of sputtering is described in Vossen and Cuomo [16] and in Parsons [17]. Sputtering is a physical vapor deposition (PVD) process, in which a energetic particle stream is directed onto a “target.” The kinetic energy of the impinging particles is transferred to surface atoms of the target, some of which break loose and form a flux of target material. The angular distribution of emitted particles is not characteristic of single hard-body collisions, instead more like a cosine distribution [18].

There are many ways of generating the incident particle stream. The one used in the work performed in this study is called glow discharge sputtering. This process uses a gas at a low pressure (1 to 100 millitorr) as a source of ions. The ions are generated by an RF or DC discharge, with the target attached to one electrode. A bias, or voltage difference, between the target and the plasma tends to accelerate the positive gas ions into



the target. This causes the ablation of the target surface and deposition of material onto nearby surfaces.

Deposition of thin films onto substrates is commonly done using three different technologies: evaporation, sputtering, and chemical vapor deposition (CVD) [19]. Of the three, sputtering places the fewest constraints on target material and results in the least substrate heating. Coherence of the deposited film and adherence to the substrate is typically much better than for evaporated films and can be somewhat worse than that observed with CVD. The films that are generated can have near-bulk density and accurate chemical stoichiometry.

#### 2.5.2.1 Gas and plasma properties in an RF (radio frequency) plasma.

This section supplies background on three topics important in the understanding of glow discharge sputtering, namely the kinetic theory of gases, the energy transfer functions for elastic and inelastic particle collisions, and the basics of ionization. The terminology and concepts introduced here are used extensively in future sections.

Glow discharge sputtering is a process that takes place in a moderate vacuum. Pressures in the gas are still sufficiently high to result in large numbers of gas/gas collisions compared to gas/chamber wall collisions, which satisfies a primary assumption underlying the kinetic theory of gases. The theory allows approximate determination of a number of useful microscopic variables from the global macroscopic variables pressure and temperature. The formulae in this paragraph are from Chapman [20] and O'Hanlon [21]. Mean and RMS particle speeds are fundamental microscopic variables, and are determined by equating the translational kinetic energy of a particle to its portion of the macroscopic thermal energy of the gas (it is implicitly assumed that no other degrees of freedom exist in the particle, something that may not be true, for example, in the case of non-noble gases). The resulting expressions are

$$\bar{c} = \left( \frac{8kT}{\pi m} \right)^{\frac{1}{2}} \quad \text{and} \quad (c)_{RMS} = \sqrt{\frac{3kT}{m}}, \quad (2.11)$$

where  $k$  is the Boltzmann constant and  $m$  the molar mass of the gas. Assuming random particle direction and elastic wall/particle collisions, the number density of particles is

$$n = \frac{3p}{m((c)_{RMS})^2} = \frac{p}{kT}. \quad (2.12)$$

The mean free path, or the average distance a particle must travel before encountering another, can be estimated by equating the specific volume of gas (volume per particle) with the volume swept out by a particle, which is the product of the particle crosssectional area and mean free path. One finds

$$\lambda = \frac{1}{\pi r_p^2 n}. \quad (2.13)$$

One important application of the mean free path is determination of the probability of collisions between sputtered particles and the process gas. As will be described, these collisions determine the energy with which the particles strike the substrate. Many collisions result in "thermalization," or loss of nearly all incident energy. This takes away the deposition energy advantage of sputtering over evaporation, and happens as mean free path decreases (or process gas pressure increases) relative to target-substrate distance  $d$ . Chapman (reference [20], page 10) derives the collision probability as

$$P \propto e^{-\frac{d}{\lambda}}. \quad (2.14)$$

As  $d$  approaches  $\lambda$ , thermalization rapidly occurs. This is good during substrate cleaning, as it prevents adherent contaminant deposition onto the substrate or target. Higher process gas pressure makes sense for this and other reasons. During deposition, process gas pressure is kept lower to enhance deposition energy and resulting adherence.

The kinetic theory of gases also permits the estimation of the flux of particles through a given surface in space. This flux can be expressed in many ways, including the monolayer formation time, the time required for a surface to be bombarded by a number of particles to form). An estimate of this time, which is important in the determination of permissible contamination, is

$$\tau = \frac{1}{n\bar{c}r_o^2}. \quad (2.15)$$

The second family of basic concepts deal with elastic and inelastic collisions. Glow-discharge sputtering works by the transfer of energy and momentum to the target surface, which results in the removal of a series of neutral particles. This energy is supplied to the system via a DC and/or RF electric field imposed on the target by a generator. It is converted to the kinetic energy of neutrals by the partial ionization of the process gas. The electrons and ions thus formed are accelerated in the electric field. Collisions of these with additional process gas atoms can be elastic, resulting in the transfer of kinetic energy only, or inelastic, resulting in the transfer of both kinetic and potential energy (an example of potential energy transfer might be ionization of the atom struck). The one-dimensional equations describing the transfer of energy in elastic and inelastic two-body collisions are

$$\left( \frac{\text{KE}_{\text{Transmitted}}}{\text{KE}_{\text{Incident}}} \right)_{\text{ELASTIC}} = \frac{4m_{\text{inc}}m_{\text{struck}}}{(m_{\text{inc}} + m_{\text{struck}})^2} \quad (2.16)$$

for the elastic case, and, for inelastic collisions,

$$\left( \frac{\text{KE}_{\text{Transmitted}}}{\text{KE}_{\text{Incident}}} \right)_{\text{INELASTIC}} = \frac{\frac{1}{2} m_{\text{struck}} v_{\text{struck}}^2}{\frac{1}{2} m_{\text{inc}} v_{\text{inc}}^2}, \quad (2.17)$$

$$\frac{v_{\text{struck}}}{v_{\text{inc}}} = \left( \frac{m_{\text{inc}}}{m_{\text{inc}} + m_{\text{struck}}} \right) \left( 1 + \sqrt{1 - \left( \frac{\Delta U}{\frac{1}{2} m_{\text{inc}} v_{\text{inc}}^2} \right) \left( \frac{m_{\text{inc}}}{m_{\text{struck}}} \right) \left( \frac{m_{\text{inc}} + m_{\text{struck}}}{m_{\text{inc}}} \right)} \right)$$

where  $\Delta U$  is the translational kinetic energy converted to another, unspecified form. For  $\Delta U=0$ , the elastic expression is recovered. There is a limit on the fraction of energy that can be converted and result in a system that still conserves linear momentum. This limit corresponds to the radical in Equation (2.17) becoming zero-valued, the velocity ratio half, and the energy transmission ratio one quarter of the elastic value. A comprehensive expression is thus

$$\frac{m_{\text{inc}} m_{\text{struck}}}{(m_{\text{inc}} + m_{\text{struck}})^2} \leq \left( \frac{\text{KE}_{\text{Transmitted}}}{\text{KE}_{\text{Incident}}} \right)_{\text{INELASTIC}} \leq \frac{4 m_{\text{inc}} m_{\text{struck}}}{(m_{\text{inc}} + m_{\text{struck}})^2}. \quad (2.18)$$

Two features of this expression are important to the upcoming discussion:

- 1) The efficiency of energy transmission in a collision depends on the ratio of the masses of the colliding particles, rapidly diminishing as this ratio deviates from 1, and
- 2) Much (75%) of the energy in the collision of two particles can be transferred to non-kinetic storage, such as ionization.

True gas dynamics takes place in a three-dimensional environment, with more complicated expressions for energy exchange. These two principles are more difficult to observe, but remain valid.

The third basic concept deals with different expressions for energy. Sputtering involves the exchange of energy between an external source, a plasma, several surfaces, and a cooling system. Sometimes this energy is best expressed in electrochemical terms (Volts or electron-volts), sometimes in thermo-mechanical terms (Joules), finally

sometimes in terms of a particle velocity (in momentum transfer contexts). Table 2.1 provides a comparison of values for several typically-observed situations

Table 2.1: Quantitative comparison of different energy expressions.

| Physical Situation                                   | Temperature,<br>°C | Thermal<br>Energy<br>$E=kT$ ,<br>Joules | Voltage<br>Drop, V | Argon atom<br>equivalent<br>speed,<br>m/sec |
|--|--------------------|---|--------------------|---|
| room temperature                                     | 20                 | $4.05 \cdot 10^{-21}$                   | 0.025              | 349   |
| upper bound on<br>temperature for<br>evaporated atom | 11300              | $1.60 \cdot 10^{-19}$                   | 1                  | 1550  |
| typical magnetron bias<br>voltage                    | $2.9 \cdot 10^6$   | $4.01 \cdot 10^{-17}$                   | 250                | 24600                                       |
| covalent bond strength                               |                    |   | 1.5 to 9.4         |   |
| ionic bond strength                                  |                    |   | 6.2 to 10.4        |   |
| physisorbed gas bond<br>strength                     |                    |   | 0.1 to 0.5         |   |
| chemisorbed gas bond<br>strength                     |                    |   | 1 to 10            |   |
| hydrogen bond energy                                 |                    |   | 0.1 to 0.4         |   |

#### 2.5.2.2 Process parameters.

Parameters that can be controlled in METL's sputtering system include process gas pressure, spiking oxygen gas pressure, target forward power, substrate forward power or bias, deposition time, target-to-substrate distance, the angle between substrate and target normals, and the conductance of the high vacuum valve at its "cracked" setting.

Process gas pressure has two primary effects on deposition. First, since target bombardment by gas ions causes material removal and ionization fraction varies little with pressure, the rate of material removal increases approximately linearly with pressure. Second, since typical sputtering pressures result in mean free paths of 0.1 to 10 cm, and typical target-to-substrate separations are on the order of 5-10 cm, the gas pressure can

result in a regime where sputtered particles travel directly from target to substrate or undergo many collisions. The first case produces the most energetic deposition and the densest film, the second is more diffusive in nature and more uniformly coats surfaces not on a direct line of sight with the target.

The process gas is normally noble (periodic table group zero, filled outer electron shell), because chemical reactions between the gas and sputtered material are in general undesirable. In some processes, though, a chemical reaction is by design part of the deposition process. One example is reactive sputtering, in which a ceramic coating is deposited by combining a sputtered metal with a process gas containing a reactive component like nitrogen or oxygen. Another is modification of the TCR of Nichrome by doping with oxygen added to the process gas [59].

#### 2.5.2.3 Deposition of durable films.

For pressure and temperature fluctuations to be sensed in the elastohydrodynamic contact, the sensor must survive pressures on the order of 10,000 atmospheres and requisite shear stresses of boundary lubrication as the instrumented device is started and stopped. Significant sensor wear, the loss or transfer of material, is not acceptable. Typical wear-resistant coatings are on the order of 5 microns thick -- typical sensing films nearer 0.05 microns. This section discusses the selection of materials and process parameters for deposition of wear-resistant films.

The most common model for metal and ceramic wear is the Archard equation [60], which states for applied pressure  $p$ , velocity  $v$ , and hardness  $H$ , wear rate  $W$  obeys

$$W \propto \frac{pv}{H}. \quad (2.19)$$

This model has one parameter controlled by material:  $H$ , the hardness, or resistance to plastic deformation under applied loading. Harder materials wear less quickly, so cheaper, softer materials are often coated to prevent wear. Coatings are applied by a number of methods, including electroplating, evaporation, and sputtering. Materials often employed

in wear resistant coatings include hard chrome (chromium), nickel, and oxide-, nitride- and carbide-based ceramics.

For wear to take place in the slow, uniform manner modeled by the Archard equation, the coating must both adhere to the material beneath and cohere to itself -- otherwise some form of gross delamination will occur. This is managed by selection of chemically compatible materials, production of a dense, continuous microstructure, and deposition under parameters that lead to a favorable residual stress state.

The bond formed between coating and substrate is partially chemical, partially physical. "Clean" surfaces are vital, since many common surface contaminants form a mechanically weak layer between coating and substrate which fails under loading. Plasma cleaning is often the necessary last step in cleaning, since oxides, hydrocarbons, and water inevitably deposit onto the substrate in air. Adhesion is best when the materials can form a hard alloy or compound and deposition is performed with enough energy to form this "graded coating" of substrate/alloy or compound/coating. A good example of this comes in the coating of glass (a mixture of alkali oxides) with copper or a noble metal. The first forms a weak oxide, the second no oxide at all. Glass coating with copper, gold or other noble metal is done by depositing two coatings: first a chromium, titanium, or another metal "interlayer" which forms a strong, stable oxide, then the desired metal, which bonds better to another metal than to glass. Techniques for enhancing coating adhesion are described in Bull [15].

Good cohesion in a coating depends on a continuous microstructure. The structure is influenced by initial wetting to the substrate [61], which can be improved by control of incident energy during the initial enucleation phase of film growth [89]. Once something close to a monolayer has been formed, dense growth is continued by the introduction of sufficient energy to promote adatom surface mobility. This concept, initially explored by Movchan and Demchishin [62] and by Thornton [63] is discussed in Bhushan and Gupta [64]. The authors noted that, depending on the deposition process parameters employed, the coating microstructure took one of several forms (Movchan and Demchishin had three, and Thornton four forms in their respective taxonomies). Two process parameters, inert sputtering gas pressure and substrate temperature, were used to construct a "map" of coating zones. At high pressures (where adatom thermalization occurs as discussed in Section 2.5.2.1), low substrate temperatures (which restricts adatom surface mobility), or a combination of these, the coating microstructure is sparse, with

discrete particles surrounded by voids. This is known as Zone 1 growth. As surface mobility is enhanced by reduced pressure and/or increased substrate temperature, the particles bind in a tough, fibrous structure, called Zone T (for transition). This zone is preferred for wear-resistant coatings, since it combines a favorable combination of hardness and toughness. A further increase in incident surface energy creates Zone 2 growth, which features a "columnar" grain structure. Still higher temperatures (these need to be near the melting temperature of the coating) result in Zone 3 growth, in which recrystallization of the coating material occurs on the substrate as the deposition process occurs.

Increased substrate temperature is not the only way to enhance surface mobility. Ion bombardment can be used to push a process nominally in Zone 1 growth into Zone T or Zone 2 without unduly increasing the temperature of sensitive substrates. This ion bombardment is a consequence of the introduction of a substrate bias, which ionizes the process gas above the substrate and accelerates process gas ions into it. Surface mobility enhancement is not the only consequence of bias-induced substrate ion bombardment, as is discussed next.

The equation for macroscopic coating durability is simple, at least in a qualitative sense. If the adhesive strength enabled by cleaning and promoted by physical and chemical bonding of coating to substrate exceeds the sum of applied and residual stresses, the coating continues to be a coating. If not, it quickly becomes debris over an uncoated substrate. Nowicki [65] discusses the effect of ion bombardment on residual stress state. Stress comes in two components: an intrinsic interaction between substrate and coating and a component based on deposition parameters [66]. Two factors compete to produce the deposition stress: process gas absorption into the growing film and the thermal gradient that comes from the absorption of the bombardment energy. Ion bombardment is an excellent example of the "more is not necessarily better" adage. As bias, for example, is increased, the stress in a film can go from neutral, to compressive, then to strongly tensile. The most desirable stress state is compressive and small enough to keep the overall (residual plus applied) state slightly compressive under typical loading. Compressive stresses that exceed the adhesion strength of the coating produce a buckled coating that looks much like a wrinkled sheet. Tensile stresses that exceed the adhesion strength result in a coating that cracks and flakes off of the substrate.



#### 2.5.2.4 Control of electrical properties.

Two electrical properties of the metal films deposited are of importance: TCR (thermal coefficient of resistance), and PCR (pressure coefficient of resistance). This section describes methods that can be used to vary the TCR and PCR of a specified material. These methods vary the TCR and PCR from values determined by the elastic restraint of the substrate and elastic properties (principally Poisson's ratios) of the film.

There are two deposition parameters that can be used to control TCR. The bulk material used in coating has an associated TCR. As film thickness decreases, the measured TCR becomes progressively smaller. As the film becomes discontinuous, the TCR curve goes through zero and becomes negative. Another way of making the film "discontinuous" at greater thicknesses is doping of the film with a reactive spiking gas during deposition [59].

Like TCR, PCR is a function of thickness [91]. As the film thins, PCR values become progressively larger. Very thin (discontinuous) films have large, but unstable values. Klokholm [92] also describes the use of residual stress to vary longitudinal strain resistance sensitivity.

#### 2.5.2.5 Layers deposited for EHD sensor fabrication.

Three layers are deposited to fabricate a pressure/temperature sensor pair on a steel substrate, with the first omitted in the case of glass substrates. The first is a 1.0 to 1.5 micron layer of aluminum oxide, whose purpose is to electrically isolate the conductive substrate from the conductive sensors above without a large change in thermal conductivity. Two coatings are deposited on top of this: first a 0.12 micron layer of zirconium for use as a temperature sensor, then a 0.04 micron thick layer of 80/20 nichrome used to sense pressure fluctuations. Physical masks are used to prevent coating of nichrome onto zirconium, except for a small region used to make external connections. Each coating is deposited using an AJA International A320 magnetron driven by an Advanced Energy RFX600/ATX600 13.56 MHz RF generator.

Steel substrates are coated using a three-step process. A high power plasma clean is followed by a low energy enucleation deposition and a high energy growth

deposition. The high power plasma clean is conducted at 26 mTorr, lasts 30 minutes, and is run under a substrate bias of -200V. After it, the specimen is maintained at a -30V bias and allowed to cool for 20 minutes. During this delay, the aluminum oxide target is warmed up for 10 minutes at 40 W forward power. After it, the target is ramped from 30 to 130 Watts in 90 second intervals (the 130W was chosen to keep power density at a value reported in Parsons [17] as below a target cracking threshold). Substrate bias is simultaneously ramped from 0 to -50V in -10V decrements. Pressure is maintained at 8 mTorr during the four hour deposition (the higher pressure increases deposition rate by increasing incident target plasma density without being high enough to render diffusion of the sputtered material dominant). After the four hour deposition, bias and power are ramped down in +10V and -20 W intervals. When 50 Watts forward is reached, the target and substrate RF generators are shut down. The total run is nearly as long as the life of liquid nitrogen in the vacuum system cold trap. To avoid blow-off of adsorbed water, the cold trap is recharged two hours after the onset of the deposition. The target/substrate distance is 79-81 mm.

The two metallization layers are deposited similarly. Target/substrate distance is 87-90 mm. Pressure is kept at 5 mTorr, a value large enough to insure a stable plasma, but kept as low as possible to maximize the energy of incident adatoms impinging on the target. Zirconium is deposited at 120 W forward power for 10 minutes, nichrome at 100 W for 5 minutes (the nichrome power is restricted to avoid an adherence problem noted with excessive residual stress). To obtain a uniform deposited thickness, the regions on the substrate to be coated are kept within the projected cylinder formed by the outer wall of the magnetron. Prior to coating, the substrate is plasma cleaned using a 10 minute exposure in 26 mTorr argon to a plasma that biases the substrate to -30V with respect to the ground terminal on the chamber wall. The metal gun is also warmed up during this interval by sputtering into a closed shutter, with 40W of forward power used.

## 2.6 Sensor Pattern Production.

The properties of the thin films deposited are critical to contact sensor manufacture. The films themselves, though, are insufficient. They must be patterned to form electronic devices through which measurements in property changes can be made. Three sensor patterning methods have been employed. The first, through-mask

deposition, places a pre-patterned metal foil mask between the deposition source and substrate. The second, laser etching, uses a pulsed infrared laser and computer-controlled table to melt and displace the thin surface film without inducing substrate damage. The third, photolithography, first patterns an organic film placed on the film, then uses a chemical etchant to remove parts of the metal film not protected by the organic cover. Each, in turn, is described in this section.

### 2.6.1 Through-mask deposition

One way to produce a sensor pattern on an insulated substrate is to deposit through a mask that obscures regions not to be coated. This is called through-mask deposition.

Deposition masks can be produced by two methods. De Silva et al. [34] describe the use of a pulsed laser system for the manufacture of metal foil masks for through-mask deposition. Masks can also be produced using photolithography (sometimes called photochemical machining or chemical milling, at this size scale). By either method, the mask should be designed for maximum stiffness near its smallest features.

Accurate transference of the mask geometry to the substrate requires the mask and substrate to be in close conformity. A gap as large as 100 microns (0.004") can provide enough clearance to diffuse the sharp sensor line into something much wider and more abrupt. To keep this gap small, the mask is pinched between the substrate and another object in close conformity to it.

### 2.6.2 Laser etching.

Laser patterning is another method to pattern the thin metal films of which the sensors are made. Unlike the other techniques, laser patterning affects only a small region of the metal film -- sensors are fabricated by cutting thin lines that interrupt the film. The heat used to melt and separate the film is equally capable of deforming or melting the substrate. To prevent this, the energy is introduced in the form of pulses short enough to

prevent significant thermal diffusion into the substrate. This allows patterning even of films whose melting temperature is higher than that of the substrate. Careful control of pulse energy has permitted patterning even over transparent dielectric films.

In the setup used, the laser optics are fixed. During the patterning operation, a two-axis table holding the sample is moved in the plane perpendicular to the beam. The table is computer-controlled, and permits speed-controlled motion over a pattern consisting of straight lines and described by the endpoints of these lines. Figure 2.9 contains an example program used to control the table.

|                    |  |
|--------------------|--|
| ^X SO              | Reset memory, load subroutine 0.   |
| +01010 +00100 4005 | Go to point (0.1010,0.010). Set speed to 5 in/sec.   |
| +01500 +00100 0    | Go to point (0.1500,0.010).  |
| +01500 +01000 0    |  |
| +01510 +01000 0    |  |
| +01510 +00100 2    | Go to point (0.1510,0.010) and stop.   |
| ^R RHS ^T          | Enter remote command entry mode, reset/move controller home/start, resume keyboard entry mode. |

Figure 2.9: Example program for computer-controlled table.

Figure 2.10 shows the components used to focus the laser energy onto the coated disk. The beam is first run through an attenuator to precisely control the output power level, expanded to reduce power density, then directed onto a focussing lens. A long focal length reduces defocussing due to beam/controlled table misalignment. To illustrate the importance of this, for a 75 mm lens a 0.001" change in lens/surface separation will change spot size 3.6 microns, a considerable fraction of the typical nominal spot size of 10-15 microns.

Both the coated disk and laser output are reflective. This results in multiple reflected beams between the laser and disk. These reflections tend to produce a broader spot whose size cannot be controlled by focussing the final lens. This undesirable effect is minimized by adjusting mirror and lens positions and orientations so the incident and reflected beams are as coaxial as possible. Before locking the focus lens in place, its distance from lens center to table center is approximately set, with an appropriate offset for sample thickness.

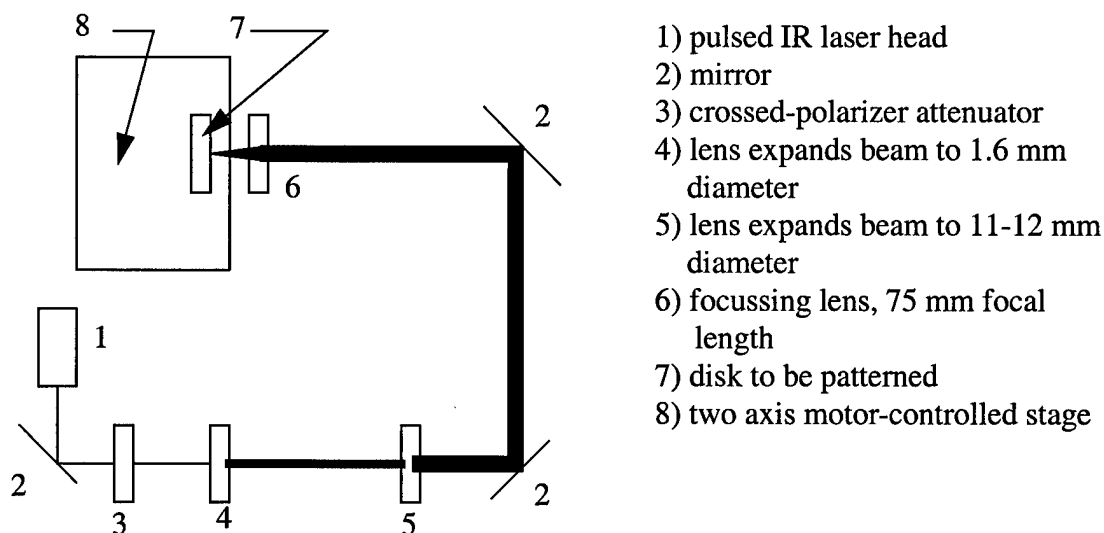


Figure 2.10: Schematic of laser patterning apparatus.

Once the in-plane adjustments were complete, intermediate tuning of focussing lens (6) is performed. An expendable sample of thickness close to that of the piece to be patterned is loaded onto the table. The attenuator is set to a low angle (approximately 15 degrees) and pulse power is set to 1.5W. The sample is set into motion so the pulsed beam continues to hit undisturbed areas on the sample. The lens/table offset is then slowly adjusted using a micrometer on the table. At this power level, when approximate focus is achieved, small sparks visible even through protective goggles are used.

Final focussing is achieved by patterning isolated holes at a much lower power (1.5W incident, attenuator angle near 83 degrees), measuring hole diameter using a microscope, and making minor adjustments in lens/table spacing.

Once focus is attained, pulse energy and focus are adjusted to achieve lines of the desired width. Selective defocussing can be used to increase line width -- this is desirable because the table is driven using a stepper motor which permits fixed 25 micron increments in position are possible. Narrow sensor lines are obtained by putting two cut lines next to each other. The width of this line is 25 microns minus the cut linewidth. Energy is varied to obtain a continuous line without inducing substrate damage. In tests at focus on nichrome films, with 1.5W laser output, an attenuator angle of 80 degrees induced substrate damage. An 87 degree angle was excessive, with negligible patterning. At focus, the same energy (84 degree attenuation) has been effective in patterning both 40

nm nichrome and 160 nm Zirconium films. Figure 2.11 depicts 40X optical interferograms of laser-etched patterns with excessive, sufficient, and inadequate pulse energy. In particular, note the bend in the fringes near the cut line when energy is excessive. This indicates residual substrate strain. A sensor patterned with this energy level tested on the optical EHD test rig (Section 2.11.1) suffered rapid delamination of the dielectric layer.

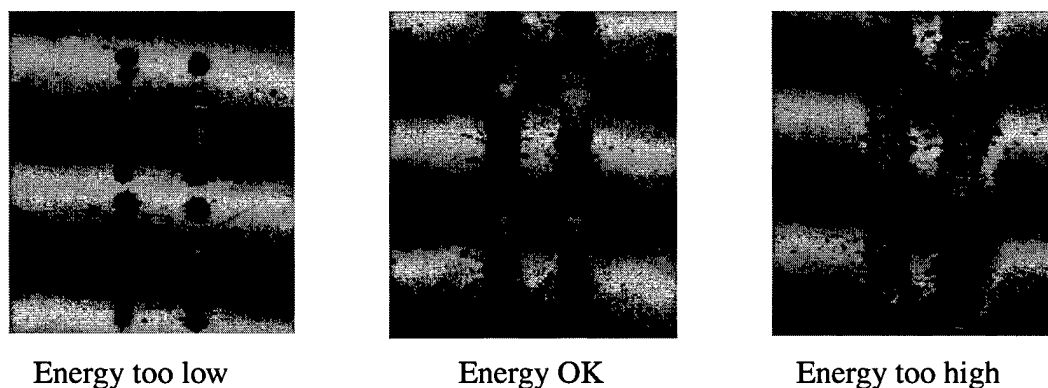


Figure 2.11: Interferograms of laser-patterned lines (40X).

One other parameter must also be set to achieve high quality patterns. Laser pulse rates of 1 to 999 pulses per second are available, although laser power begins to fall off at rates above 600/second. Even the maximum rate places 20 nanosecond pulses at least 1,000,000 nanoseconds apart -- no cumulative thermal effect due to multiple pulses has been observed. In light of this, the maximum possible full power pulse rate should be used. At low table speeds, this causes several pulses to hit a single area and minimizes local variations in line width.

### 2.6.3 Photolithography.

#### 2.6.3.1 Introduction.

Photolithography is the removal of select regions of a thin film or layer of material by generating a patterned layer resistant to etching, etching of the unprotected regions of the layer, and removal of the patterned protective layer.

Early in photolithographic process development, a photoresist system and etchant must be selected. These two choices, in turn, will determine issues as disparate as mask polarity (positive or negative), line width obtainable, and the capital equipment required for the patterning process.

There are two principal types of photoresists. Positive resists such as the AZ series (Hoechst Celanese Corporation, Somerville, New Jersey) protect the portions of the film covered by unexposed resist. Line resolution is relatively better than is observed for negative resists. They utilize a system less resistant to some kinds of chemical attack (aqueous alkalis in particular), which results in a film that restricts the set of potential etchants, but results in much more benign developing and stripping (photoresist removal) solutions. In contrast, negative resists like the KTI series (London Chemical, Bensenville, Illinois) develop thicker, more chemically resistant photoresist layers. For these, the exposed regions of the photoresist layer protect the film underneath from etching. The thicker photoresist layer reduces available resolution somewhat. The enhanced chemical resistance allows a wider variety of etchants, but increases the cost of both the stripping and developing formulations and of the capital equipment (fume hoods) required for their safe handling.

Photolithographic procedure is described by photoresist manufacturers. Holland and Tychsen [51] wrote a comprehensive description of their application in the production of EHD contact sensors.

### 2.6.3.2 Photomask generation.

The photomask is the template used to form a pattern in the photoresist. This pattern is transcribed to the thin film below by etching. Photomasks used on a microscopic level (for integrated circuit wafer manufacture) usually consist of patterned chromium films on flat glass substrates. Macroscopic photomasks (like those used in printed circuit board manufacture) are often printed onto film. The photomask pattern is developed either by photolithography (duplication of an existing master), photoreduction of artwork, or direct writing from a computer-controlled, traceable light source with a similarly controlled aperture.

Mechanical flexibility of the photomask is a distinct advantage in the case of EHD contact sensors, which are rarely flat. Film masks are therefore preferred. Typical EHD contact widths are on the order of 100-500 microns. To resolve parameter variations, sensors a few microns wide are desirable. This was typically done in the past by photoreduction of oversized master artwork. Printing technology has improved significantly, and direct printing is now possible. The newest generation of "imagesetters," high performance printers used in the graphic arts/printing prepress business, provide resolution and minimum linewidths on the order of 5-10 microns, direct printing onto films suitable for use in photomasks, turnaround of a few days, and costs of a few dollars per film.

### 2.6.3.3 Chemical etching.

At this point in the photolithographic process, the regions of the deposited films that are to be kept are covered with a lacquer resistant to the etching process. Etching may be done by sputtering, chemical removal, or a combination of these. Because of equipment constraints, only chemical etching is employed in this project.

The term "etching" in the context of thin-film electronic device manufacture implies the uniform removal of regions of a layer of one material. Implicit in this are that the etch not preferentially attack grain boundaries, that it not attack the substrate, photoresist, or other layers at a rate comparable to the layer, and that vertical etch rate is comparable to or greater than the lateral rate. Where etching is done in the context of a



photoresist-protected patterning operation, it is also important that the etching environment (composition and temperature) be compatible with the photoresist.

In the pressure/temperature sensors developed, Titanium and nichrome films with thicknesses on the order of 100 nm are to be removed from an alumina substrate. The substrate need not be considered when determining a nichrome etchant, as these chemicals have little effect on the alumina. It is significantly more difficult to find a substance that etches Titanium, but not alumina. Titanium is a reactive material that forms a tenacious, chemically stable surface oxide. This oxide, in turn, prevents attack by most chemicals to such a degree that Titanium is frequently used in chemical processing equipment. Many common etchants (nitric acid, for example) oxidize and passivate the surface, inhibiting the etching process. One ion capable of removing the surface oxygen is fluoride ion  $F^-$ , commonly used in an acid environment (hydrofluoric acid, or a fluoride salt combined with a weak organic acid). Unfortunately, these etchants also aggressively attack the aluminum and silicon oxide layers used to form electrical isolation layers.

A number of other aqueous solutions can be used to dissolve Titanium. They include alkaline/peroxide [67] and alkaline/peroxide/EDTA [68,69] combinations, and hot oxalic acid solutions [70]. One of these successfully employed in patterning Titanium thin-film sensors is a warm sodium hydroxide/hydrogen peroxide solution. Even weak alkalies attack the AZ1518 photoresist used in patterning (AZ developer is a weak alkaline solution). This problem was overcome by utilizing a relatively long, high temperature postbake to maximize photoresist crosslinking and chemical resistance [71]. As a consequence, photoresist strip became more difficult -- extended soaks in acetone, followed by gentle mechanical scrubbing with a plastic-bristled brush was needed.

Nichrome is difficult to etch in a manner that produces well-defined traces [72]. Berry et.al. [73] describe a sequential etch of dilute hydrochloric acid, cupric chloride, and ammonium hydroxide as an etch stop (chemical to abruptly inhibit further etching). Kern and Deckert [74] list warm 36° Baume ferric chloride, a mixture containing 6.3 M nitric and 3.9 M hydrochloric acids, and 9.3 M hydrochloric acid as potential agents. Rosenberg includes a 4.6 M HCl and 12%  $H_2O_2$  etchant for the chemically similar Inconel alloys[75]. The author has successfully used a chromium etchant consisting of 4 volume percent concentrated acetic acid and 10 weight percent ceric ammonium nitrate.

No studies in the literature were found describing chemical etching of zirconium for patterning, particularly in an environment where silicon or aluminum oxide insulating layers must survive the etch. Like titanium, zirconium is etched by fluoride systems. Unlike it, no other known formulations are available. A new etching system was developed and is described in the next section.

Depending on the characteristics of the layer etched and the nature of the photoresist layer, undercutting (removal of material under the edge of the photoresist) may occur. Well controlled, this can be advantageous, resulting in predictable linewidths less than those on the photomask and smooth film edges.

#### 2.6.3.4 Development of a zirconium thin-film etchant compatible with oxide insulators.

Zirconium is a metal with very low pressure coefficient of resistance and great chemical inertness. The first makes it very useful as a thin film temperature sensor in elastohydrodynamic contacts. The second makes photolithographic patterning of these same sensors difficult.

There is only one family of chemical etchants capable of dissolving zirconium: those based on the fluoride ( $F^-$ ) ion. The same etchants are used to dissolve the silicon or aluminum oxides typically used to form insulating layers in elastohydrodynamic contact sensors.

An etchant is still possible. This agent must be chosen to maximize the ratio of metal to oxide etch rate. To accomplish this, two etchant parameters are independently adjusted: total fluoride concentration and solution pH (acidity). Fluoride concentration influences etch rate of both metal and oxide. pH determines the relative concentrations of fluoride-bearing species ( $F^-$ ,  $HF$ ,  $HF_2^-$ ) and is used to adjust metal/oxide etch ratio. The remainder of this section describes the basis for etchant concentration determination and testing of the formulation so determined.

The proper fluorine-containing species should be maintained in solution. For relatively low  $HF$  concentrations with other acids added to reduce pH, Smith and Hill [80] found the etch rate for Zirconium well fit by the equation

$$\text{Zr etch rate (nm/min)} = A[\text{HF}] \quad (2.20)$$

where  $A \sim 6000 \text{ nm/min-moll}$  at  $33^\circ\text{C}$  for moderate stirring.

Value  $A$  was not dependent on  $[\text{HF}]$  concentration down to a value of  $0.0003\text{M}$ . It was, on the other hand, somewhat dependent on stirring (a vigorously stirred solution resulted in an approximately threefold etch rate acceleration) on temperature (Arrhenius relation, rate constant of about  $3 \text{ kcal/mol}$ ), and weak dependence on the type of acid used to adjust pH. Note here that  $[\text{HF}]$  is the concentration of undissociated HF, not that calculated based on the initial addition of hydrofluoric acid to the solution. The question of which species is actually responsible for the etch is probably not well addressed (one data point on page 118 of [80] indicates a  $\sim 20\%$  reduction in etch rate for a more basic solution buffered with KF).

In the case of  $\text{SiO}_2$ , Judge [77] and later Kikuyama et al. [79] state that the etching rate of the  $\text{HF}_2^-$  ion is approximately five times that of undissociated HF, and that the fluoride ion is relatively ineffective in dissolving  $\text{SiO}_2$ . In a study of  $1\text{M}$  fluoride solutions with different pH's, Judge found a simple rate equation of the form

$$\text{SiO}_2 \text{ etch rate} = A[\text{HF}] + B[\text{HF}_2^-] + C \quad (2.21)$$

with constants  $A$ ,  $B$ , and  $C$  taking the values shown in Table 2.2.

Table 2.2: Silicon dioxide dissolution rates in mixed fluoride species.

| T, °C | A    | B    | C     |
|-------|------|------|-------|
| 25    | 15.0 | 57.8 | -0.84 |
| 60    | 62.4 | 292. | -6.12 |

(as well as a more general, temperature dependent fit). Judge's Figure 1 indicates that, for pH not controlled by the introduction of hydrofluoric acid, the concentrations of  $\text{HF}_2^-$  and HF are equal for  $\text{pH} \sim 1$ , with more HF for lower and more  $\text{HF}_2^-$  for higher pH. For  $\text{pH} > 4$ , the proportional concentration of  $\text{HF}_2^-$  drops again, with  $\text{F}^-$  becoming the dominant

component. Notably, at a pH of 0 ( $1 \text{ M } [\text{H}^+]$ ),  $[\text{HF}] \sim 4 [\text{HF}_2^-]$ , with  $[\text{HF}_2^-]$  dropping off rapidly for lower pH.

A number of acids can be used to generate the lower pH needed to keep HF as the dominant specie in solution. Nitric acid is widely used in the HF pickling baths used in zirconium because it inhibits the formation of a hydride described in [78] that can cause stress corrosion cracking. It may not be the best choice in this case, since sputtered  $\text{SiO}_2$  films tend to be slightly oxygen deficient, and nitric acid is an etchant for silicon monoxide [76]. Sulfuric acid is another possibility, as a concentrated solution is somewhat effective as a Zirconium etchant. Hydrochloric acid was used in [80].

In an article for the ASM Metals Handbook, Yau [81] describes procedures for inhibiting corrosion of Zirconium in an acidic fluoride solution. One useful method is complexation of the fluoride with silica. This indicates that, if the surface area of the silica exposed to the etchant greatly exceeds the surface area of Zirconium to etch, the rate may dramatically decrease. Either a stop lacquer or plater's tape may be needed to mask off incidental areas of silica not masked with photoresist. Smith & Hill reported no notable increase in specimen surface area during HF attack, indicating a uniform etch (not, for example, pitting corrosion). Higher pH etchants should probably be avoided: acidic fluoride solutions are used to chemically polish (smooth) glass, more basic ones (a lot of ammonium fluoride with some concentrated hydrofluoric acid) to frost (roughen) glass [82].

The rate equations above indicate an etch rate on the order of 100 nm/minute of zirconium and  $<1$  nm/minute on  $\text{SiO}_2$  for a formulation consisting of 0.01 to 0.1 molar hydrofluoric acid basestock, with 2-molar hydrochloric acid added to maintain a low pH and inhibit formation of  $\text{HF}_2^-$ , slowing the  $\text{SiO}_2$  etch rate. If this were to be prepared from the standard concentrated acids, that would imply 165 mL concentrated HCl and 0.345 to 3.45 mL concentrated HF per liter of etchant. A more practical formulation would begin with two stock solutions: a *relatively* safe, low concentration 0.2 M HF (6.9 mL concentrated acid solution per liter solution) and 4 M HCl (330 mL concentrated acid/liter stock solution). The most concentrated etchant is formed by combining one part of each stock solution.

Two tests were run on the new etchant, one to ascertain PVD zirconium film etch rate, the other to determine the rate and nature of  $\text{SiO}_2$  attack. Both tests used microscope slides as substrates, with the slide used in the first test having a measured Zr film thickness of 35-40 nm deposited 3/21/97.

In the first test, the Zr film was etched in 15-20 seconds (estimated etch rate, 120-150 nm/minute). This was confirmed by etching the film on the opposite side of the slide. In the second test, a clean slide with electroplater's tape was immersed in the same etchant for 200 seconds. After etching, the slide was rinsed with water, the tape was removed, and the slide was cleaned using both acetone and trichloroethylene to remove any traces of adhesive from the slide surface. An interferometric microscope was then used to measure step heights varying from 85 to 95 nm, indicating an etch rate of 25-30 nm/minute and 8.5 to 9.5 nm  $\text{SiO}_2$  removed during a 20 second thin-film etch. The Zr etch appeared complete, and the  $\text{SiO}_2$  etch appeared to be uniform, with no evidence of pitting.

It would be irresponsible not to include a brief warning of the danger of hydrofluoric acid burns. The corrosivity of the mineral acids (e.g. hydrochloric, sulfuric, nitric) is well known, along with their tendency to boil water, spatter, and burn tissue. Hydrofluoric acid poses three additional threats. It rapidly penetrates skin, often leaving no immediate evidence of its passage. In sufficient amounts, it rapidly removes calcium from blood serum, inducing heart failure. Lesser amounts kill the tissue beneath the skin, resulting in necrosis and infection. Peripheral necrosis is sometimes treated with amputation of the affected limb. Abdominal necrosis has killed those exposed. Skin exposed to hydrofluoric acid must be treated immediately, aggressively, and sometimes in spite of symptoms. This treatment begins with rinsing, preferably with a calcium gluconate solution to neutralize the acid. At a physician's discretion, it may continue with subcutaneous injections of calcium gluconate. In brief, hydrofluoric acid should be treated with even more care than other concentrated acids.

#### 2.6.3.5 Photoresist strip.

The final step in photolithography is removal of the protective photoresist film. In this study, the Hoechst AZ<sup>®</sup> 1500 series photoresist chemistry is used [83]. Two types of chemical strippers are used to remove the film. If the post-bake step is at or below 120

°C, acetone will remove the layer. Photoresist layers baked to a higher temperature are not easily removed -- more aggressive strippers like Caro's acid or commercial products like Nophenol (Allied Chemical) are recommended. Acetone may still work in these cases, if the devices is soaked for several hours, then the photoresist is gently brushed with a nylon or teflon-bristled brush.

#### 2.6.3.6 Implementation of photolithography on glass disk substrates

This section describes how photolithography was implemented on the borosilicate glass disk substrates used to date in EHD pressure and temperature data collection.

The process begins just after deposition. The part is kept under vacuum until photolithography is to be performed. This is done because wetting was observed to be visibly worse on the zirconium temperature-sensing film after extended exposure to air, and that this reduction in wetting resulted in loss of adherence of the 25 micron sensing line on the temperature sensor. The disk is loaded onto a centrifuge capable of three second acceleration to 1300 rpm using two step clamps. Any observable fibers are blown off with a nitrogen gun. A yellow incandescent "bug lamp" is used to replace normal room lighting. A Pasteur pipette is used to apply a complete and uniform coating of Hoechst AZ1518 photoresist to the unclamped portion of the disk, a task that requires two-three pipettes for a normally receptive four-inch disk. The centrifuge is closed, accelerated to 1300 rpm within three seconds, and maintained at that speed (+/- 100 rpm) for two minutes. The centrifuge is then decelerated and the part removed.

The coated disk is prebaked in an 80°C oven for thirty minutes to firm the resist surface and drive off remaining solvents, then allowed to cool to room temperature (thirty minutes for a glass disk, nearer sixty for a steel disk). Cooling is important because exposure rate depends on resist temperature. A photomask printed using an imagesetter is used to generate the resist pattern. The mask is held against the disk surface, emulsion side in, using a blank glass photomask plate. The plate is affixed gently to the disk to avoid bending, which lifts the film mask and reduces line width. The resist-coated surface is then exposed the illumination from a Philips PL9W compact fluorescent ultraviolet

lamp for 130 seconds, with the sensor region at mid tube and at 45 degrees to the wide tube axis. The distance between the lamp center and disk center is kept at 42-50 mm.

After exposure, the disk is placed in a 150 ml 1:1 solution of AZ Developer and double-deionized (DDI) water for sixty seconds. The solution is gently agitated to circulate fresh developer over the disk. It is then rinsed twice in DDI water baths for thirty seconds to stop development. The developed resist pattern is inspected (typical resist thickness is approximately 1.5 microns) and post-baked at 120°C for one hour to harden the resist. Before etching, the patterned disk is allowed to cool to room temperature.

The nichrome film is etched first using a solution consisting of 10 w/o (weight percent) ceric ammonium nitrate and 4 v/o (volume percent) glacial acetic acid. The etchant is introduced using a Pasteur pipette to localize it (the etchants tend to soften the resist, use of the Pasteur pipette prevents softening of the resist over the zirconium film during nichrome film etching). Nominal etch rate is approximately 0.06 microns per minute. Just before the etch is complete, the film becomes intensely colored due to multiple-reflection interference. The etch is stopped by immersion in DDI water, and the sensor pattern inspected under optical microscope. Etching seems slowest in the channel containing the sensor line, making it the best region for inspection.

The acidified hydrofluoric acid solution described in Section 2.6.3.4 is used to etch the zirconium film. The etchant is formed by combining equal parts of 0.2 M (molar) hydrofluoric acid and 4 M hydrochloric acid solutions. Etching takes place by immersion, with a 0.07 micron/minute rate typical. After two minutes, the etch is stopped with a flow of DDI water, inspected, and, if necessary, continued.

After sensor patterning, the photoresist is easily removed using an acetone-soaked paper laboratory wipe. Both sensors are then inspected for thickness, width, length and uniformity using an interferometric microscope. After a successful patterning operation, external connections are formed as described in the next section.

## 2.7 Thin-Film Interconnects.

Short leadwires are used to connect thin film sensors to the external signal conditioner. The connection mechanism used must not disturb the electrical

characteristics of the underlying film, which is as little as 500 atoms thick. The contact resistance must be much less than the 100-500  $\Omega$  sensor resistance to maintain high signal-to-noise ratio, and must have a resistance noise much less than the m $\Omega$  to few  $\Omega$  fluctuations characteristic of contact parameter changes. Finally, the contact must be mechanically durable enough to support lead loading during part insertion and removal, as well as the thermal and mechanical stresses associated with operation and testing.

Four means have been used historically to connect sensors to leads. First, sensors can be sputtered onto a structure containing an existing bondable structure, like a conductor-bearing paint stripe or a thicker deposited metal film. Second, a compression-based bonding method like those used to connect semiconductor "dice" to package leads can be employed. Third, the film can be soldered directly to each lead. Fourth, a conductive adhesive can be used to attach lead to film. Of these four, only the last two have been evaluated. The first has not been tried because it adds process complexity: vacuum system compatibility in the case of the paint strip, another deposition step in the case of the additional metal film. The second requires additional equipment limited in its availability. It was used by Meijer, Schouten, and van Leeuwen [45]. The other two methods are describe below.

Soldering makes use of controlled heat, a flux, and a bonding metal with a low melting temperature. The warmed flux is used to displace oxides on the surfaces to be joined, then the molten solder forms a chemical/mechanical bond between the film and leadwire surface. Surface temperature and soldering time must fit within narrow ranges for a bond with good mechanical and electrical integrity. Insufficient temperatures prevent solder melting and integration into both surfaces, excessive ones deactivate the flux and oxidize lead and film.

Three solder-flux systems were used to form joints between nichrome, titanium, and zirconium thin films and tinned copper lead wires. The first system used was 60/40 tin/lead solder with integral rosin flux. This system is the workhorse of the electronics industry, but was not useful with any of the films. The chromium in nichrome, zirconium and titanium all form oxides much more tenacious than copper, oxides too durable for the rosin flux to displace. A second, more active system (Browning "High Force 44" solder and Eutectic 205 flux) used to solder high nickel/stainless steels was effective with nichrome. No joints could be made to zirconium or titanium due to incomplete oxide removal. The final system used was indium, with no flux. Indium is a



special solder in that it forms an electrically conductive, mechanically integral and adherent oxide. Indium can be used to make joints even to glass. Testing showed wetting to zirconium to be good on test samples, although none of the visual cues associated with a good joint were apparent.

The initial sensing films were deposited onto thermally-insulating glass substrates. Predictable heating was possible even with a low wattage temperature-controlled soldering station. The High Force 44/Eutectic 205 combination was used on both pressure (nichrome) and temperature (titanium, later zirconium) sensors -- with nichrome bonding pads sputtered onto the temperature sensors. Joints could be made, but not remade (a poor joint tended to destroy the metal film to which the bond was made). Later sensors were on thermally conductive steel substrates and included a 0.5 - 2 micron oxide insulating layer. The soldering process was developed concurrently with the insulating film deposition process, and no method was found during initial testing to controllably heat these substrates without thermally shocking and electrically disrupting the insulator. Problems with soldering forced a look for an alternative.

Conductive adhesives were tried very early in the research program, even before the metallization process was worked out. A two-part room temperature epoxy paste was tried on a glass slide that was tested for pressure response in a high pressure chamber. Contact was highly variable during and subsequent to the test, and the bond was mechanically weak. Adhesives were not therefore pursued in glass-substrate testing. When soldered joints became problematic adhesives were reviewed. The most stringent selection criterion was the high (165°C) temperature used in the 24 hour thermal aging bake of the resistor films. Few conductive adhesives are rated for this. One, Acheson Colloids Electrodag 5915, has been mechanically durable, electrically consistent, and chemically resistant to lubricants and cleaning agents. A sufficiently long curing cycle is needed, and, due to substrate thermal mass, this has been as much as double the manufacturer's recommendation. This has been easily accomplished by performing lead attachment during the thermal aging bake.

## 2.8 Thermal Aging Bake

The sensors formed to measure elastohydrodynamic contact parameters are thin-film resistors. Metal film resistors, also produced by physical vapor deposition, are used in electronic applications where precise value and predictable thermal coefficient of resistance are important. As deposited, metal film microstructure and contaminant concentration change, and both value and TCR tend to drift with time. Before resistors are shipped, they are "aged" by extended elevated temperature operation [84]. Aging is an exponential process, with the most rapid change at the beginning. Within reason, higher temperatures increase the aging time constant.

Aging in elastohydrodynamic contact sensors involves a compromise. The same extended temperature increase used in aging also softens heat-treated steel. AISI E52100 steel is the material most typically used in bearing applications. Based on a NASA study [87], a 24 hour, 165°C exposure does not result in a significant loss of hardness in E52100 steel.

## 2.9 Signal Conditioning.

The sensors described in this chapter slightly change resistance under external pressure and temperature fluctuations. Most general-purpose laboratory data acquisition equipment measures voltage fluctuations with a high-impedance input device -- the high speed digital storage oscilloscope employed in this study is no exception. A device must be used to offset the nominal resistance of the sensor, convert resistance changes to voltage changes, and amplify small signals. In this work, this is done using a low-noise excitation supply, a Wheatstone bridge, and a monolithic wideband instrumentation amplifier.

The dynamic aspects of signal conditioner design were discussed in Section 2.4.5. Implementation details are presented in Section 2.11.2. Two factors remain and are described here: nominal DC conditioner transfer function and selection of excitation voltage.

Figure 2.12 is a schematic of a Wheatstone bridge. The equal-valued reference resistors divide the excitation voltage (and any noise on it) by two. For changes

in sensor resistance small compared to its value, the bridge output voltage is approximately one fourth of the relative sensor resistance change.

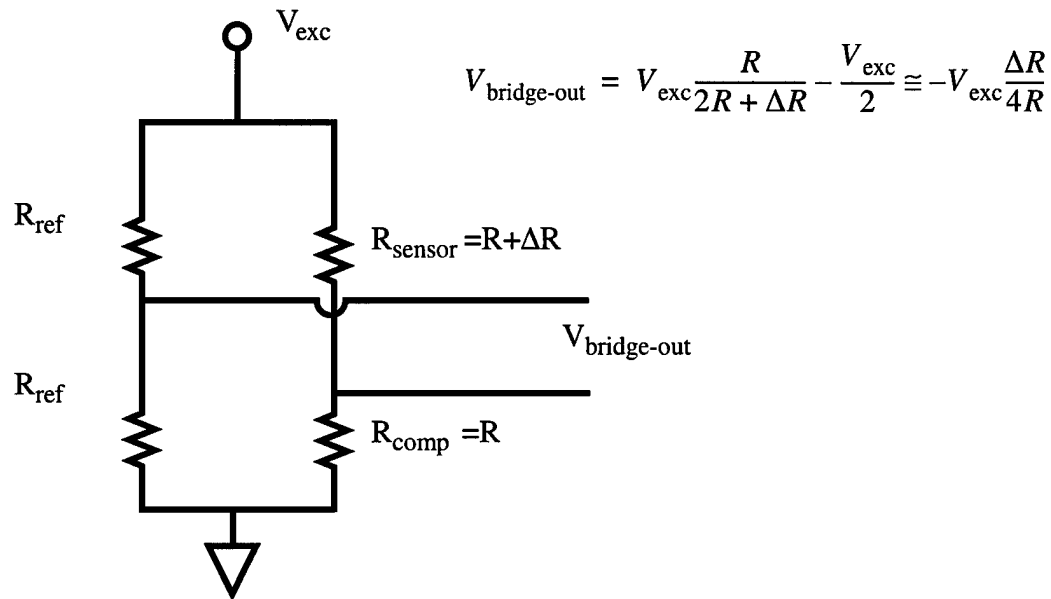


Figure 2.12: Schematic of a Wheatstone bridge.

The signal conditioner includes an amplifier with gain  $G$ . This gain increases the bridge output voltage to the signal conditioner output voltage

$$V_{\text{out}} \cong -GV_{\text{exc}} \frac{\Delta R}{4R} \quad (2.22)$$

There are two ways to amplify the sensor output signal: either the excitation voltage  $V_{\text{exc}}$  or the amplifier gain  $G$  can be increased. Excitation voltage is preferable, as it increases the size of the signal without boosting noise levels. There is an upper limit on excitation voltage discussed next.

Early tests on glass disks showed pressure signals of appropriate magnitude, with features characteristic of elastohydrodynamic contacts included. The output of the titanium thin-film temperature sensor was more difficult to explain. As the sensor passed through the contact, the temperature decreased instead of the anticipated increase due to compression heating and viscous shear.

Sensor self-heating was considered early in the design program, with an estimate of maximum allowable excitation voltage based on power densities listed in Dally and Riley [85] for strain gauge installations. The model was not well chosen. The films used to manufacture strain gauges are thicker and occupy a much larger surface area than the single-filament gauges used to measure EHD contact parameters. An easily employed, but more accurate, model was found in Rohsenow, Hartnett, and Ganic [86]. The authors describe the transient thermal response of a semiinfinite body under transient heating of a circular patch (geometric accuracy is traded for a quick solution). Convection is neglected, which makes the solution accurate only until if substrate heat dissipation dominates. Use of a circular patch of area equivalent to the sensor line results in a sigmoidal temperature-time curve. The steady-state temperature is achieved in 2.5 to 3.0 msec. The heat flux is proportional to the square of excitation voltage. For the BLH 5100 series strain gauge signal conditioner used before the unit described in Section 2.11.2 was built, the minimum available excitation voltage was 3V and resulted in a heat flux of 2.3 MW/m<sup>2</sup> and a predicted steady-state temperature rise of 80°C. In general, the Rohsenow/Hartnett/Ganic conduction model predicts a steady-state temperature and time constant

$$(\Delta T)_{ss} = \frac{V_{exc}^2}{4\sqrt{(\pi w l)k}R_{sensor}} \quad \text{and} \quad \tau = \frac{wl}{\pi\alpha} \quad (2.23)$$

(here  $w$  and  $l$  are the sensor line width and length,  $k$  and  $\alpha$  are the thermal conductivity and diffusivity of the substrate material, and  $R_{sensor}$  is the sensor resistance). Application of the model made excessive self-heating appear to be a likely possibility. The signal conditioner was modified to reduce excitation voltage enough to maintain a predicted steady state temperature increase below 1°C.

### 2.10 Calibration.

Before use, both temperature and pressure sensors are thermally calibrated. To date, pressure sensitivity has been determined in-situ. Procedures and results are outlined in this section.

### 2.10.1 Thermal calibration procedure.

Sensors are calibrated through one complete heating cycle to 80-90°C. Resistance is monitored to five significant digits. Heating was performed in a temperature-controlled oven, with the sensors immersed in a viscous, inert fluid (DuPont Krytox™ AB perfluoroalkylpolyether lubricant), with the sensor surface vertical to minimize thermal convection currents. The temperature control is slowly adjusted to keep bath temperature, which is measured with a thermocouple immersed in the oil, and sensor temperature close. Total up-down cycle time is approximately 5 hours.

A representative calibration curve is shown in Figure 2.13.

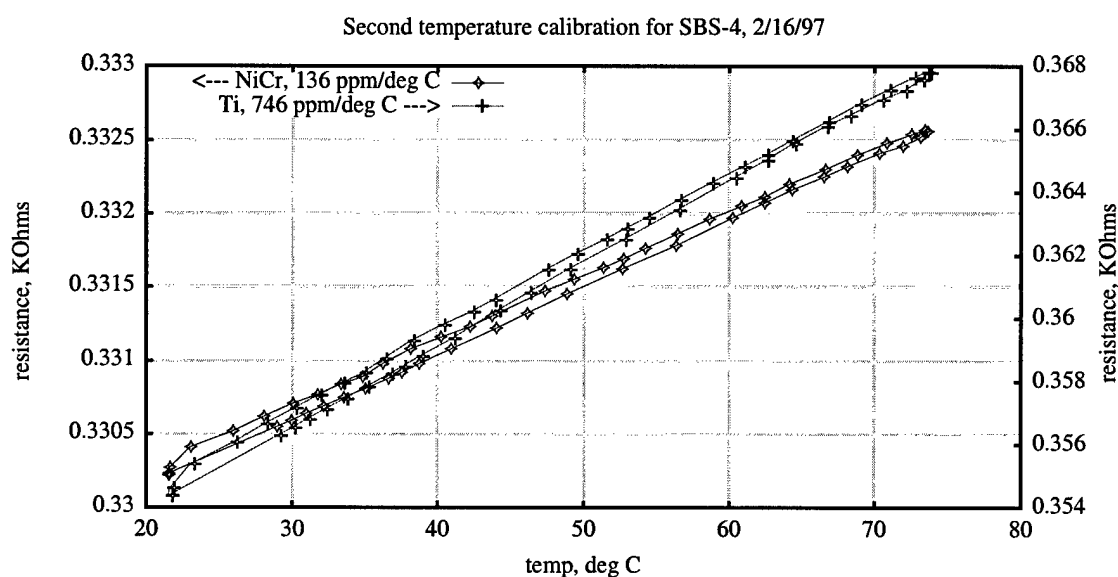


Figure 2.13: Typical thermal calibration curve of pressure and temperature sensors.

### 2.10.2 Pressure calibration procedure.

Pressure calibration has, to date, been done by running instrumented disks on the optical rig described in the next section at zero slip (ball and disk surface speeds equal). Other authors have employed static calibration, either by loading the sensor with an interposed insulator (often paper or film) or using a high pressure chamber like the one described in [40]. Both Safa [35] and Orcutt [22] found better correlation to a

dynamically derived pressure coefficient of resistance than to the static one they measured, both attributing the difference to a non-hydrostatic element in loading.

For operation at zero slip, the main lobe of the pressure distribution is well described by Hertz's no-friction dry contact model. Given the dead-weight load acting on the machine, a maximum Hertzian contact pressure is computed and equated to the experimentally-observed main-lobe peak.

### 2.11 Testing

Testing of thin-film pressure and temperature sensors has been performed in a rig initially designed for optical measurement of oil film thickness. The sensors were deposited onto glass disks like those used in film thickness measurements, then loaded, rotated, lubricated and tested. The subsequent sections describe the test rig, signal conditioning, acquisition, and processing hardware and software, and provide exemplary test results.

#### 2.11.1 Description of Test Rig.

Figure 2.14 is a schematic of the core of the optical EHD test rig used to collect data on instrumented disks. The test rig provides an environment in which a load is applied, the speeds of the disk holding the sensors and the ball it runs over are maintained, and lubricant is provided. To expand, the rig has two perpendicular shafts, a fixed shaft in the horizontal plane and a vertical shaft free to slide up and down, onto which weights can be applied through a stationary hanging spindle. Each is driven by an induction motor with variable speed drive. A disk with two thin-film sensors is loaded onto the vertical shaft, a ball onto the horizontal shaft. A small lubricant reservoir viscously feeds the lower side of the driven ball, and is continuously replenished using a peristaltic pump. Spent lubricant is recycled. Hertzian pressures from 0.8 to 1.4 GPa are possible (exact levels depend on the composition of the ball and disk). Speeds from 0.5 to 4.0 m/sec with slip from 0 to 20% can be stably attained.

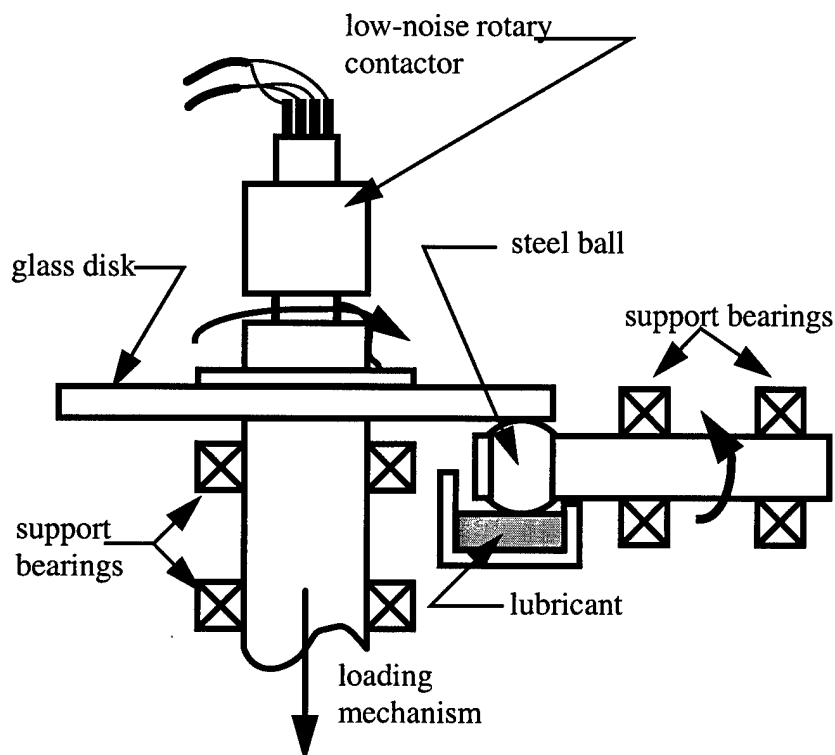


Figure 2.14: Schematic of optical EHD rig core.

Two sensors, one pressure- and one temperature-sensitive, can be monitored simultaneously. Signals are passed through a low-noise rotary mercury contactor to an external signal conditioner. Acquisition is triggered using an infrared retroreflective sensor (open collector output) in front of which a strip of aluminum foil passes.

#### 2.11.2 Signal Conditioning, Data Acquisition and Post-Processing.

Signals are passed through the rotary contactor to a signal conditioner, then to a HP54501 digital sampling oscilloscope. Files generated are passed on to the departmental mainframe, where a postprocessing and deglitching program are used to postprocess the data. Each of these is described in this section.

The signal conditioner consists of three blocks: a low-noise excitation supply, a Wheatstone bridge compensation network, and a low-noise wideband instrumentation amplifier. The excitation supply uses a Burr-Brown REF102 voltage reference with an OPA27 low-noise operational amplifier as a buffer and low-pass filter. The output

network permits one or two times a resistor-selectable excitation voltage (currently set at 0.1V). The bridge compensation network consists of two fixed  $499\Omega$  resistors to form a half bridge, and an active half-bridge consisting of the sensor in series with a  $1\text{ K}\Omega$  wirewound variable compensating resistor (as designed, the compensating resistor is on the ground side of the bridge). The non-resistive reactance of the compensation resistor was initially of concern, but testing showed negligible phase shift over the frequency range of interest (DC to 300 KHz). The output of the excited bridge is fed to a Burr-Brown INA103 wideband instrumentation amplifier. Gains of 100, 200, 500, and 1000 are switch-selectable. Testing of the amplifier shows a cutoff frequency of 100 KHz at a gain of 1000, with some tendency toward intermittent oscillation near the cutoff frequency.

The output of the signal conditioner is passed to the HP54501 digital sampling oscilloscope (DSO). The oscilloscope is run in a sequential burst sampling mode triggered by the output of the optical shaft sensor. Sequences of about 30 sequential triggering events are collected, with 4000 points in each. Data is sampled to eight-bit accuracy and, after collection to memory is stored on a DOS-formatted diskette drive (each single channel data file is approximately 250 KB in size).

The data stored from the DSO is transferred to the department's mainframe computer. There, a program is used to reformat the oscilloscope's binary file, time-shift signals from two sensors to phase-align them, present all of a file pair's data in an animated format, and generate selected segment voltage/time records for subsequent processing.

With the glass disks used, the excitation voltage level must be kept low to avoid undesirable sensor self-heating. This results in very low bridge output levels ( $O(1\text{ mV})$ ) produced in close proximity to two relatively noisy motor drives. Single-point grounding of the drives, scope, and signal conditioner have reduced electrical noise greatly, but transient spikes are still readily apparent in the data. In-line active filters can smooth these somewhat, but produce as output broader pulses (essentially the impulse response of the filter) that look much like valid data. Less invasive deglitching was performed using a program that operates in the time, rather than the frequency domain. Each data record is looked at as a sequence of vectors. The program replaces sequences of length less than a specified value that leave the neighborhood of an interpolating line, then return to it, with interpolated straight segments. In effect, glitches are removed without disturbing the surrounding data.



### 2.11.3 Results.

To date, data have been collected using a combination of borosilicate glass and AISI E52100 steel disks, both 4 inch diameter, 1/4 inch thick as substrates. Seventeen figures are included to represent the database collected.

Two figures show the correlation between experimental measurements and the results of a thermal elastohydrodynamic contact model developed by Dr. Gang Xu, formerly of the Purdue/METL [88]. Dr. Xu's model operates on a space domain transformed to time for these plots given the known surface speed. His domain is relatively short, which explains the longer experimental than analytical record. The first plot (Figure 2.15) shows a comparison of measured and simulated pressure response in the EHD optical rig. Analysis of elastohydrodynamic contacts shows contact pressure to be relatively insensitive to slip. The apparent depression in the pressure curves is more likely due to thermal cross-sensitivity (the pressure coefficient of resistance of the nichrome films deposited is negative, the temperature coefficient of resistance positive) than to a change in the pressure distribution. Temperature fluctuations are more sensitive to slip variation. These are shown in Figure 2.16 for three different values of slip: 0% (pure rolling, no sliding), 10%, and 20% slip. In each case, the slip was obtained by reducing the speed of the ball in the optical rig: the speed of the disk (and sensor) was unchanged. These data were taken using a glass substrate. Temperature increase is more responsive to the change in substrate. Figures 2.17, 2.18, and 2.19 show correlation of analytical and experimental temperature distributions using a steel disk.

METL has an ongoing research effort underway to analyze grease lubrication. Here "grease" refers to the combination of a base oil, which may be mineral or synthetic, and a thickener, often a soap or clay. As a part of the program, several greases were evaluated early in the research program, before improvements to the signal conditioner made the titanium, later zirconium temperature sensor useful. The most immediate question was the role played by the thickener in the pressure response. Ideally, a grease should behave like an oil (the thickener is intended only to serve as a lubricant holder and wick). There was a possibility that thickener particles could be extruded through the contact, resulting in a broader pressure profile and lesser peak pressure.

The two subsequent figures show pressure sensor response at two different speeds (1.5 and 2 m/sec) and three different applied loads (0.74, 0.81, and 0.87 GPa).

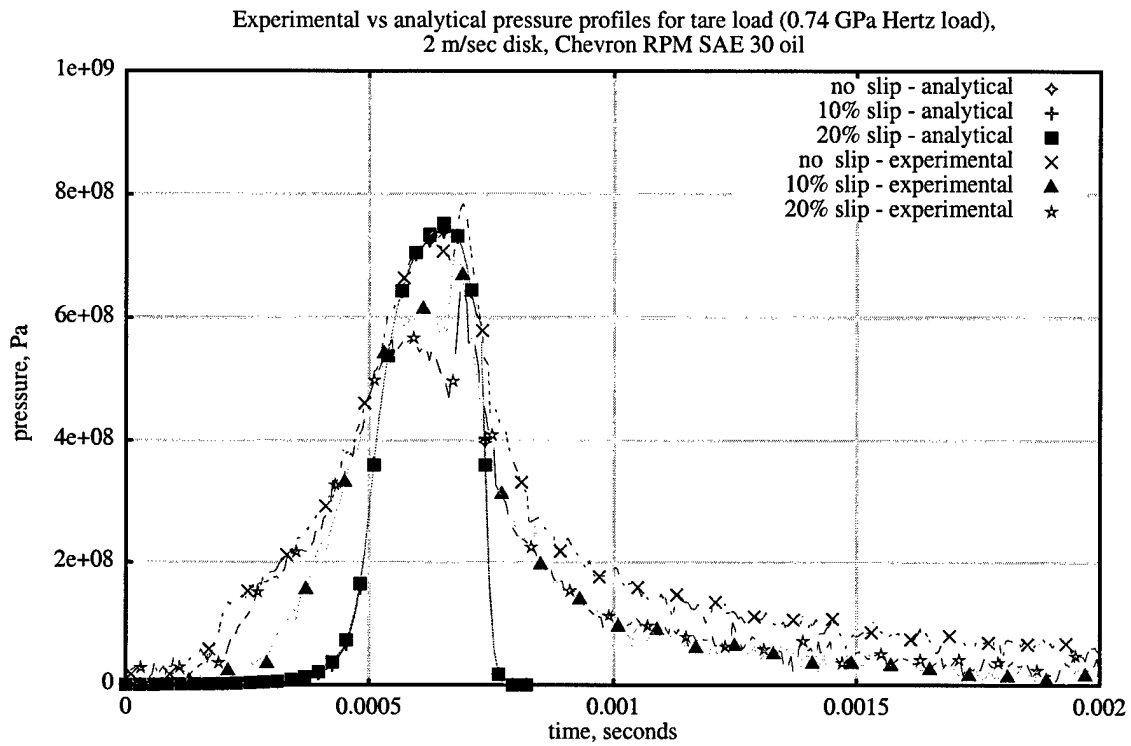


Figure 2.15: Comparison of analytical and experimental pressure estimates.

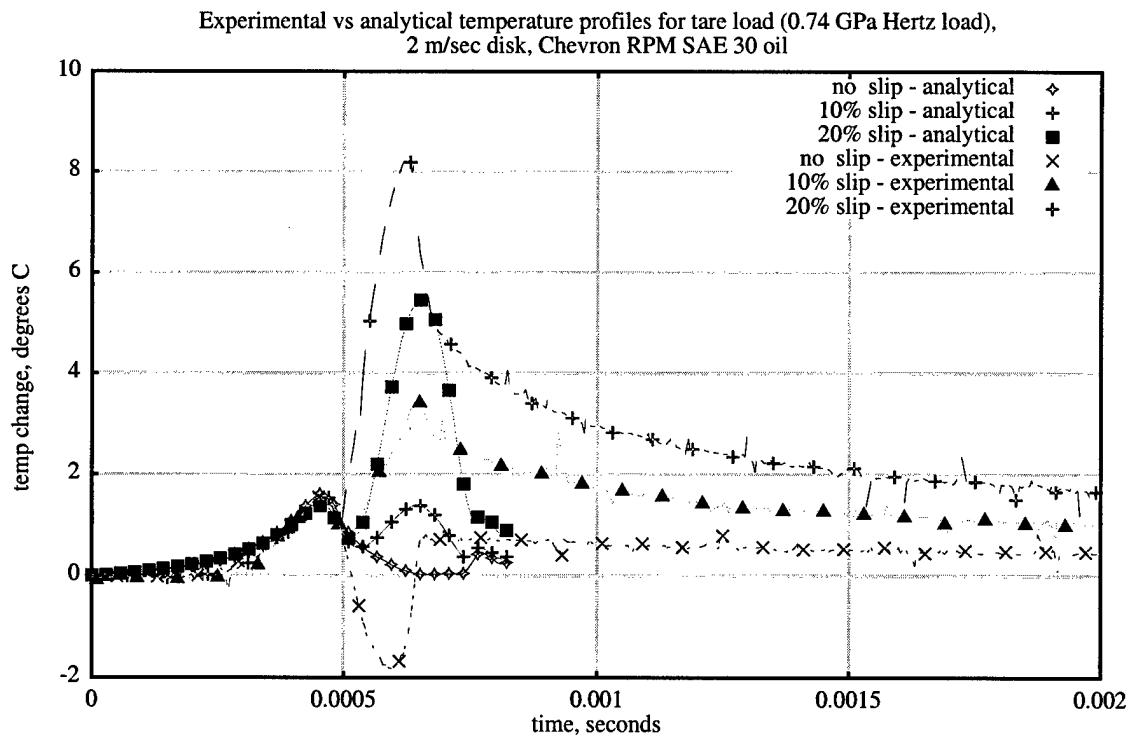


Figure 2.16: Comparison of analytical and experimental temperature estimates.

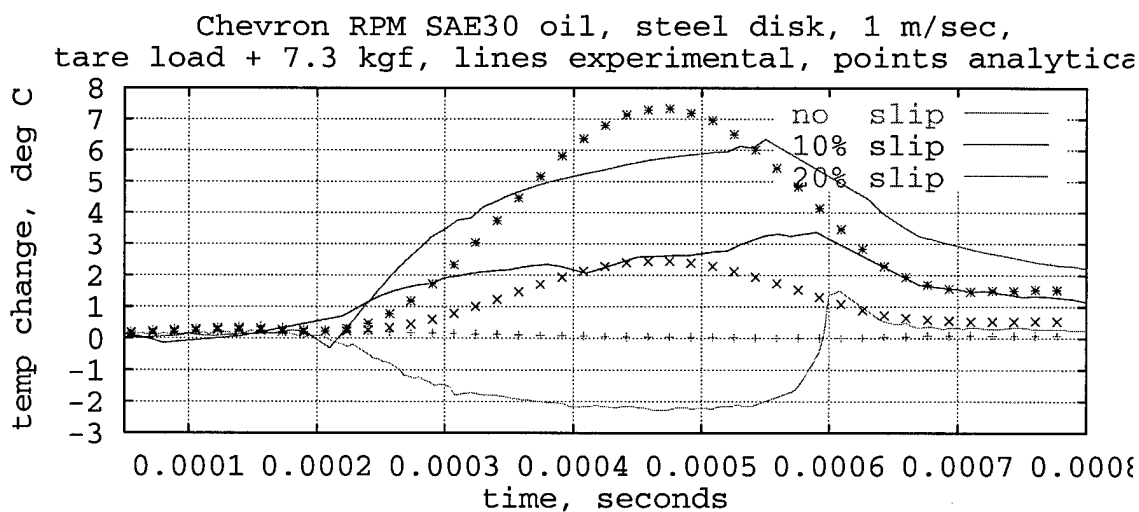
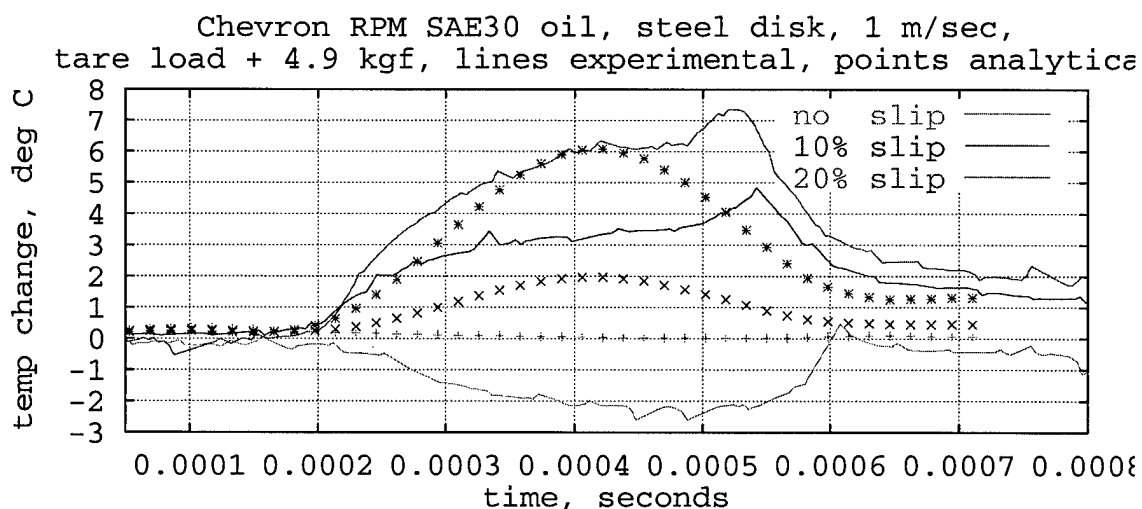
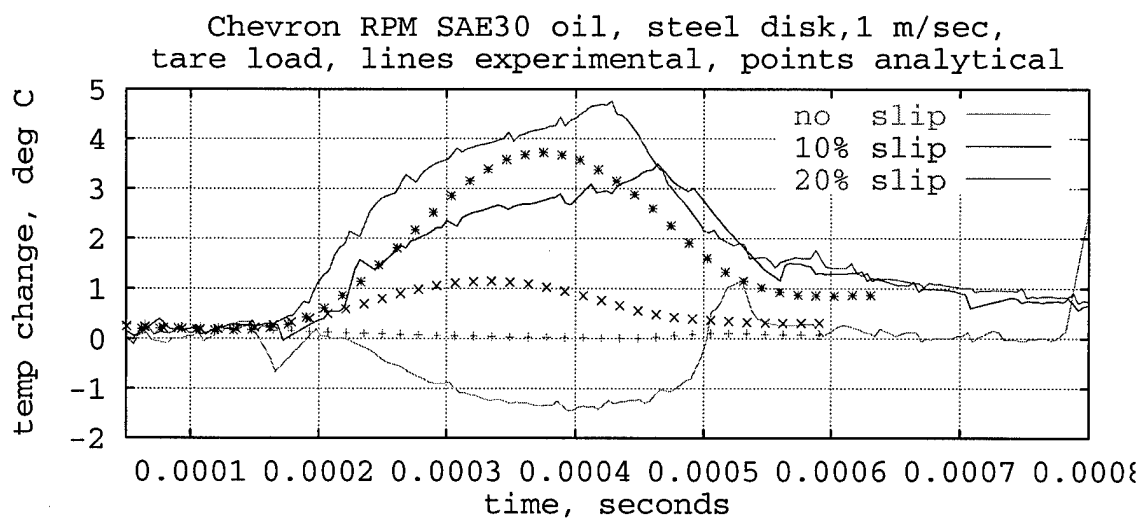


Figure 2.17: Comparison of analytical and experimental temperature transients (1 of 3).

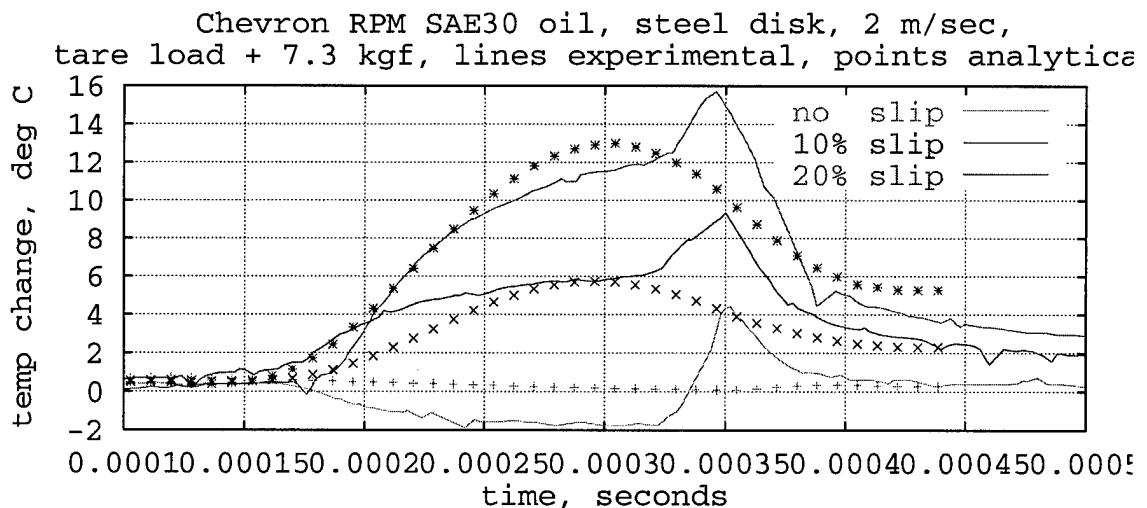
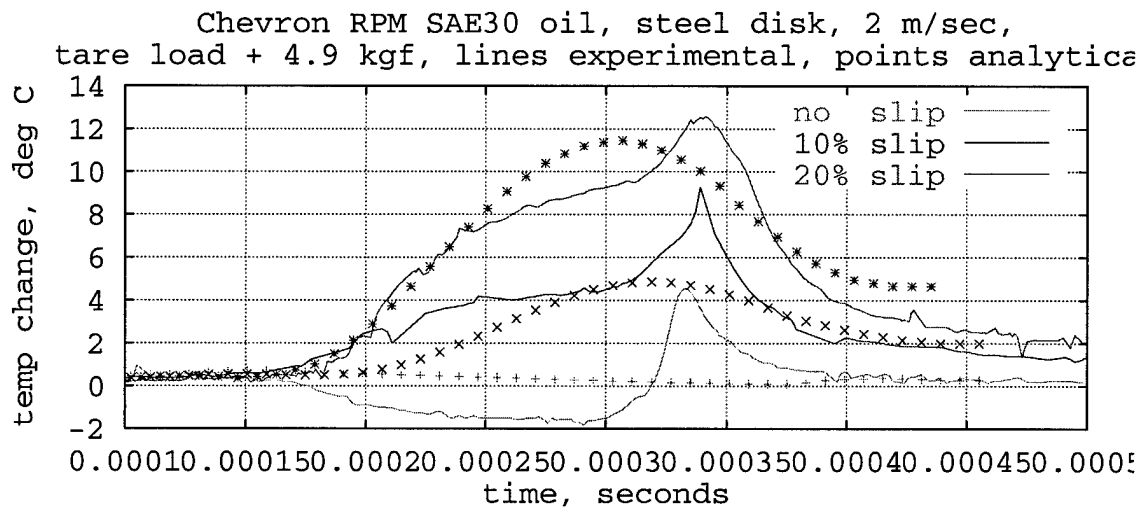
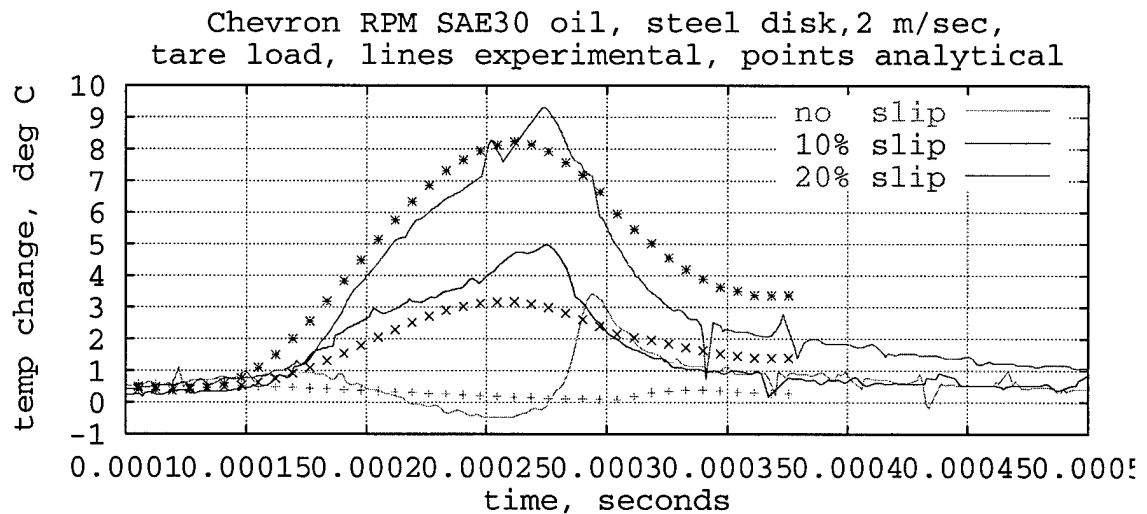


Figure 2.18: Comparison of analytical and experimental temperature transients (2 of 3).

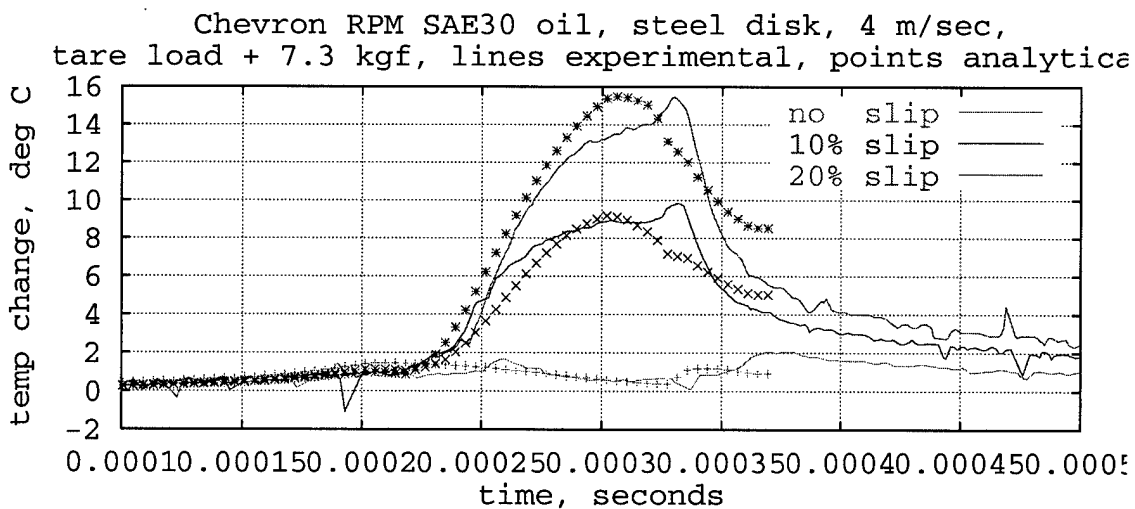
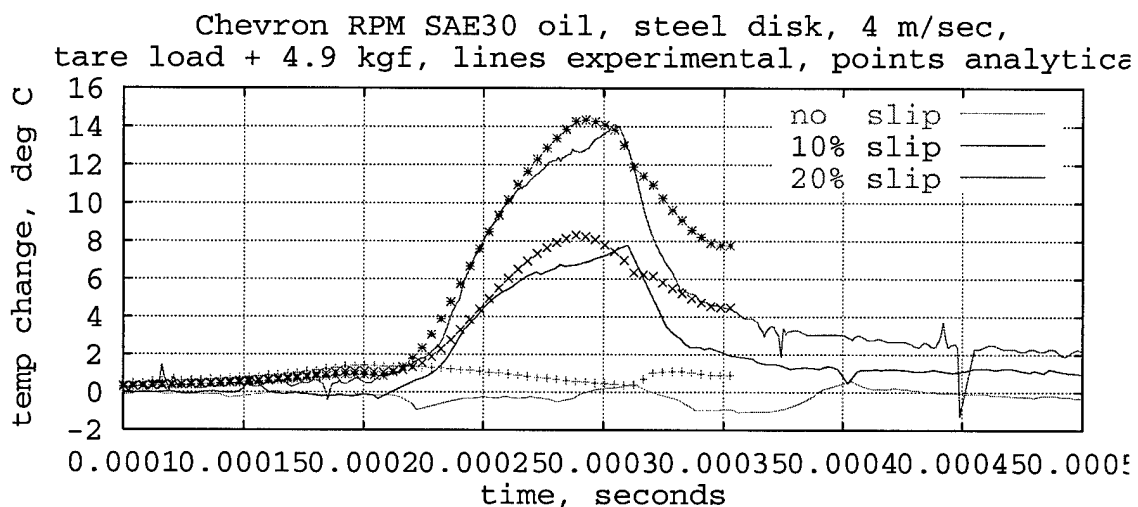
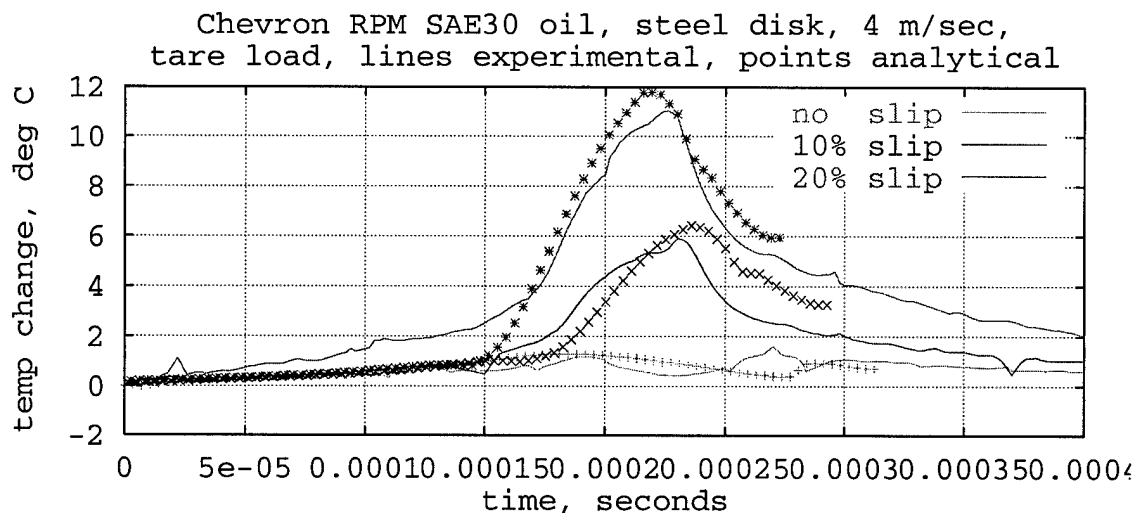


Figure 2.19: Comparison of analytical and experimental temperature transients (3 of 3).

Three lubricants are examined: NLGI (National Lubricating Grease Institute) grade 00 and 1 greases based on a mineral oil (Figure 2.21), and a thicker NLGI grade 2 grease based on a synthetic perfluoropolyalkylether (PFPAE) oil (Figure 2.22). In addition to the thicker grease (this based on thickener, rather than base oil), the PFPAE oil has a much larger pressure-viscosity coefficient than the mineral oil. The variation of viscosity with pressure roughly follows a power law, and this coefficient appears within the exponent. The larger coefficient results in a greater viscosity increase, greater compression and shear heating, and greater temperature increase during sensor passover. The difference can be observed in the pressure profiles, where the PFPAE-based grease shows the same peak truncation for no slip as the mineral oil did for much more substantial slip. The common behavior, though, indicates no thickener effect.

Sensed parameter duration and quantitative agreement between analysis and experiment are good. Cross-sensitivity in the pressure sensor is an issue, one that can probably be dealt with using the technique described in Tramposch [59]. Cross-sensitivity in the temperature sensor has been largely, though not completely, dealt with by the choice of a novel material (no other researchers use zirconium).

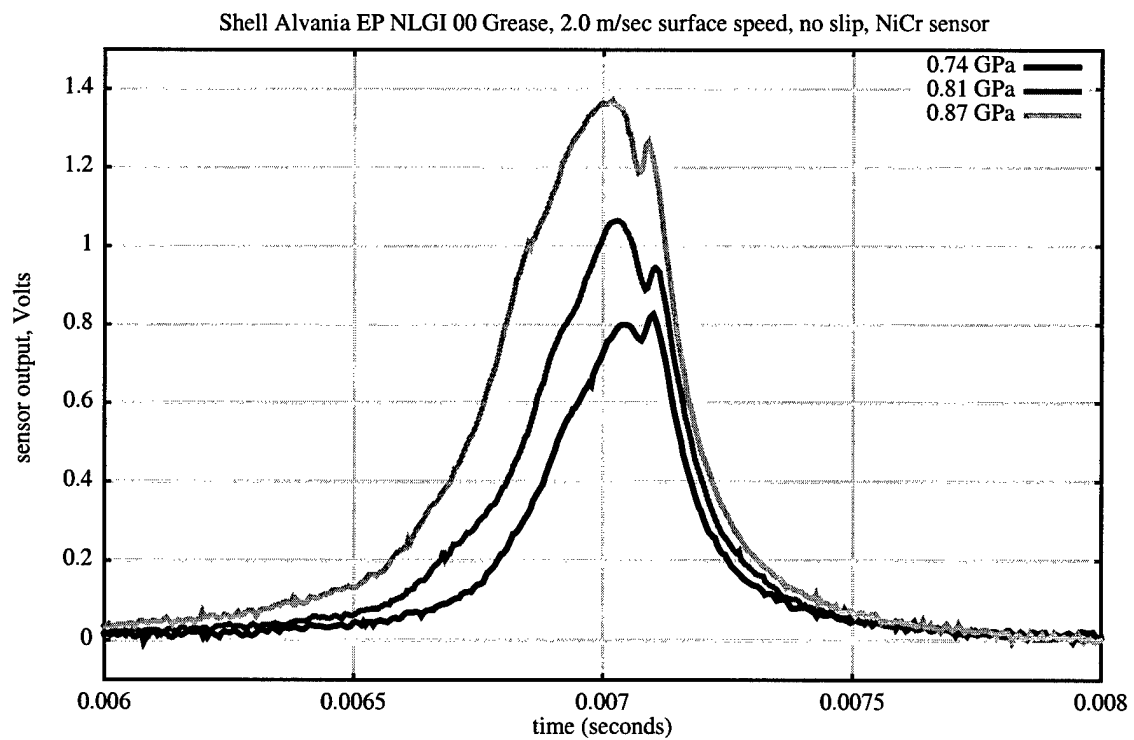
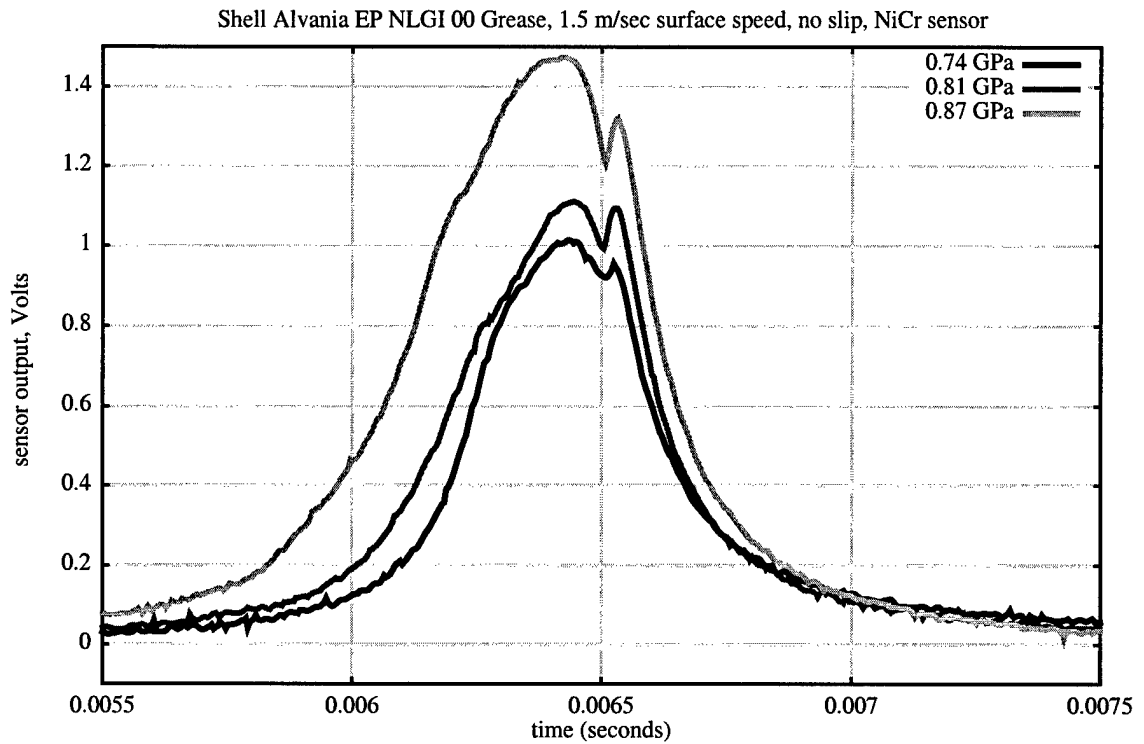


Figure 2.20: Pressure sensor output, NLGI-00 grease with mineral oil.

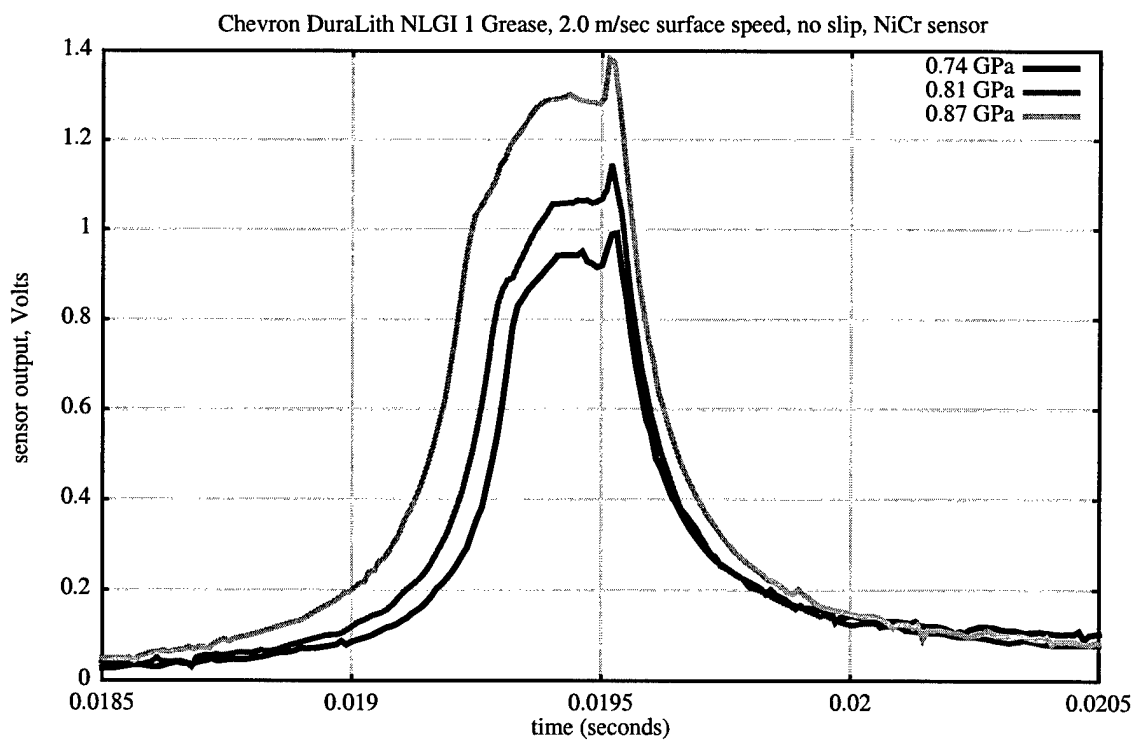
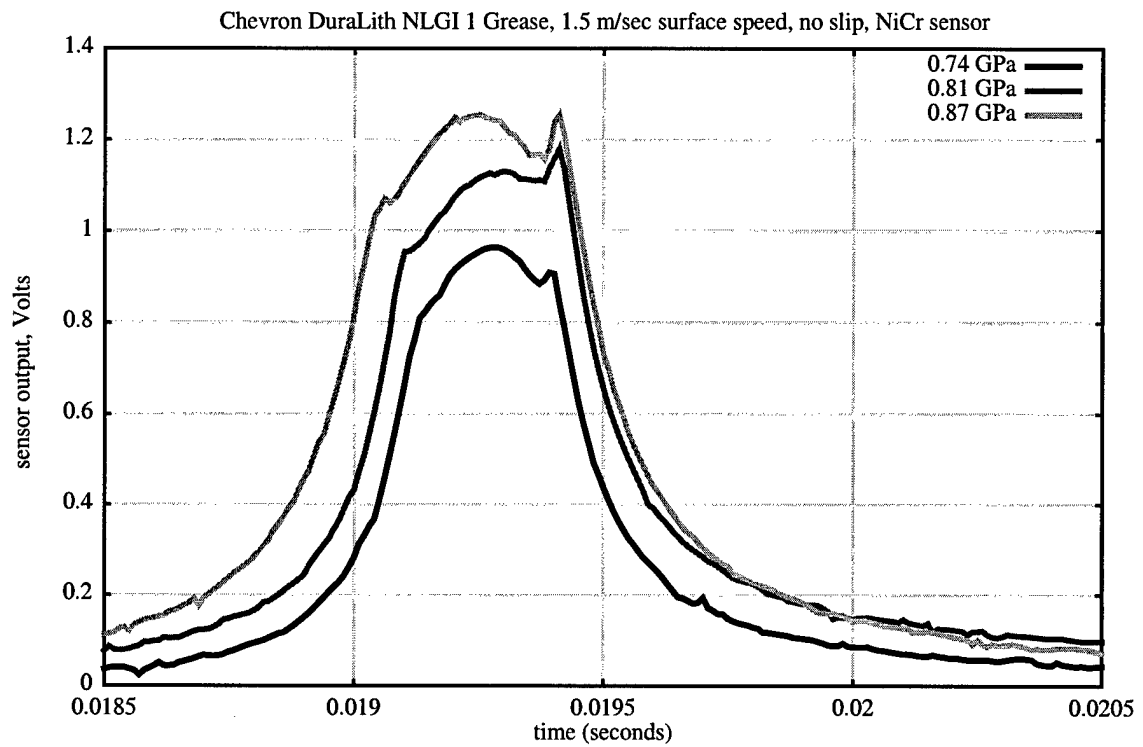


Figure 2.21: Pressure sensor output, NLGI-1 grease with mineral oil.



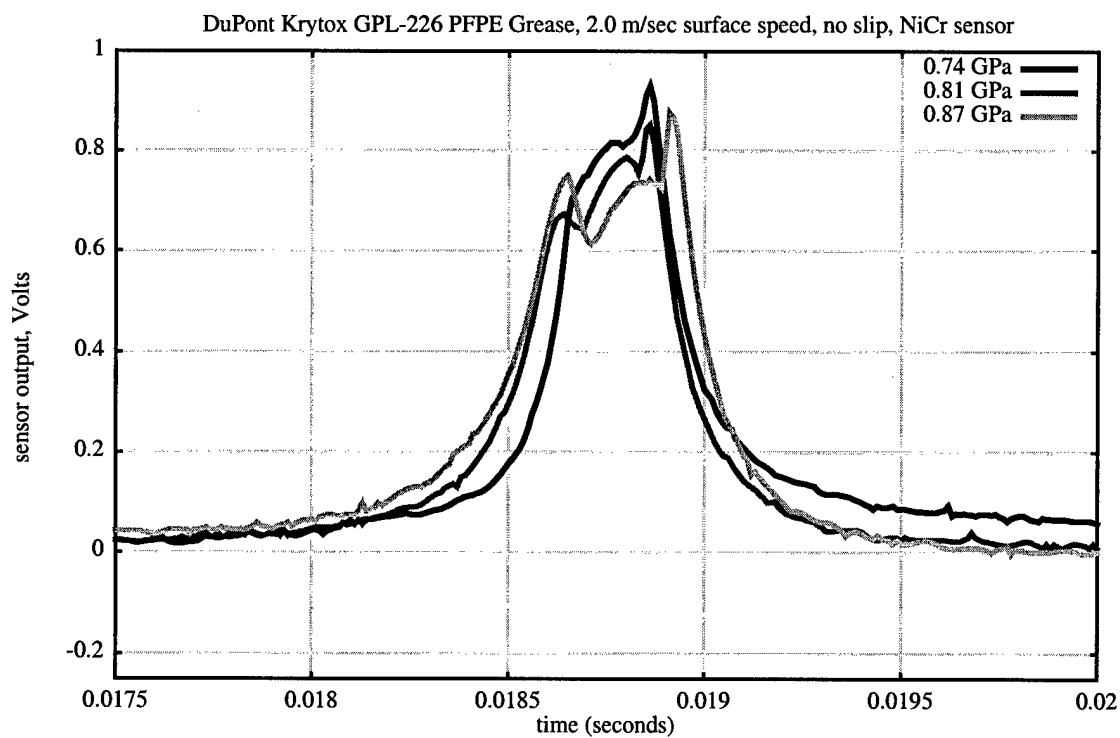
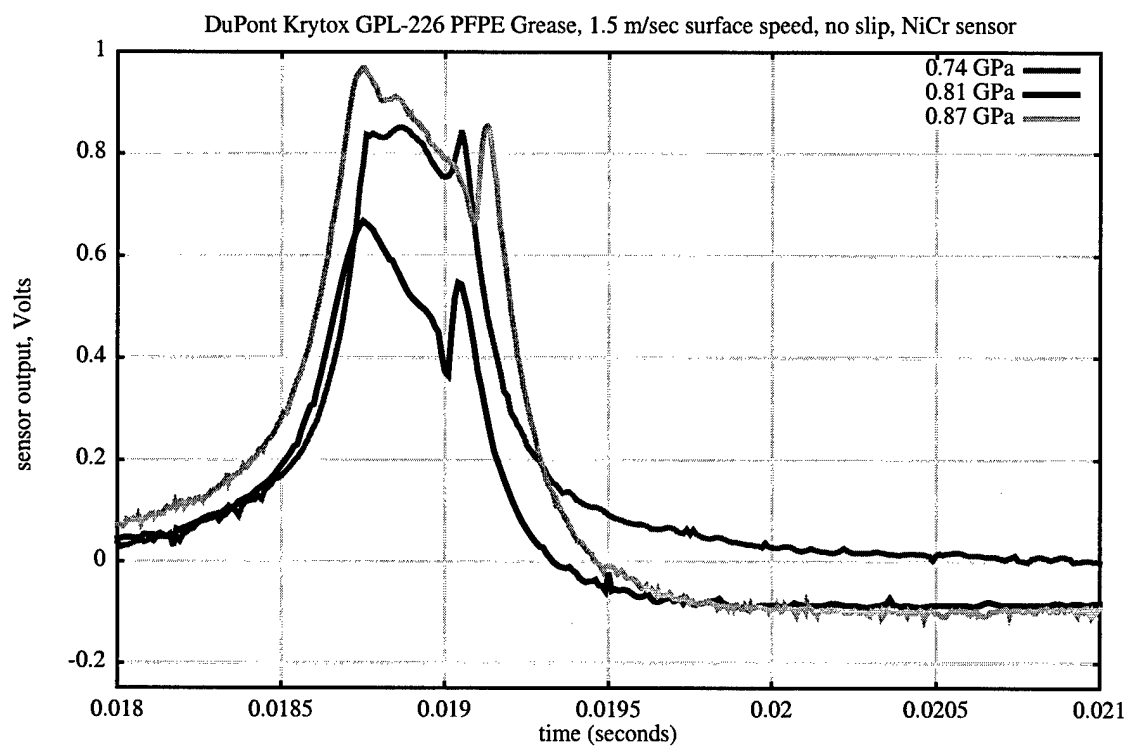


Figure 2.22: Pressure sensor output, NLGI-2 grease with PFPAE oil.

### 3. RADIO TELEMETER FOR COMPONENT TEMPERATURE ASSESSMENT.

#### 3.1 Goals to be Achieved.

In keeping with overall project goals, the goal of this phase is the development of a component-scale sensing system that provides a capability not currently commercially available. One key component parameter is temperature. Tribocomponent temperature influences contact temperature, lubricant viscosity, and lubricant degradation. Temperatures of points on stationary components are readily measured using thermocouples or thermistors. Large moving components can be monitored using existing telemeters or rotating contactors. In some cases, pyrometry is an option, although oil splash or grease can both bias and interrupt measurement. There is a significant niche in the measurement of the temperatures of small components undergoing complicated motions. Two notable examples of this might be planetary gears and bearing rollers. The smaller of these two is a bearing roller. Focussed on this device, the goal is the development of a minimally invasive telemeter for the assessment of bearing roller temperature during normal operation.

#### 3.2 Literature Review.

Most telemetry applied to machine dynamics uses relatively large commercial telemeters attached to a rotating shaft, with some sort of external sensor applied. Reference 94 describes one example. This type of device is not amenable to the environments or complicated motions of mechanisms like bearing rollers or planetary gears, whose small components have motive degrees of freedom independent of the large shaft to which the telemeter and power supply are normally attached.

Burrham et al. [93] provides one example of a telemeter applied to a tribocomponent, here a piston, with backface temperature the quantity measured. This

telemeter is as large as commercial models, but is both more robust and does not need a battery, relying instead on piston motion and a variable-inductance circuit for power.

The biological community has produced a great deal of work in the area of small telemeters. Amalaner et al. [95] and Mackay [96] are comprehensive references in biotelemetry. Authors who focussed on small telemeters include

- Naef-Denzer [97], who instrumented small birds for range determination
- Kutsch et al. [98], who developed telemeters for locust muscle activity measurement, and
- Cutchis et al. [99], who built telemeters for human ingestion.

The references from the biotelemetry community provide valuable tips for telemeter construction. A key advantage is that the authors need not be concerned about competitive advantage. A disadvantage, on the other hand, is that the data acquisition environment is much different, a point that will be expanded on in the description of design.

### 3.3 Theory of Device Operation.

Telemeters are remote information transmitters. Information is typically transmitted by the modulation (time-dependent change) of a carrier medium: for example light, sound, or an electromagnetic emission. The carrier is chosen to facilitate conveyance of the information from transmitter. Radio is a useful carrier in the tribological environment -- oil splash has little effect on transmission.

Modulation method also plays an important role in the utility of a telemeter. Digital and analog methods form the largest distinction. Digital methods feature great immunity from noise, but require greater numbers of components and more stringent power requirements. Figure 3.1 provides examples of two analog modulation methods used by nearly everyone. Analog modulation (as in AM radio) modifies the carrier wave by changing its amplitude. An extreme case of this utilized by Mackay is pulse modulation, where the carrier is turned on and off, and pulse rate conveys the information. Frequency modulation (as in FM radio) changes the frequency of the carrier wave. This method is particularly useful in proximity to inverter-driven rotating machinery, where the noise takes the form of short-duration pulses. Short noise pulses distribute their energy throughout the frequency spectrum, so a method that looks at a narrow frequency band is

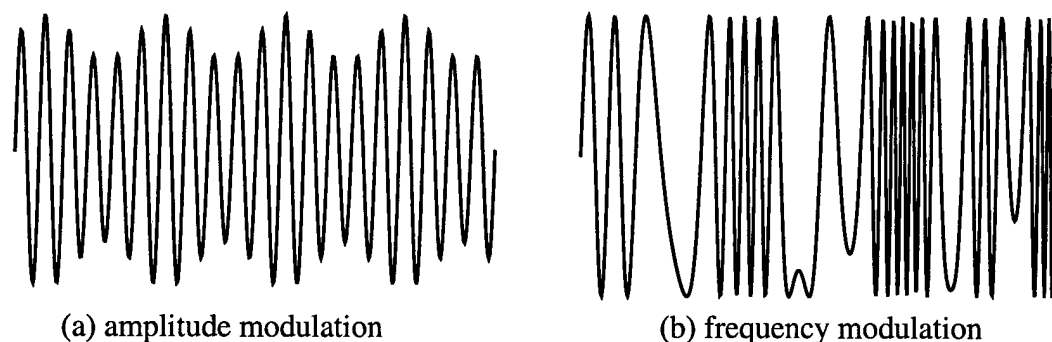


Figure 3.1: Analog modulation methods.

least affected. In contrast, the pulse-modulated telemeter produced by Mackay provides relatively efficient utilization of its battery power source, but produces a signal that looks much like the ambient noise in a rotating machine environment.

Figure 3.2 is a block diagram of the typical subsystems in any radio transmitter, one example of which is a radio telemeter (power supply omitted). Transmitters consist of an oscillator, which provides the carrier signal, a modulator, which combines the carrier with the information to transmit, an amplifier, which boosts the signal to useful levels and impedance-matches the modulator output to the input of the antenna, which efficiently radiates the encoded carrier to one or more receivers.

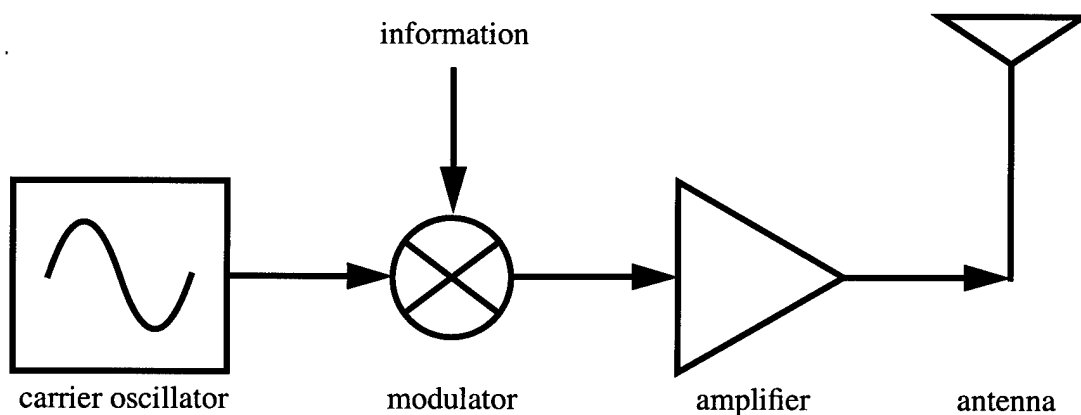


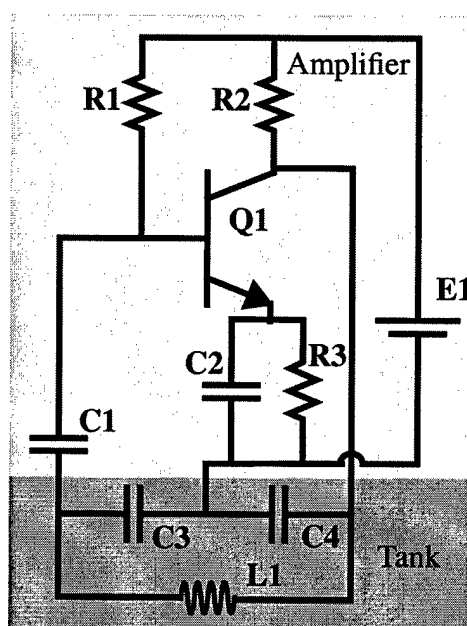
Figure 3.2: Block Diagram of a Radio Transmitter.

### 3.4 System Design Issues.

Noninvasiveness, through minimal telemeter size is a primary design goal. This is accomplished both in circuit design and manufacture. In design, size is reduced by performing multiple tasks with single circuit elements.

### 3.5 Circuit Design.

Figure 3.3 is a schematic of the circuit designed to implement the radio telemeter. Each of the tasks described above is implemented using 10 components. Subsequent sections describe how this is accomplished.



#### Parts list:

- R1 - 3900  $\Omega$ , 1/16 W base resistor,  
Panasonic ERJ3GSYJ392B
- R2 - 390  $\Omega$ , 1/16 W collector resistor,  
Panasonic ERJ3GSY391B
- R3 - 180  $\Omega$ , 1/16 W emitter resistor,  
Panasonic ERJ3GSY181B
- C1 - 0.1  $\mu$ F, 50 V, ceramic decoupling capacitor,  
Murata GRM39Y5V104Z025AD
- C2 - 0.1  $\mu$ F, 25 V, ceramic bypass capacitor,  
Murata GRM39Y5V104Z025AD
- C3,C4 - 10000 pF, 25 V tank capacitors,  
Murata GRM39Z5U103M050AD
- L1 - 3 mm diam by 3 mm high air core on 0.0055" magnet wire (30 turns, about 1  $\mu$ H)
- Q1 - Philips BFS17 low-saturation-voltage RF transistor

Figure 3.3: Radio Telemeter Circuit Schematic.

#### 3.5.1 Overall feedback circuit.

Construction of an RF (radio frequency) carrier wave is most often accomplished using a feedback oscillator. This consists of two blocks. One amplifies its input over a broad frequency range. The other is a filter, traditionally called a "tank", which modifies the phase and amplitude of its input in a frequency-dependent way. In an

ideal feedback oscillator, at one frequency, the output of the tank results in a larger, in-phase input. The gain at low amplitude must result in amplification -- this makes the circuit "self-starting" when power is first applied. Feedback continues to increase amplitude until a balance between battery power injected and resistive/radiated power lost is achieved, or until circuit nonlinearities limit the output amplitude. Many circuits of this type produce a non-sinusoidal output. This one is designed to be primarily sinusoidal to facilitate demodulation at the receiver.

There are several common types of feedback oscillators, with the type defined by the nature of components used to fabricate the filter. The type implemented in this telemeter is known as a Colpitts oscillator, with capacitors C3 and C4 and inductor L1 in Figure 3.3 forming the filter. Analysis of the Colpitts oscillator is not trivial, since in normal operation the tank circuit modifies the amplifier characteristics. Design is discussed in Parzen [101] and in Comer [102].

### 3.5.2 Amplifier components.

Design of the amplifier is dictated by power supply limitations, as described below, low supply voltage. It seems easier to find a bipolar device that can be biased into the linear range with a very low supply voltage. To best use the limited supply voltage, a transistor with a low saturation voltage was selected. Intermediate bandwidth (several Megahertz) was also necessary. One device that met these constraints well was the Philips BFS-17, with  $(V_{CE})_{sat}$  approximately 0.1V and a transition frequency of 1.3 GHz. Sufficient gain was provided using a single stage emitter-degenerated common-emitter amplifier with DC gain of approximately 2 to integrate the functions of oscillator amplifier and output amplifier -- the first example of component integration.

The purposes of components referred to in Figure 3.3 are as follows. Transistor Q1 amplifies the current applied to its base, providing a controlled energy input to the tank. Only positive collector-emitter voltages are possible, so resistor R1 is used to apply a DC current that biases the transistor to the midpoint of possible output currents (and collector-emitter voltages). Resistors R2 (at the transistor collector terminal) and R3 (at its emitter) determine the DC gain of the amplifier. R3 is chosen to overwhelm the intrinsic resistance of the emitter, which varies with temperature and would otherwise

cause the amplifier characteristics to likewise change with telemeter temperature. R2 is then chosen to provide a small amount of DC gain, here 2X input (it should be noted that this is an inverting amplifier, with the output voltage deviation -2 times the input voltage). Finally, capacitor C2 bypasses emitter resistor at high frequencies, insuring sufficient gain even when the collector resistor is partially bypassed by tank capacitor C4.

### 3.5.3 Tank circuit. Broadcast antenna. Temperature-sensing capacitors.

The Colpitts oscillator tank circuit consists of three components: a two-capacitor divider and inductor. The frequency of oscillation is

$$f = \frac{1}{2\pi\sqrt{\frac{(C_3 + C_4)}{LC_3C_4}}} \quad (3.1)$$

(component values refer to Figure 3.3). Most of the component integration described earlier is performed in this block. Briefly, the inductor functions as the transmitter antenna and the tuning capacitors frequency-modulate the carrier as temperature varies.

In more detail, inductor L is designed both to determine the frequency of oscillation and to be the broadcast antenna. As will be discussed, the thermally sensitive tank capacitors used tend to have large values, which pushes the oscillation frequency down. Because of this, the inductor value is chosen just large enough to dominate over lead inductances. Also because of this, the antenna is physically much smaller than its wavelength, which tends to mean most radiation is in the form of a spatially isotropic magnetic. The antenna is wound on a non-ferromagnetic form to avoid trapping the oscillating magnetic field, which serves as the telemeter output.

Most oscillators are designed to operate at a tightly-controlled single frequency. Variation of frequency with temperature is not acceptable. Due to this, frequency-determining elements have electrical parameters designed to vary little with temperature. This oscillator, on the contrary, must be thermally sensitive. To achieve this, the EIA (Electronic Industries Association) Type I capacitors normally used were replaced with EIA Type III bypass/decoupling capacitors. Bypass and decoupling capacitors are normally used in applications where they block DC current flow, but allow higher

frequency signals to pass through unchanged. This type of capacitor is designed to put a large capacitance into a small volume, with temperature sensitivity looked at as a secondary criterion. Thermal sensitivity is predictable and large, with typical response qualitatively shown in Figure 3.4. As the temperature of the tank capacitors increases

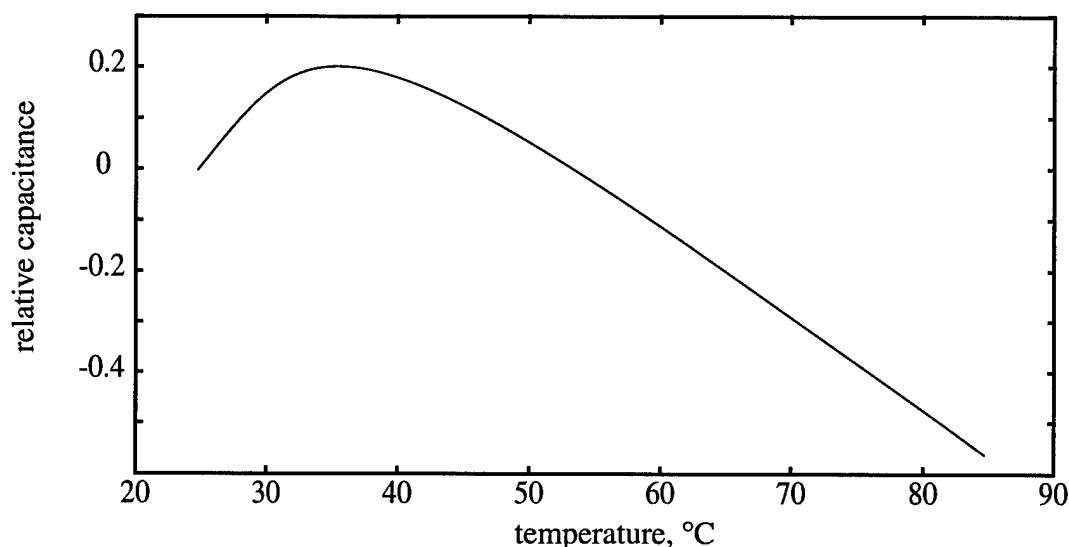


Figure 3.4: Qualitative thermal capacitance response of an EIA Type III dielectric.

from room temperature, capacitance increases, reaches a peak around 35°C, then rapidly decreases. This introduces the possibility of two capacitances (and thus frequencies) corresponding to a particular temperature. The nonuniqueness is not desirable, but not a large problem either. Industrial rotating machinery typically operates at elevated temperatures. As an indication of this, the two benchmark temperatures given to evaluate oil viscosity are 40 and 100°C.

Bypass and decoupling applications require relatively large capacitance. To maximize telemeter output, the carrier wavelength is chosen as close as possible to antenna electrical length as possible (it is invariably smaller, the wavelength of a 1.5 MHz radio wave in air is approximately 200 meters). This is done by choosing the smallest possible values for tank inductance and capacitance. The minimum commonly available capacitance is 10000 pF. With the 1  $\mu$ H tank inductor described earlier, a carrier frequency of about 1.5 MHz is obtained.



#### 3.5.4 Power source.

Telemeters can be powered by one of two methods: an internal battery or an external broadcast radio signal.

Battery power is attractive because of its simplicity, but current battery technology imposes three limitations. Even the smallest batteries available are larger than the other devices used, so the battery defines at least one dimension of the telemeter size. The chemistries of the smallest batteries also produce relatively low voltage cells, which restricts the capability of the device powered. Finally, commercially available small batteries carry a relatively small amount of energy and are unable to deliver it at high rates.

External power offers the possibility for long life and higher-powered circuits, at the price of greater circuit complexity. The large size of typical batteries means this can be achieved without making the overall telemeter larger. This work did not fit into the context of the research, but is discussed by Ko [100].

The battery employed, an Eveready 337, was the smallest found (4.8 mm diameter by 1 mm height, button cell). This battery uses a silver-oxide chemistry. The telemeter draws approximately 1 mA continuously. Under these circumstances, battery life was around one hour at room temperature, with longer life at higher temperature (note this was true whether the telemeter or only the battery was at the elevated temperature). Figure 3.5 contains three battery life curves, two at room temperature and one at 70°C. Telemeter operation ceased at a battery voltage near 1.1V. Frequency change during battery life proved not to be a problem since (1) the frequency shift associated with capacitor temperature change is much larger than that due to battery voltage change, and (2) battery decay is very rapid, particularly at high temperatures.

#### 3.6 Telemeter Manufacture.

Telemeter manufacture consists of two steps: fabrication of circuit boards and population of these boards with components. The two subsequent sections describe these steps.

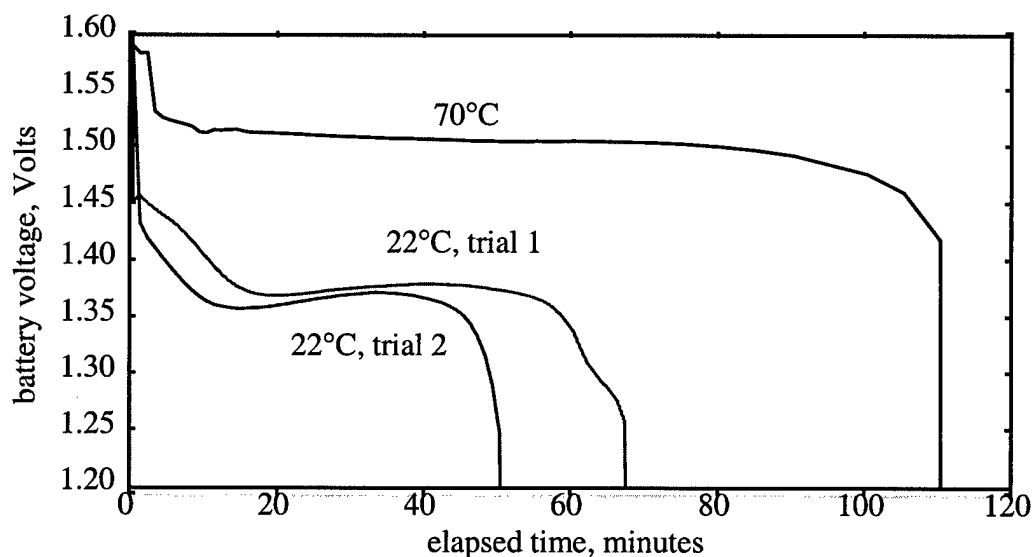


Figure 3.5: Eveready 337 battery life at room and elevated temperatures.

### 3.6.1 Circuit board manufacture.

To keep telemeter size small, small flexible circuit boards were fabricated to hold and connect the components constituting the telemeter. Traces were patterned onto the boards using a method known as photolithography. This technique is much more extensively employed in the production of thin-film sensors. More background is provided in Section 2.6.3. Only the production details (which differ significantly from those for thin film sensors) are described.

A “photomask” describing the artwork of several boards was drawn using the Postscript<sup>TM</sup> page description language. The mask, which is a photographic positive of the metal lines on the final board, was produced using an imagesetter, a high resolution printer used in the graphic arts industry. Figure 3.6 shows the artwork used to construct six circuit boards (artwork at 5X).

Pieces of R/flex 1100 flexible circuit board stock (Rogers Corporation, Microwave and Circuit Materials Division, Chandler, AZ) were cleaned with soap, water, and a scouring pad, then dip-coated with KPR-3 photoresist (London Chemical Company, Bensenville, IL). The coated boards were baked at 65°C for 10 minutes, covered with the photomask (emulsion side to the board), and exposed to the light from a 5-tube ultraviolet

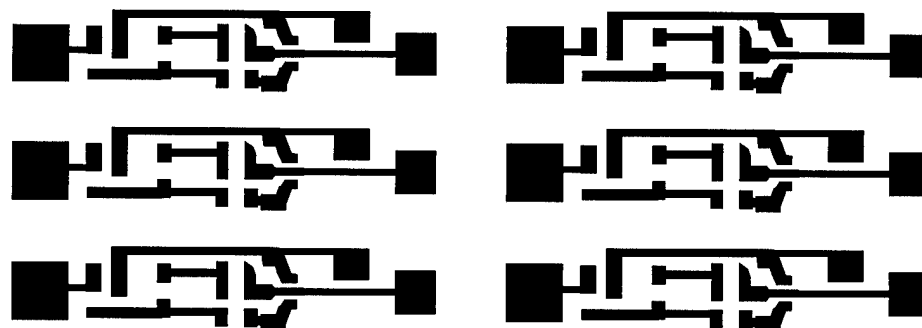


Figure 3.6: Artwork used to construct photomask for six circuit boards (5X).

lightbox (Kepro Circuit Systems, Fenton, MO) for 3.5 minutes. The exposed photoresist was removed from the board during a 90 second development cycle in trichloroethylene. A 10 minute, 120°C postbake was used to harden the remaining resist lines. The unprotected copper was removed by etching in a 70°C solution of ferric chloride and hydrochloric acid (600 gm ferric chloride to 83 ml concentrated hydrochloric acid to 1 l water), rinsed, electroless tin-plated with Kepro Tinnit solution, and rinsed again. The individual boards were then cut out and populated with components as described next.

### 3.6.2 Surface mount technology component attachment. Telemeter holder. Final testing.

All telemeter components except for the inductor employ SMT (surface-mount technology). SMT devices are small parallelepipeds, and have short leads or conductive endcaps and no leads. A typical passive component size is 1.5 by 0.75 by 1 mm high. A solder-bearing paste (Kester WS-860, Kester Solder, Des Plaines, IL) with a low melting point (210°C) is used. The paste is deposited onto the board's metallized pads, the components are temporarily placed onto the solder paste, then the paste is heated, either by putting the entire board into an oven or by local heating with the focused output of a heat gun. The antenna/inductor is soldered to pads on the circuit board.

After assembly, telemeters were tested for power-up oscillation. Component variation caused some telemeters not to start. This was remedied by moving the amplifier bias point through an increase in base resistor R1.

A brass telemeter holder, depicted in Figure 3.7, was designed to clamp the battery, position the antenna, and provide a rigid mount for the telemeter circuit. In the final step, the flexible circuit board was glued to the telemeter body, with connections to the battery case made.

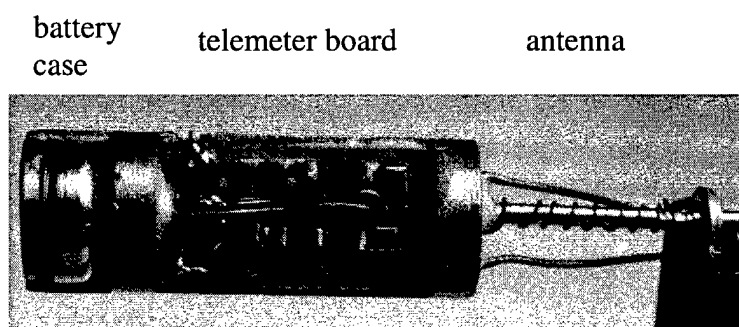


Figure 3.7: Photograph of telemeter in holder (approximately 4X).

### 3.7 Calibration and Test Procedure.

The procedures used to temperature calibrate telemeters are described here, as is the means by which in-bearing tests were run using the temperature telemeter.

#### 3.7.1 Signal monitoring.

The output frequency of the telemeter varies from 1.6 to 2.7 MHz over the rated temperature range of 20 to 85°C. This band does not correspond to allocated AM, FM, or shortwave broadcast bands. It is, however, readily measured using many shortwave radios (these low frequencies are infrequently used for communication between amateur radio operators). Early calibration and testing was done using a Sony ICF-2010 shortwave receiver in SSB (single sideband) mode, with the operator manually tracking the telemeter output with the receiver's frequency control.

Subsequent calibration and testing was performed using a Hewlett-Packard 8567A RF spectrum analyzer, which includes a frequency tracking filter. The filter was initially tuned to lock, then easily followed thermal variations in the telemeter frequency,

even in the presence of noise. Measurements were made using a receiver antenna consisting of a single loop of magnet wire approximately 150 mm in diameter, attached via 50  $\Omega$  coaxial cable to the analyzer input. Measurement signal-to-noise ratio was typically 30 dB. At this short range, tilt in the receiver antenna resulted in amplitude modulation of the received signal. This did not impede frequency measurement.

### 3.7.2 Calibration.

Static calibration was performed by immersing the telemeter in an oil bath. A hot plate was used to gradually increase the temperature (rate of temperature increase approximately 1  $^{\circ}\text{C}/\text{min}$ ). An RF spectrum analyzer with a loop antenna was used to pick up the telemeter output. An external battery was used to separate voltage variation effects from thermal effects on the telemeter circuit (this was later tested separately - voltage changes over a range from 1.55V (new battery) to 1.10V (telemeter shutdown) resulted in frequency change corresponding to an ambient temperature error of 0.6  $^{\circ}\text{C}$ ). The results of two calibration runs performed one day apart are depicted in Figure 3.8. The results indicate good repeatability. The calibration curves exhibited a local minimum in frequency near 35 $^{\circ}\text{C}$ , corresponding to the maximum capacitance shown in Figure 3.4. A hysteretic effect was also noted, with the capacitance on temperature decreasing returning to the curve for temperature increasing only after several hours. The hysteresis is of concern, but two facts to keep in mind is that the temperature deviation is small in the 40+ $^{\circ}\text{C}$  temperature range of interest and that measurements are only performed with ascending temperature.

The lower branch of the curve in Figure 3.8 corresponds to the increasing temperature phase of operation in which testing was conducted. The following curve fit to the mean of the calibration sets, plotted in Figure 3.8, was obtained

$$T = 33.844 \pm \left( \frac{|f - 1.70463|}{0.00125428} \right)^{0.603202}, \quad (3.2)$$

where T is the temperature in degrees Centigrade and f is the telemeter output frequency in megahertz.

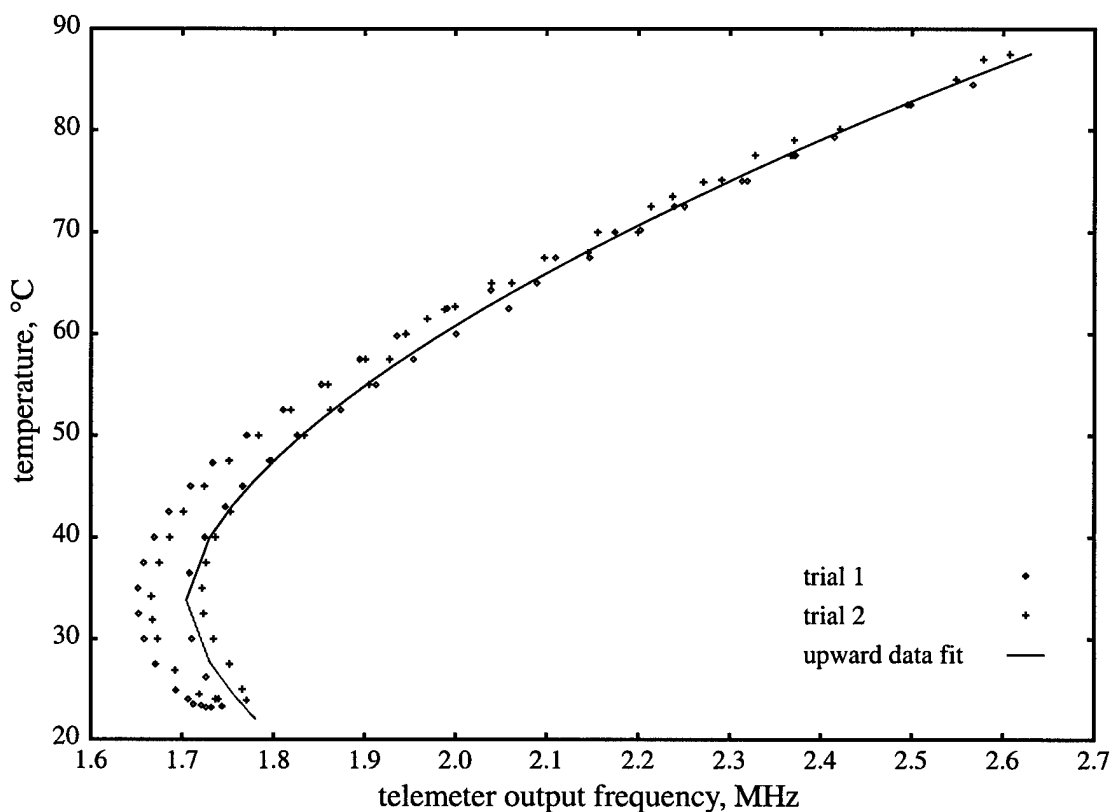


Figure 3.8: Two telemetry temperature calibration curves.

### 3.7.3 Use in axial bearing test rig.

The telemetry was tested in a new Timken JM205149/JM205110 tapered roller bearing with internal and external diameters of 50 and 90 mm. A pocket was created in the center of the large end of one roller using electrical discharge machining (EDM). The telemetry holder was then placed in the pocket, using high thermal conductivity paste to fill the approximately 50  $\mu\text{m}$  diametral gap. The telemetry and roller were placed in a cage with one pocket modified to permit easy insertion and removal of the battery-powered telemetry and to accommodate the transmission antenna. Testing was performed with six of eighteen rollers inserted to increase contact stress per unit axial load.

Three oil jets, two to the small end of the bearing and one to the rib-roller contact, were driven by an air-over-oil lubricator. Room temperature SAE 30 weight motor oil was introduced to the bearing at a flow rate of 150 cc/minute. Tests were

conducted for 10-15 minutes, with roller temperature measured using the telemeter, and housing temperature with a thermocouple attached to the cup.

### 3.8 Test Results, Discussion of Results.

A number of tests were conducted at different loads and speeds. Figures 3.9 and 3.10 depict bearing transient time response under two different peak cone Hertz stress levels and at three speeds. Data were collected during the 15 minute interval allowed by lubrication system capacity, or until the indicated telemeter temperature reached its 85°C design limit.

The measured results take place in three different heat transfer regimes. For small power input (Figure 3.9 c, 51W input thermal power), the change in temperature is negligible. At the other extreme, Figure 3.10 a (532 W input thermal power) exhibits thermal runaway, in which the cooling capacity of the bearing tester core is insufficient to keep the telemeter in its design temperature range. The other curves occupy an intermediate power regime in which heating is measurable, but controlled. In all lubricated cases, roller temperature tracks with housing temperature, with the deviation increasing with increasing power input. This contrasts with the case of lubricant loss, described in the next paragraph. The indicated roller temperature is higher than that of the housing with three exceptions: the initial temperatures in Figure 3.9a and Figure 3.10b. In these cases, indicated roller temperature jumped from below housing to above it. These are examples of the nonuniqueness in the calibration curve below 35°C. A computer program was used to translate output frequency to indicated temperature. The program was not given any insight into which branch of the calibration curve to follow.

One test (Figure 3.9 c) was inadvertently continued after loss of oil. A rapid increase in roller temperature was expected. What was not expected at the time was a decrease, then slow increase, in housing thermocouple temperature. The test was repeated under more controlled circumstances, with the results shown in Figure 3.11. After the loss of lubricant, great heating occurs at the sliding rib-roller contact. This heating is caused by the increase in friction coefficient associated with the loss of the separating fluid film. The experiment underlines the importance of oil not only as a fluid film that separates components, but also as a heat transfer agent. When lubrication was ceased, the

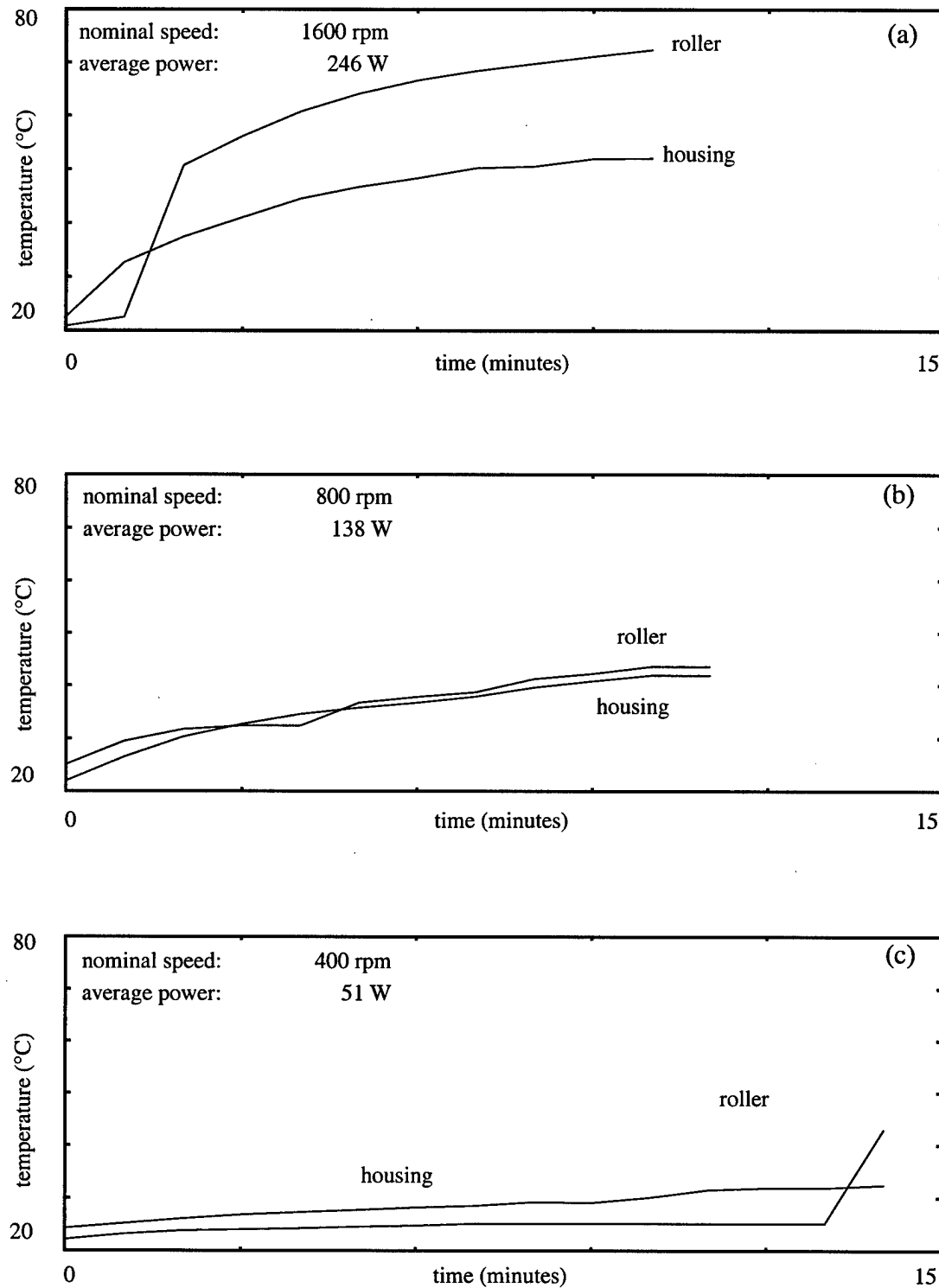


Figure 3.9: Measured roller (via telemeter) and housing (via attached thermocouple) temperatures of a tapered roller bearing with a nominal Hertzian stress level of 175 ksi and shaft speeds of (a) 400, (b) 800, and (c) 1600 rpm.



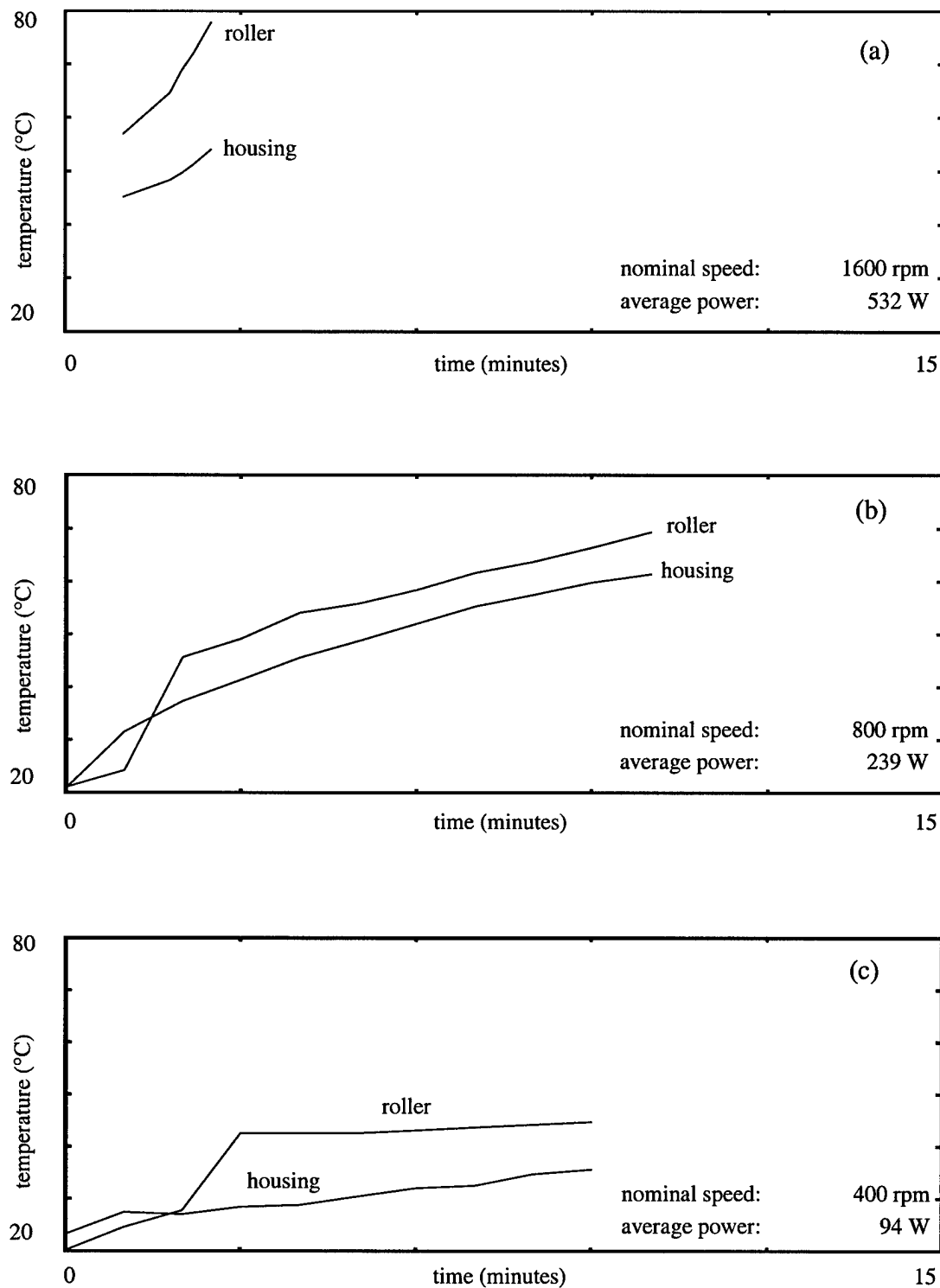


Figure 3.10: Measured roller (via telemeter) and housing (via attached thermocouple) temperatures of a tapered roller bearing with a nominal Hertzian stress level of 250 ksi and shaft speeds of (a) 400, (b) 800, and (c) 1600 rpm.

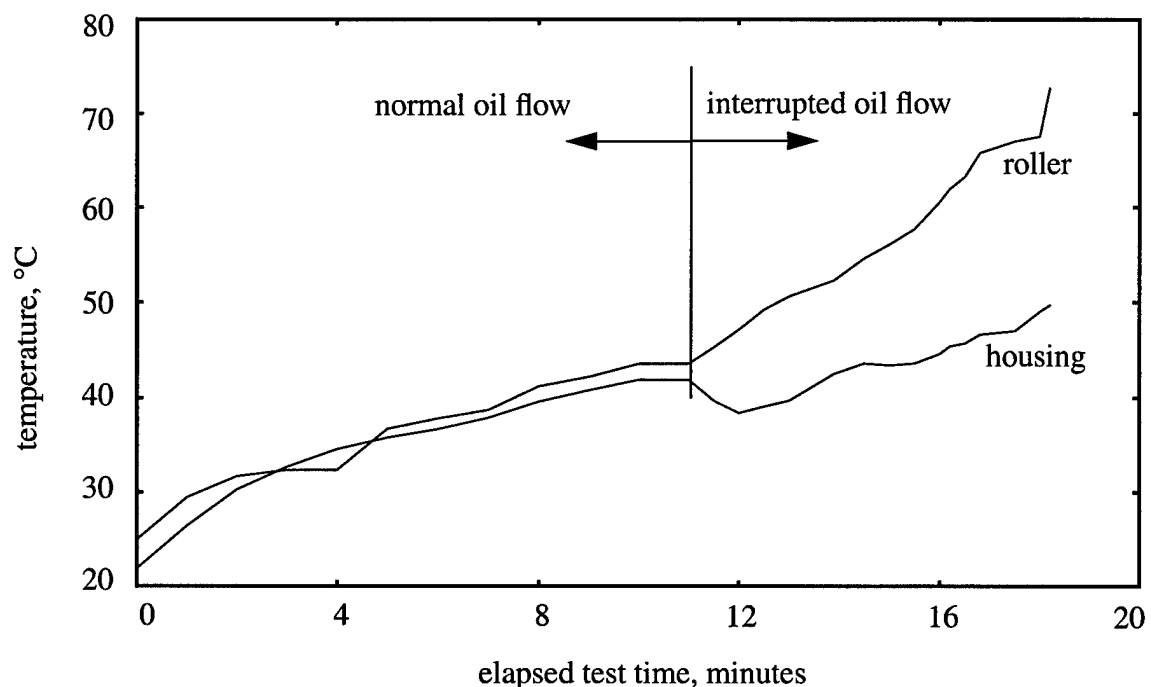


Figure 3.11: Bearing roller and housing temperatures before and after oil flow interruption (operating conditions: 175 ksi nominal, 800 rpm).

housing was no longer convectively coupled to the rollers. This indicates another potential role for an inexpensive temperature telemeter, that of a condition monitoring apparatus. The heating that occurs due to loss of lubricant is rapid, and potentially destructive not only to the bearing, but also to the system it supports. A roller-mounted temperature measurement device gives much earlier warning, time that can be used to take protective or remedial action.

#### 4. VAPOR PRESSURE LITERATURE SEARCH

One criterion that can be used to compare diagnostic or condition monitoring sensors is proximity. Sensors close to the phenomena measured have the advantages of rapid response and a relatively direct link between desired measurand and sensor output. This link minimizes the amount of guesswork needed to assign a sensor signal to a specific change in system status. Remote sensors, on the other hand, can monitor several systems simultaneously and can often be placed in a more benign environment. The thin-film sensors described in the previous chapter provide an extreme example of directness, which comes at the potential price of mechanical, thermal, and chemical invasiveness. The other type of sensor described in the request for proposal and elaborated on during an early teleconference after acceptance of the Phase I proposal falls at the other end of the spectrum. As described in the proposal, this sensor measures lubricant vapor pressure. Discussion during the May 14, 1998 teleconference provided more detail concerning the desired function of the remote sensor. This device is to rely on diffusive or convective transfer of the lubricant or its degradation products to indirectly indicate the condition of nearby lubricated contacts. This clarification expanded the mandate for the literature search somewhat and focused it on an application. The remainder of this chapter describes the results of the search.

Vapor pressure is one indication of changes in the status of a lubricant. In petroleum derivatives, it is used, for example, as an indication of molecular weight. The most common method of measuring vapor pressure is direct. For volatile liquids like fuels, a chamber with attached pressure gauge [104] or modified manometer called an isoteniscope is used [103]. As vapor pressure decreases, the traditional Bourdon gauge is replaced with a vacuum gauge (capacitance manometer, thermoresistive, or ionization gauge) [105]. Even in the low pressure work, of Sasse et al. [105] "low" pressures are on the order of  $10^{-3}$  Torr, although this seems more an apparatus limitation than a fundamental problem. Two greater problems introduced by the authors are the inability to

separate the phenomena of gas generation, leakage or permeability, and adsorption or desorption.

Lubricants consist of a base oil and often, a system of additives that, among other things, inhibit oxidation, prevent foaming, and separate component surfaces during film collapse. Under some situations, a second type of vapor pressure sensor could be used. The vapor pressure of a liquid varies with the concentrations of solutes in it. Variation of vapor pressure with other parameters like temperature fixed can thus be used to monitor changes in additive concentration. This measurement, called vapor pressure (VPO), is described in references 106 (description of a standard test procedure) and 107 (application of the method to a biological problem). The difficulty in using VPO alone as a condition monitoring technique is the inability to separate concentration-based vapor pressure changes from changes in component temperature. The required proximate sensor deprives this method of its principal advantage.

Attitude control wheels typically operate in a sealed environment under a partial vacuum, sometimes with an inert back-filled gas. The purpose of this vacuum is reduction of drag and prevention of component oxidation. The vacuum environment is home to two other devices used to assess the quantity and composition of substances in the low-pressure atmosphere.

The first of these, the quartz crystal microbalance (QCM), measures small changes in the fundamental natural frequency of a piezoelectric disk. Mass loading, due to material condensation onto the disk or, to a lesser extent, due to ambient gas pressure, reduces this natural frequency. The sensitivity of the measurement can be very large, with resolution on the order of an atomic monolayer and a range up to microns (tens of thousands of monolayers). Gregory and Levenson [108] describe indirect vapor pressure measurement by determination of mass flux for molten lead over a temperature range that results in pressures of  $10^{-6}$  to  $10^{-4}$  Torr. In Reference 7, Wallace applies the QCM to a problem more related to the aerospace industry: assessment of outgassing and surface contamination of a sealant. This paper also describes a means of compensating for thermal drift by use of a second, thermally coupled QCM physically isolated from the contaminant mass flux. Scialdone et al. [109] reports on the recent use of a QCM to assess the vapor pressures of two potential ACW lubricants, Apiezon ® C (hydrocarbon-based) and Krytox AB ® (a perfluoropolyalkylether).

One disadvantage of direct pressure sensors is a lack of chemical specificity. Direct pressure sensors can not differentiate between the pressure due to lubricant breakdown, residual vacuum, and component outgassing. QCMs measure the mass of material condensing onto them, which depends on a "sticking potential", the likelihood of condensation without reevaporation. This provides a degree of sorting useful in separating volatile (low sticking potential) from volatilized (high sticking potential) materials. They are therefore useful in measurement of oil migration. Another tool, though, might be more useful for measurement of the low molecular weight fractions associated with lubricant breakdown.

The second device commonly used in vacuum physics and technology is the residual gas analyzer (RGA). RGAs characterize the composition of the substances contaminating a vacuum. This is done with a small mass spectrometer which ionizes particles, accelerates them in a magnetic field, and sorts them by mass. RGA's have long been used to diagnose the partial pressure and degree of degradation of vacuum pump oils, which are chemically similar to the lubricants used in ACWs. These exhibit characteristic cracking spectra, distributions of pressure with molecular weight (expressed in terms of AMU's, or "atomic mass units"). Reference 5 describes the cracking spectra of hydrocarbon and fluorocarbon oils, as well as the gases and solvents commonly contaminating evacuated vessels. Traditional RGA units were relatively large, fragile, and expensive. They required the use of an external vacuum pump. The more recent invention is the "process RGA" which dramatically reduces cost, space and fragility. Figure 4.12 depicts a process RGA head at approximately twice its true size [4]. The head can operate in pressures from ultrahigh vacuum to 10 mTorr ( $10^{-5}$  atmospheres) and has a partial pressure resolution of approximately  $10^{-9}$  Torr ( $10^{-12}$  atmospheres). This pressure range can be extended to atmosphere by sampling the ACW atmosphere through a leak valve to the external space vacuum.

The principal failure modes of ACWs are correlated with changes in the lubricating system: either the reservoir of lubricant is depleted, or the chemical composition of the lubricant changes. Direct pressure sensors or QCMs can monitor for the loss of volatilized lubricant, but indicate compositional change only through a change in QCM sticking coefficient. The latter phenomenon is more easily measured using and RGA, assuming degradation changes the relative pressures within the lubricant cracking spectrum.

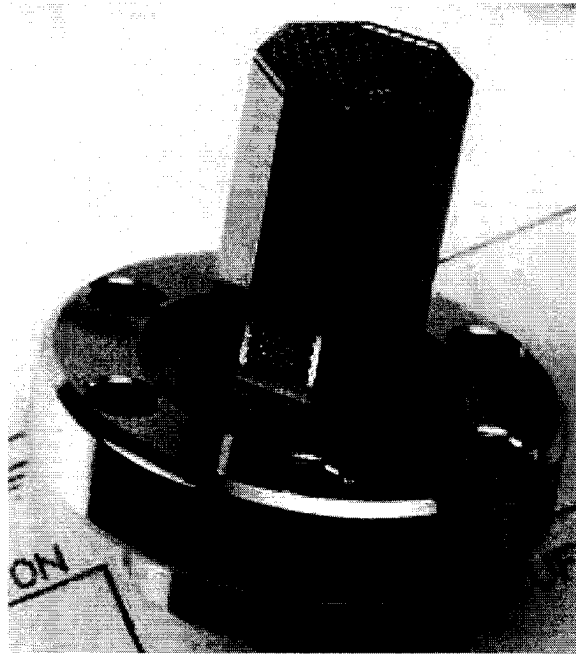


Figure 4.12: Photograph of process RGA head (~ 2X scale).

## 5. PHASE I CONCLUSIONS

In-situ thin-film sensors have been developed for the measurement of the pressure and temperature transients. Materials and processes have been designed for the deposition of durable thin films, both electrical insulators and resistive sensing layers. Three technologies: through-mask deposition, photolithography, and laser patterning have been evaluated for patterning of the sensing layers. Sensors thus fabricated have been produced on glass and steel substrates and tested with oils and greases, using both hydrocarbon and fluorocarbon-based base oils. A small, simple signal conditioner has been designed and tested. The resulting sensors have proven durable, repeatable, and have been correlated with analytical results.

A literature search of technologies for remote assessment of lubricated contact condition was made, with the emphasis on sampling of physical and chemical remnants lubricants and their degradation products. Two different methods of vapor pressure sensors: direct pressure sensors and vapor pressure osmometers were evaluated. Two other means of measuring lubricant volatiles: the quartz crystal microbalance and the residual gas analyzer (RGA), were shown to be more appropriate in the case of low vapor pressure lubricants (typical in the case of ACW bearings). Of the two, a process RGA is believed the better choice because of the enhanced information given by the lubricant's chemical breakdown spectrum.

## 6. PHASE II THRUSTS

The major thrusts for the Phase II effort have been designated in light of Phase I research and in consideration of priorities expressed by Air Force personnel in contacts since the inception of the Phase I contract. They consist of four programs. The first is the adaptation of the thin-film sensors described in this report to the nonplanar geometry of a bearing ring and use of this type of sensor. The second is the evaluation of a retainer-mounted telemeter as a noninvasive tool for prediction of loss of lubricant. Third is preliminary evaluation of two comparative near-contact sensors as possible predictors of incipient failure. The final thrust is the examination of the two most promising methods of remote convective/diffusive sensors identified in the Phase I literature review.



## 7. REFERENCES

- [1] Anonymous, MIL-A-83577B 1 Feb. 1988 Assemblies, Moving Mechanical Parts, for Space and Launch Vehicles, General Specification for
- [2] W. Auer, "Test Results and Flight Experience of Ball Bearing Momentum and Reaction Wheels," NASA CP3062, 24th Aerospace Mechanism Symposium
- [3] B. Bialke, "On-Orbit Problems with Scanning Earth Sensor Bearing Lubrication: A Testimonial for Realistic Life Testing of Long Life Space Flight Mechanisms," pp 349-357 of Guidance and Control 1994, Volume 86 of Advances in the Astronautical Sciences, R.D. Culp and R.D. Rausch, Editors, Univelt, 1994.
- [4] Ferran Scientific Micropole RGA Product Literature, Ferran Scientific, San Diego, CA 92121.
- [5] "Cracking Patterns", Appendix E of J.F. O'Hanlon, A User's Guide to Vacuum Technology, Second Edition, Wiley-Interscience, 1989.
- [6] P.D. Fleischauer, M.R. Hilton, R.A. Rowntree, M.J. Todd, "Assessment of State-of-the-Art and Tribology of Advanced Spacecraft Mechanisms," as described on pages 327-330 of NASA TM 107047, "Space Mechanisms Lessons Learned Study," W. Shapiro, F. Murray, R. Howarth and R. Fusaro, National Aeronautics and Space Administration.
- [7] D.A. Wallace, "Use of the Quartz Crystal Microbalance for Outgassing and Optical Contamination Measurements," Journal of Vacuum Science and Technology, Volume 9, Number 1, pp 462-466, 1972.
- [8] Crook, A.W., "Elastohydrodynamic Lubrication of Rollers," Nature, Volume 190, Number 4782, pp 1182-1183, June 1961.
- [9] F.J. Wren, C.A. Moyer, "Understanding Friction and E.H.L. Films in Concentrated Contacts of a Tapered Roller Bearing", Article C10/72 in Elastohydrodynamic Lubrication - 1972 Symposium, Institution of Mechanical Engineers, pp 55-60. 1972.
- [10] K.L. Johnson, Contact Mechanics, Cambridge Press, 1985.

- [11] A. Palmgren, Ball and Roller Bearing Engineering, S.H. Burbank, 1959.
- [12] L.I. Maissel and R. Glang, Handbook of Thin Film Technology, pp 3-24 to 3-25, McGraw-Hill, 1970.
- [13] R.W. Berry, P.M. Hall, M.T.Harris, Thin Film Technology, p 209, Van Nostrand, 1968.
- [14] D.M. Mattox, Growth and Growth-Related Properties of Films Formed by Physical Vapor Deposition, pages 538-555 in Surface Engineering, Volume 5 of the ASM Metals Handbook, American Society of Materials, 1990.
- [15] S.J. Bull, "Techniques for improving thin film adhesion," Vacuum, Volume 43, Numbers 5-7, pp 517-520, 1992.
- [16] J.L. Vossen & J.J. Cuomo, "Glow Discharge Sputter Deposition," in Thin Film Processes, J.L. Vossen and W. Kern, Editors, Academic Press, 1978.
- [17] R. Parsons, "Sputter Deposition Processes," in Thin Film Processes II, J.L. Vossen and W. Kern, Editors, Academic Press, 1991.
- [18] L.I. Maissel and R. Glang, Handbook of Thin Film Technology, pp 3-24 to 3-25, McGraw-Hill, 1970.
- [19] British Department of Trade and Industry, "Wear Resistant Surfaces in Engineering: a guide to their production, properties and selection," Her Majesty's Stationary Office, 1986.
- [20] B. Chapman, Glow Discharge Processes: Sputtering and Plasma Etching, John Wiley & Sons, 1980.
- [21] J.F. O'Hanlon, A User's Guide to Vacuum Technology, Second Edition, Wiley-Interscience, 1989.
- [22] F.K. Orcutt, "Experimental Study of Elastohydrodynamic Lubrication," ASLE Transactions, Vol 8, pp 381-396, 1965.
- [23] J.W. Kannel, "Measurements of Pressures in Rolling Contact," Proc. Inst. Mech. Engrs., Vol 180, Ser 3B, pp 135-142, 1965-66.
- [24] J.W. Kannel, J.C. Bell, C.M. Allen, "Methods for Determining Pressure Distributions in Lubricated Rolling Contact," "ASLE Transactions, Volume 8, pp 250-270, 1965.

- [25] J.W. Kannel, T.A. Dow, "The Evolution of Surface Pressure and Temperature Measurement Techniques for Use in the Study of Lubrication in Metal Rolling," Trans. ASME Journal of Lubrication Technology, pp 611-616, October 1974.
- [26] J.W. Kannel, F.F. Zugaro, T.A. Dow, "A Method for Measuring Surface Temperature Between Rolling/Sliding Steel Cylinders," Trans. ASME J. Lubr. Technology, Volume 100, pp 110-114 January 1978.
- [27] J.W. Kannel and T.A. Dow, "The Relation Between Pressure and Temperature in Rolling-Sliding EHD Contact," ASLE Transactions, Volume 23, Number 3, pp 262-268, 1980.
- [28] T.L. Merriman, J.W. Kannel, "Apparatus for Extensional Viscosity Measurements," Journal of Tribology, Transactions of the ASME, Volume 119, Number 4, pp 700-703, October 1997.
- [29] G.M. Hamilton, S.L. Moore, "Deformation and pressure in an elastohydrodynamic contact", Proc. Royal Soc. London Ser A, Vol 322, pp 313-330, 1971.
- [30] M.O.A. Mokhtar, A.A. Abdel Ghany, "Elastohydrodynamic Behavior of Rolling Elliptical Contacts: Part I: Pressure and Temperature Distribution," Transactions of the ASME: Journal of Tribology, Volume 107, pp 343-351, July 1985.
- [31] M.O.A. Mokhtar, A.A. Abdel Ghany, "Elastohydrodynamic Behavior of Rolling Elliptical Contacts: Part II: Oil Film Thickness and Contact Profile," Transactions of the ASME: Journal of Tribology, Volume 107, pp 352-358, July 1985.
- [32] M.O.A. Mokhtar, A.A. Abdel Ghany, "Elastohydrodynamic Behavior of Elliptical Contacts Under Pure Rolling Conditions," Transactions of the ASME: Journal of Tribology, Volume 109, pp 659-663, October 1987.
- [33] M.M.A. Safa, J.A. Leather, J.C. Anderson, "Thin Film Microtransducers for Elastohydrodynamic Lubrication Studies," Thin Solid Films, Vol 64, pp 257-262, 1979.
- [34] G.M.S. De Silva, J.A. Leather, J.C. Anderson, "The Fabrication of Foil Masks Using Laser Cutting," Thin Solid Films, Vol 77, pp 341-346, 1981.
- [35] M.M.A. Safa, J.C. Anderson, J.A. Leather, "Transducers for Pressure, Temperature, and Oil Film Thickness Measurement in Bearings," Sensors and Actuators, Volume 3, pp 119-128, 1982/83.
- [36] M.M.A. Safa, R. Cohar, "Squeeze films in elastohydrodynamic lubrication," Mechanisms and Surface Distress: Proceedings of the 12th Leeds-Lyon Symposium on Tribology, Elsevier, 1987.

- [37] W.J. Bartz, J. Ehlert, "Influence of Pressure Viscosity of Lubrication Oils on Pressure, Temperature, and Film Thickness in Elastohydrodynamic Rolling Contacts," Trans. ASME Journal of Lubrication Technology, Vol 98, pp 500-508, October 1976.
- [38] H. Peeken, A. Köhler, "Moderne Messtechnik mittels aufgedampfter Geber in Gleit- und Wälzlager," Konstruktion, Volume 32, Number 6, pp 241-246, 1980.
- [39] H. Peeken, A. Köhler, "Messtechnische Ergebnisse zum EHD-Kontakt am Zwei-Scheiben-Prüfstand," Konstruktion, Volume 33, Number 5, pages 175-182, 1981.
- [40] H. Peeken, M. Spilker, "Hochdruckkammer für Drücke bis 20000 bar," Konstruktion, Volume 17, pp 97-100, May 1980.
- [41] M.E. Königer, G. Reithmeier, M. Simon, "Ion Beam Sputter Deposition of Thin Insulating Layers for Applications in Highly Loaded Contacts," Thin Solid Films, Volume 109, pp 19-25, 1983.
- [42] E. Kagerer, M.E. Königer, "Ion Beam Sputter Deposition of Thin-Film Sensors for Applications in Highly Loaded Contacts," Thin Solid Films, Volume 192, pp 333-344, 1989.
- [43] K.J. Janczak, S. Hofman, "Investigation of the Temperature Distribution in the Elastohydrodynamic Oil Film," Wear, Volume 94, pp 241-257, 1984.
- [44] S. Hofman, K. Janczak, A. Wilczek, "Evaluation of Errors of Temperature Measurements with the Aid of a Thin-Layer Transducer in Concentrated Contacts," Wear, Volume 102, pp 271-293, 1985.
- [45] H. van Leeuwen, H. Meijer, M. Schouten, "Elastohydrodynamic film thickness and temperature measurements in dynamically loaded concentrated contacts: eccentric cam-flat follower," Paper XX(ii) in Fluid Film Lubrication, Osborne Reynolds Centenary, Proceedings of the 11th Leeds-Lyon Symposium, pp 611-625, 1986.
- [46] M.J.W. Schouten, H.J. van Leeuwen, H.A. Meijer, "The Lubrication of Dynamically Loaded Concentrated Hard Line Contacts: Temperature and Pressure Measurements," AGARD-CP-394 (Advisory Group for Aerospace Research and Development Conference Proceedings 394), Aircraft Gear and Bearing Tribological Systems, Papers Presented at the 60th Meeting of the Structures and Materials Panel of AGARD, San Antonio TX 22-26, pp 11-1 to 11-12, April 1985.
- [47] Th. Roth, E. Borszeit, K.H. Kloos, "Struktur gesputterter amorpher Aluminiumoxidschichten," Zeitschrift für Werkstofftechnik, Vol 18, pp 9-15, 1987.

- [48] Th. Roth, E. Borszeit, K.H. Kloos, "Wear Behaviour of R.F.-Sputtered Alumina Coatings on Cast Iron Substrates in a Model Wear Test Under Dry Conditions and the Influence of Residual Stresses and Adhesion," *Surface and Coatings Technology*, Volume 36, pp 801-805, 1988.
- [49] H. Baumann, "Measuring surface temperatures between rolling steel cylinders using double layer transducers," *Proc Instn. Mech. Engrs.* Vol 201, No C4, pp 263-270, 1987.
- [50] R. Haller and J. Kirschner, "Druck- und Temperaturmessungen in einem Nockentriebwerk," *Tribologie und Schmierungstechnik*, Volume 36, Number 6, pp 287-292, 1989.
- [51] J. Holland and M. Tychsen, "Photolithographische Strukturierung von Dünnsfilmsensoren für EHD-Messungen," *Technisches Messen*, Volume 58, Number 12, pp 478-484, 1991.
- [52] Y. Mihara, T. Hayashi, M. Nakamura, T. Someya, "Development of measuring method for oil film pressure of engine main bearing by thin film sensor," *JSAE Review*, Volume 16, Number 2, pp 125-130, 1995.
- [53] S. Ichikawa, Y. Mihara, T. Someya, "Study on main bearing load and deformation of multi-cylinder internal combustion engine: Relative inclination between main shaft and bearing," *JSAE Review*, Volume 16, Number 4, pp 383-386, 1995.
- [54] X. Tian, F.E. Kennedy, J.J. Deacutis, A.K. Henning, "The Development and Use of Thin Film Thermocouples for Contact Temperature Measurement," *Tribology Transactions*, Volume 35, Number 3, pp 491-499, 1992.
- [55] R.A. Colclaser, S. Diehl-Nagle, *Materials and Devices for Electrical Engineers and Physicists*, McGraw-Hill, 1985.
- [56] D.D. Pollock, *Electrical Conduction in Solids: An Introduction*, Chapter 4, American Society for Metals, 1985.
- [57] C.R. Tellier and A.J. Tosser, *Size Effects in Thin Films*, Elsevier, 1982.
- [58] Chapter 4 of T.J. Coutts, *Electrical Conduction in Thin Metal Films*, Elsevier, 1974.
- [59] R. Tramposch, *Thin Film Process for Hybrid ICs, from Thin Film for Hybrids Sputtering School*, Materials Research Corporation, Orange, NY.
- [60] "Quantitative Laws of Adhesive Wear," Section 6.6 of E. Rabinowicz, *Friction and Wear of Materials*, John Wiley and Sons, 1995.

- [61] "Film Formation by Atomistic Deposition I and II," two articles in D.M. Mattox, Educational Guide to Vacuum Deposition Technology, Society of Vacuum Coaters, 1994.
- [62] B.A. Movchan and A.V. Demchishin, "Study of Structure and Properties of Thick Vacuum Condensates of Nickel, Titanium, Tungsten, Aluminum Oxide and Zirconium Dioxide," Phys. Metals Metallography, Volume 28, pp 83-90, 1969.
- [63] J.A. Thornton, "The microstructure of sputter-deposited coatings," J. Vac. Sci. Technol. A, Volume 4, Number 6, pp 3059-3065, Nov/Dec 1986.
- [64] "Microstructure of Glow-discharge Sputtered Coatings," Section 9.3.3.2 of B. Bhushan and B.K. Gupta, Handbook of Tribology: Materials, Coatings, and Surface Treatments, McGraw-Hill, 1991.
- [65] R.S. Nowicki, "Origins and Minimization of Defects in Sputtered Thin Films," Solid State Technology, Volume 23, pp 83-88, December 1980.
- [66] J. A. Sue and G. S. Schajer, "Stress Determination for Coatings," article from Surface Engineering, Volume 5 of the ASM Handbook, ASM International, 1990.
- [67] T.M. Sigalovskaya, M.P. Kalyanova, V.I. Kazarin, L.V. Aleshina, N.D. Tomashov, "Corrosion-Electrochemical Behavior of Titanium and its Alloys in Alkaline Solutions of Hydrogen Peroxide," Protection of Metals, Volume 12, Number 4, pp 331-335, 1977.
- [68] P. Kohl, Georgia Institute of Technology, personal communication, December 1995.
- [69] K.E. Healy, P. Ducheyne, "Passive dissolution kinetics of titanium in vitro," Journal of Materials Science: Materials in Medicine, Volume 4, pp 117-126, 1993.
- [70] M. J. Donachie, Jr., Editor, Titanium: A Technical Guide, page 334, ASM International 1988.
- [71] H.B. Lovering, "Direct Exposure of Photoresist by Projection," Solid State Technology, pp 39-42, July 1968.
- [72] R.W. Berry, P.M. Hall, M.T. Harris, Thin Film Technology, D. Van Nostrand, 1968, p 661.
- [73] *ibid*, p 661.
- [74] W. Kern and C.A. Deckert, "Chemical Etching," in Thin Film Processes, J.L. Vossen and W. Kern, Editors, Academic Press, 1978.

- [75] S.J. Rosenberg, Nickel and Its Alloys, NBS Monograph 106, p 55, U.S. Department of Commerce, National Bureau of Standards, May 1968.
- [76] W. Kern, "Chemical Etching of Dielectrics" pp 1-18 of Proceedings of the Symposium on Etching for Pattern Definition, 1976.
- [77] J.S. Judge, "Dissolution of SiO<sub>2</sub> in Acidic Fluoride Solutions," Journal of the Electrochemical Society, Volume 118, Number 11, November 1971, pp 1772-5.
- [78] E.M. Vander Wall and E.M. Whitener, "Concentrated Nitric & Dilute Hydrofluoric Acid Mixtures in Dissolution of Zirconium Metal," Industrial & Engineering Chemistry, Volume 51, Number 1, pp 51-54, January 1959.
- [79] H. Kikuyama, M. Waki, M. Miyashita, T. Yabune, N. Miki, J. Takano, T. Ohmi, "A Study of the Dissociation State and the SiO<sub>2</sub> Etching Reaction for HF Solutions of Extremely Low Concentration," Journal of the Electrochemical Society, Volume 141, No. 2, Pages 366-374, February 1994.
- [80] T. Smith and G.R. Hill, "A Reaction Rate Study of the Corrosion of Low-Hafnium Zirconium in Aqueous Hydrofluoric Acid Solutions," Journal of the Electrochemical Society, Volume 105, Pages 117-121, March 1958.
- [81] T.L. Yau and R.T. Webster, "Corrosion of Zirconium and Hafnium," Corrosion: Volume 13 of the ASM Metals Handbook, American Society for Metals, page 710, 1985.
- [82] F.V. Tooley, Volume II of The Handbook of Glass Manufacture, 3rd Edition, Ashlee Publishing Co., Inc., New York, New York, pp 840-842.
- [83] Product literature, AZ 1500 Series Positive Photoresists, AZ Photoresist Products Somerville, NJ.
- [84] R.W. Berry, Thin Film Technology, p349-364, Van Nostrand, 1968.
- [85] J.W. Dally, W.F. Riley, Experimental Stress Analysis, pp 182-185, McGraw-Hill, 1978.
- [86] W.M. Rohsenow, J.P. Hartnett, E.N. Ganic, Handbook of heat transfer fundamentals, p 4-112, McGraw-Hill, 1985.
- [87] N.E. Anderson, "Long-Term Hot Hardness Characteristics of Five Through-Hardened Bearing Steels," NASA TP-1341, National Aeronautics and Space Administration, 1978.

- [88] G.Xu, "Debris Denting, Spall Initiation and Propagation in Elasto-Hydrodynamic Lubricated Contacts," Ph.D. Thesis, Purdue University, May 1997.
- [89] S. Tokumaru and M. Hashimoto, "High resistivity AlOx thin films deposited by a novel two-step process," *Surface and Coatings Technology*, Volume 54/55, pp 303-307, 1992.
- [90] W. Kern, "Characterization of Localized Defects in Dielectric Films for Electron Devices: Parts 1&2," *Solid State Technology*, Volume 17, pp 35-42 and pp 78-84, March and April, 1974.
- [91] A. Belu-Marian, E. Candet, A. Devenyi, "Piezoresistive Sensors," Chapter 3 of *Thin Film Resistive Sensors*, P. Ciureanu and S. Middelhoeck, Editors, IOP Publishing, Ltd., 1992.
- [92] E. Klokholm, "Piezoresistance in Evaporated Nickel Films," *Journal of Vacuum Science and Technology*, Volume 10, Number 1, pp 235-237, January/February 1973.
- [93] R.W. Burrahm, J.K. Davis, W.D. Perry, A. De Los Santos., "Development of a Piston Temperature Telemetry System," SAE Paper 920232.
- [94] Advanced Telemetry, Inc. product literature, Advanced Telemetry, Inc., Kettering Ohio.
- [95] C.J. Amalaner, D.W. MacDonald Editors, *A Handbook on Biotelemetry and Radio Tracking*, Pergamon Press, 1980.
- [96] R.S. Mackay, *Bio-Medical Telemetry: Sensing and Transmitting Biological Information from Animals and Man*, Second Edition, John Wiley and Sons, 1970.
- [97] B. Naef-Daenzer, "A New Transmitter for Small Animals and Enhanced Methods of Home-Range Analysis," *Journal of Wildlife Management*, Volume 57, Number 4, Pages 680-689, 1993.
- [98] W. Kutsch, G. Schwarz, H. Fischer, H. Kautz, "Wireless Transmission of Muscle Potentials During Free Flight of a Locust", *Journal of Experimental Biology*, Volume 185, Pages 367-373, 1993.
- [99] P.N. Cutchis, A.F. Hogrefe, J.C. Lesho, "The Ingestible Thermal Monitoring System," *Johns Hopkins APL Technical Digest*, Volume 9, Number 1, Pages 16-21, 1988.
- [100] W.H. Ko, "Power Sources for Implant Telemetry and Simulation Systems," in *A Handbook on Biotelemetry and Radio Tracking*, C.J. Amalaner and D.W. MacDonald, Editors, Pergamon Press, 1980.



- [101]B. Parzen, Design of Crystal and Other Harmonic Oscillators, Chapters 5, 9, 10, Wiley-Interscience, 1983.
- [102]D.J. Comer, Introduction to Semiconductor Circuit Design, pp 366-370, Addison-Wesley, 1968.
- [103]ASTM D2879-92, "Standard Test Method for Vapor Pressure-Temperature Relationship and Initial Decomposition Temperature of Liquids by Isoteniscope"
- [104]J.Y. Hung, J.A. Forst, "Direct Vapor Pressure Measurement of Heatset Inks," Drying Technology, Vol. 9, No. 2, pp 501-506, 1991.
- [105]K. Sasse, J. Jose, J-C Merlin, "A Static Apparatus for Measurement of Low Vapor Pressures, Experimental Results on High Molecular-Weight Hydrocarbons," Fluid Phase Equilibria, Vol 42, pp 287-304, 1988.
- [106]ASTM D2503-92 "Standard Test Method for Relative Molecular Mass (Molecular Weight) of Hydrocarbons by Thermoelectric Measurement of Vapor Pressure"
- [107]P.A. Tornheim, "Use of a Vapor Pressure Osmometer to Measure Brain Osmolality," Journal of Neuroscience Methods, Vol. 3, pp 21-35, 1980.
- [108]J.W. Gregory, L.L. Levenson, "Vapor Pressure Measurements with the Quartz Crystal Microbalance," High Temperature Science, Vol. 22, No. 3, pp 211-216, 1986.
- [109]J.J. Scialdone, M.K. Miller, A.F. Montoya, "Methods for Measuring Vapor Pressures of Lubricants With Their Additives Using TGA and/or Microbalances," NASA Technical Memorandum 104633, National Aeronautics and Space Administration, Goddard Space Flight Center, 1996.